UNIVERSITÄT
ZU KÖLN

Raman Spectroscopic View on Quantum Materials: Local Symmetry Breaking in K_2ReCl_6; Raman Optical Activity in Ni_3TeO_6; and Electronic Excitations in Ruthenates

---

Dissertation
zur
Erlangung des Doktorgrads
der Mathematisch-Naturwissenschaftlichen Fakultät
der Universität zu Köln

vorgelegt von

Philipp Lars Stein

angenommen im Jahr 2025

Contents

CHAPTER 1

Introduction

It is certainly safe to say that condensed matter physics is a wide field. Research institutions all over the world have been studying it for centuries in all its aspects. Even though people have time and time again been quoted for saying that the field, or even physics as a whole, is almost complete and there are no big discoveries left to be made[1], they have been proven wrong every single time. This thesis is no exception to this effort. On the contrary, even though all chapters use Raman scattering as their main experimental method — one of the older experimental techniques still used today — it will, besides presenting new discoveries in materials (here: the local symmetry breaking in K_2ReCl_6), also attempt to show ways to expand the application of the technique itself. By implementing it in ways previously rarely executed successfully, as Raman optical activity on a chiral solid sample and as large-shift Raman spectroscopy on Cluster-Mott insulators, new areas for possible research in this field could be opened up.

The materials that are spectroscopically analysed for that purpose differ in many ways. K_2ReCl_6 has been known for almost a century [1] and has been extensively studied in the past, mainly for its crystallographic phase transitions that are connected to static rotation of the ReO_6 octahedra [2–5]. It

---

[1] As an example, Albert Michelson in the Ryerson Physical Laboratory's Annual Register 1894 famously wrote: *[...] it seems probable that most of the grand underlying principles have been firmly established and that [...] the future truths of physical science are to be looked for in the sixth place of decimals.*

belongs to the class of K_2PtCl_6-type materials, which, in their cubic phase, have been said to realise the "perfect" fcc structure with undistorted octahedra. This makes that class of materials a textbook system to study electronic states [6]. The fcc arrangement is also suggested to lead to a model antiferromagnetic state with exchange frustration [7]. These electronic and magnetic properties rely strongly on the high symmetry of the lattice. Symmetry-reducing effects like the spin-orbit induced Jahn-Teller effect [8] or libration of the ReO_6 octahedra [9] that have been suggested for these materials can thus have a major influence on both their magnetic and electronic properties. Raman spectroscopy is ideally suited to probe this through splitting of phonon degeneracies and violations of the cubic selection rules.

Ni_3TeO_6 as a compound was studied in the early 70s [10, 11] for its crystal structure and phonon spectrum, but did not receive major attention until its more interesting, chirality-based properties were discovered within approximately the last decade [12, 13]. Chiral materials in general have received major attention in the last years [14–18] for their novel topological quantum properties [19], non-reciprocal transport [20], and many other interesting phenomena. Optical methods have been shown to be suitable for probing these [21, 22]. Ni_3TeO_6 stands out within this class through its giant electromagnetic coupling strength [13] and optical rotation in the terahertz range [23]. It is thus one of the best candidate to show measurable Raman optical activity, an inelastic variant of optical activity that is common for molecular systems, but has been very elusive for crystals.

$Ba_3CeRu_2O_9$ (BCRO) and $Ba_3EuRu_2O_9$ (BERO) are cluster-Mott insulators that were successfully synthesised as single crystals for the very first time while this thesis work was already in progress. The effort to obtain these samples was prompted by recent successful observation of quasi-molecular dimer and trimer states in multiple iridium-based compounds [24–26], where the formation of these states is aided by the large spatial extent of the iridium 5d orbitals. While the iridium- and ruthenium-based materials are isostructural, the smaller spatial extent of the Ru 4d orbitals may hinder the formation of dimers in BCRO and BERO, although the existence of Cluster-Mott states has been shown in materials based on 4d transition metals molybdenum and niobium [27, 28]. The materials will be introduced in more detail in their respective chapters.

1.1 Introduction to Raman Spectroscopy

Given the wide scope of condensed matter physics, it is only to be expected that as the materials types and physical phenomena to be researched diversify, the experimental methods used to research these must keep up in order to remain useful. As such, there are only a handful of experimental techniques in solid state physics that have proven to be powerful and universally applicable enough to stay around as a widespread tool that can be used to measure new material classes and physical effects as they come. One of these techniques is Raman scattering, the inelastic scattering of photons from excitations in matter. It was independently discovered in 1928 both by C.V. Raman[2] and K.S. Krishnan [29] in Calcutta, and by G. Landsberg and L. Mandelstam [30] in Moscow, roughly five years after the feasibility of the underlying quantum mechanical process had first been demonstrated by A. Smekal [31].

Raman spectroscopy can be used to analyse almost any kind of matter: Liquids, gases, molecules, organic compounds, and solids both in powder form and as single crystals. It is non-invasive and non-destructive, and no physical contact with the sample is required, which allows for measurements of samples within enclosed environments like cryostats as long as the container or access window is transparent within the desired frequency range. The small wavelengths and small spot sizes in modern Raman setups permit measurements of nanostructures, extremely thin films and small biological structures, aided by developments of tip-enhanced Raman spectroscopy [32] and x-ray Raman spectroscopy (XRS) [33]. Commonly, the only type of matter for which the technique is not suited is highly conductive metals. The list of excitations that can be detected is equally long, in solids it includes phonons, magnons and other magnetic excitations, crystal field excitations, transitions

---

[2] Coincidentally, Sir C.V. Raman and I share the same birthday (just 104 years apart). One could say I was born to work in this field.

between electronic states split by spin-orbit coupling, superconducting gaps and photoluminescence, although the latter is not a Raman process and is typically unwanted in most Raman measurements. If polarised light is used and the relative orientation of the polarisation axis to the crystal axes is known, it is a very effective tool to analyse the symmetries of crystals and of their excitations. Monitoring the Raman spectrum of a system while changing external parameters, like temperature, pressure or magnetic field, yields knowledge about further material properties, e.g. both crystallographic and magnetic phase transitions. Varying the excitation wavelength can lead to resonances with electronic transitions. This can lead to greatly increased scattering intensities and help with identification of excitations, as only vibrations of the structural unit that is connected to that electronic transition are enhanced [34, 35].

The efficiency of the method was significantly improved by the invention of the laser in the late 1950s [36, 37], which provides higher power density and better coherence than previous light sources, and almost perfectly monochromatic light. In the years following this development, more specialised variants have emerged, including, among others, stimulated Raman spectroscopy (SRS) [38], surface-enhanced Raman spectroscopy (SERS) [39], coherrent anti-Stokes Raman spectroscopy (CARS) [40], time-resolved Raman spectroscopy [41] and Raman optical activity (ROA) [42], the last being one of the methods employed and further developed in this thesis.

The main limitation of Raman spectroscopy lies in the weakness of the effect. This can be quantised by the relation between the scattering cross sections for Raman- and Rayleigh scattering [43]:

$$\frac{\sigma_{Raman}}{\sigma_{Rayleigh}} \approx 10^{-8} \ . \tag{1.1}$$

Because of this, analysis of Raman scattered light requires dedicated instrumentation like multi-stage spectrometers and notch or edge filters to separate it from the elastically scattered light.

1.2 Thesis Overview

This thesis will, after this introductory part, get going by introducing the basic concepts that the presented research is based on. First and foremost, Raman spectroscopy, both in its mathematical description and its experimental realisation, will be the focus of this part. Increased attention will be given to Raman optical activity (ROA), a special variant of the technique that is used as the main experimental method in chapter 4. Following this, the electronic structure of transition metal compounds will be elucidated. This will concern the effects that lead to lifting of the degeneracy of electronic d levels, as well as a discussion of excitations between these levels, specifically in Raman spectroscopy.

The **third chapter** will focus on Raman instrumentation and spectrometry, and describe both the Raman setup that was used for the measurements in chapters 4 and 5, as well as the newly constructed setup for chapter 6.

The **fourth chapter** presents the results of the ROA measurements on Ni_3TeO_6. The chirality of the crystal structure in combination with beneficial selection rules enable observation of a usually negligible chiral scattering contribution, i.e. Raman scattering that has different intensity for incident right- or left circularly polarised light. Although ROA has been established [42] as a research method in molecular spectroscopy, it has not successfully been transfered to crystals. The chapter suggests the viability of this technique for solid state research, also by comparing to calculated ROA spectra and electronic band structure that have been obtained as part of a collaboration.

The **fifth chapter** deals with temperature dependent, linear polarisation Raman spectroscopy on K_2ReCl_6. In this structure, $ReCl_6$ octahedra are arranged on a face-centred cubic lattice with rather large spacing in between. The octahedra are thus only weakly interacting, and are very prone to tilting motions. Globally, the static rotation causes are series of structural phase transitions [2] that turn out to be beautifully visible in the Raman spectra. On top of this, dynamic tilting motion of the octahedra of considerable magnitude causes a local symmetry breaking that is detectable through altered selection Rules for Raman scattering, as well as a previously unknown, continuous set of low-energy excitations.

The **sixth chapter** extends the range of excitations that are detected to crystal field excitations, i.e., transitions between the electronic d-orbitals of transition metal ions whose degeneracy is lifted by crystal field splitting and spin-orbit coupling.[3] Two 4d transition metal compounds will be discussed, $Ba_3CeRu_2O_9$ and $Ba_3EuRu_2O_9$. These materials are suggested to be Cluster-Mott insulators, in which electrons are delocalised over pairs of face-sharing RuO_6 octahedra. These "new" electronic unit is called a *dimer* and features a new set of electronic states that are formed through bonding- and anti-bonding combination of the ruthenium single-ion states. Since the energies of Raman active transitions between these states lies between 100 meV and multiple eV, meaasuring them required construction of a new Raman setup. This setup is built around a spectrometer with a low groove density grating that enables measurements in the energy range up to and potentially exceeding 1 eV. The project was thus split in three parts: Construction of the Raman setup (chapter 3.3), Characterisation of the samples using low-energy Raman scattering, and finally measurement of the crystal field transitions (both chapter 6).

---

[3] Although the electronic structure of the materials in the previous chapters does not play a direct role in the measurements, it should be mentioned that absorption of visible light by d-d transitions is responsible for the vibrant, green colour of both K_2ReCl_6 and Ni_3TeO_6 samples.

Bibliography

[1] B. Aminoff, *Über die Kristallstruktur von* K_2ReCl_6, Z. Krist. **94**, 246 (1936)

[2] R.H. Busey, H.H. Dearman, and R.B. Bevan, Jr., *The heat capacity of potassium hexachlororhenate(IV) from 7 to 320° K. Anomalies near 12, 76, 103 and 111°K. Entropy and free energy functions. Solubility and heat of solution of* K_2ReCl_6*. Entropy of the hexachlororhenate ion.*, J. Phys. Chem. **66**, 82 (1962)

[3] H.W. Willemsen, C.A. Martin, P.P.M. Meincke, and R.L. Armstrong, *Thermal-expansion study of the displacive phase transition in* K_2ReCl_6 *and* K_2OsCl_6, Phys. Rev. B **16**, 2283 (1977)

[4] G.P. O'Leary and R.G. Wheeler, *Phase transitions and soft librational modes in cubic crystals*, Phys. Rev. B **1**, 4409 (1970)

[5] J.W. Lynn, H.H. Patterson, G. Shirane, and R.G. Wheeler, *Soft rotary mode and structural phase transitions in* K_2ReCl_6, Solid State Commun. **27**, 859 (1978)

[6] P. Warzanowski, M. Magnaterra, G. Schlicht, Q. Faure, Ch. J. Sahle, P. Becker, L. Bohatý, M. Moretti Sala, G. Monaco, M. Hermanns, P.H.M. van Loosdrecht, and M. Grüninger, *Spin-orbit coupling in a half-filled* t_{2g} *shell: The case of* K_2ReCl_6, Phys. Rev. B **109**, 155149 (2024)

[7] N. Khan, D. Prishchenko, Y. Skourski, V.G. Mazurenko, and A.A. Tsirlin, *Cubic symmetry and magnetic frustration on the fcc spin lattice* K_2IrCl_6, Phys. Rev. B **99**, 144425 (2019)

[8] S.V. Streltsov and D.I. Khomskii, *Jahn-Teller Effect and Spin-Orbit Coupling: Friends or Foes?*, Phys. Rev. X **10**, 031043 (2020)

[9] H.D. Grundy and I.D. Brown, *A refinement of the crystal structures of* K_2ReCl_6*,* K_2ReBr_6*, and* K_2PtBr_6, Can. J. Chem. **48**, 1151 (1970)

[10] R.E. Newnham and E.P. Meager, *Crystal structure of* Ni_3TeO_6, Mater. Res. Bull. **2**, 549 (1967)

[11] G. Blasse and W. Hordijk, *The vibrational spectrum of* Ni_3TeO_6 *and* Mg_3TeO_6, J. Solid State Chem. **5**, 395 (1972)

[12] I. Živković, K. Prša, O. Zaharko, and H. Berger, Ni_3TeO_6 *— a collinear antiferromagnet with ferromagnetic honeycomb planes*, J. Phys.: Condens. Matter **22**, 056002 (2009)

[13] Y.S. Oh, S. Artyukhin, J.J. Yang, V. Zapf, J.W. Kim, D. Vanderbilt, and S.-W. Cheong, *Non-hysteretic colossal magnetoelectricity in a collinear antiferromagnet*, Nat. Commun. **5**, 3201 (2014)

[14] H. Kuang, C. Xu, and Z. Tang, *Emerging Chiral Materials*, Adv. Mater. **32**, 2005110 (2020)

[15] S.C.J. Meskers, *Consequences of chirality on the response of materials*, Mater. Adv. **3**, 2324 (2022)

[16] X. Wang, C. Yi, and C. Felser, *Chiral Quantum Materials: When Chemistry meets Physics*, Adv. Mater. **36**, 2308746 (2024)

[17] E. Bousquet, M. Fava, Z. Romestan, F. Gómes-Ortiz, E.E. McCabe, and A.H. Romero, *Structural chirality and related properties in periodic inorganic solids: review and perspectives*, J. Phys.: Condens. Matter **37**, 163004 (2025)

[18] H. Chen, W. Wu, J. Zhu, Z. Yang, W. Gong, W. Gao, S.A. Yang and L. Zhang, *Chiral Phonon Diode Effect in Chiral Crystals*, Nano Lett. **22**, 1688 (2022)

[19] G. Chang, B.J. Wieder, F. Schindler, D.S. Sanchez, I. Belopolski, S.-M. Huang, B. Singh, D. Wu, T.-R. Chang, T. Neupert, S.-Y. Xu, H. Lin, and M. Z. Hasan, *Topological quantum properties of chiral crystals*, Nat. Mater. **17**, 978 (2018)

[20] T. Yoda, T. Yokoyama, and S. Murakami, *Current-induced Orbital and Spin Magnetizations in Crystals with Helical Structure*, Sci. Rep. **5**, 12024 (2015)

[21] H. Zhu, J. Yi, M.-Y. Li, J. Xiao, L. Zhang, Ch.-W. Yang, R.A. Kaindl, L.-J. Li, Y. Wang, and X. Zhang, *Observation of Chiral Phonons*, Science **359**, 579 (2018)

[22] K. Ishito, H. Mao, Y. Kousaka, Y. Togawa, S. Iwasaki, T. Zhang, S. Murakami, J.-I. Kishine, and T. Satoh, *Truly Chiral Phonons in α-HgS*, Nat. Phys. **19**, 35 (2023)

[23] D. Maluski, M. Langenbach, D. Szaller, S. Reschke, L. Prodan, I. Cámara Mayorga, S.-W. Cheong, V. Tsurkan, I. Kézsmárki, J. Hemberger, and M. Grüninger, *Giant natural optical rotation from chiral electromagnons in a collinear antiferromagnet*, arXiV: 2312.02733v1 (2023)

[24] A. Revelli, M. Moretti Sala, G. Monaco, P. Becker, L. Bohatý, M. Herrmanns, T.C. Koethe, T. Fröhlich, P. Warzanowski, T. Lorenz, S.V. Streltsov, P.H.M. van Loosdrecht, D.I. Khomskii, J. van den Brink, and M. Grüninger, *Resonant inelastic x-ray incarnation of Young's double-slit experiment*, Sci. Adv. **5**:eaav4020 (2019)

[25] A. Revelli, M. Moretti Sala, G. Monaco, M. Magnaterra, J. Attig, L. Peterlini, T. Dey, A. Tsirlin, P. Gegenwart, T. Fröhlich, M. Braden, C. Grams, J. Hemberger, P. Becker, P.H.M. van Loosdrecht, D.I. Khomskii, J. van den Brink, M. Herrmanns, and M. Grüninger, *Quasimolecular electronic structure of the spin-liquid candidate $Ba_3InIr_2O_9$*, Phys. Rev. B **106**, 155108 (2022)

[26] M. Magnaterra, M. Moretti Sala, G. Monaco, P. Becker, M. Herrmanns, P. Warzanowski, T. Lorenz, D.I. Khomskii, P.H.M. van Loosdrecht, J. van den Brink, and M. Grüninger, *RIXS interferometry and the role of disorder in the quantum magnet* $Ba_3Ti_{3-x}Ir_xO_9$, Phys. Rev. Research **5**, 013167 (2023)

[27] F.A. Cotton, *Metal Atom Clusters in Oxide Systems*, Inorg. Chem. **3**, 1217 (1964)

[28] H. Lee, M.Y. Jeong, J.-H. Sim, H. Yoon, S. Ryee, and M.J. Han, *Charge density functional plus U calculation of lacunar spinel* GaM_4Se_8 *(M = Nb, Mo, Ta, and W)*, EPL **125**, 47005 (2019)

[29] C.V. Raman and K.S. Krishnan, *A New Type of Secondary Radiation*, Nature **121**, 501 (1928)

[30] G. Landsberg and L. Mandelstam, *Eine neue Erscheinung bei der Lichtzerstreuung in Kristallen*, Naturwissenschaften **16**, 557 (1928)

[31] A. Smekal, *Zur Quantentheorie der Dispersion*, Naturwissenschaften **11**, 873 (1923)

[32] M.S. Anderson, *Locally enhanced Raman spectroscopy with an atomic force microscope*, Appl. Phys. Lett. **76**, 3130 (2000)

[33] T. Suzuki, *X-ray Raman scattering Experiment. I*, J. Phys. Soc. Jpn. **22**, 1139 (1967)

[34] B.R. Carvalho, L.M. Malard, J.M. Alves, C. Fantini, and M.A. Pimenta, *Symmetry-Dependent Exciton-Phonon Coupling in 2D and Bulk* MoS_2 *Observed by Resonance Raman Scattering*, Phys. Rev. Lett. **114**, 136403 (2015)

[35] O. Abdul-Aziz, D. Wolverson, C.J. Sayers, E. Carpene, F. Parmigiani, H. Hedayat, and P.H.M. van Loosdrecht, *Resonance-induced anomalies in temperature-dependent Raman scattering of* $PdSe_2$, J. Mater. Chem. C **12**, 11402 (2024)

[36] A.L. Schawlow and C.H. Townes, *Infrared and Optical Masers*, Phys. Rev. **112**, 1940 (1958)

[37] T.H. Maiman, *Stimulated Optical Radiation in Ruby*, Nature **187**, 493 (1960)

[38] G. Eckhardt, R.W. Hellwarth, F.J. McClung, S.E. Schwarz, and D. Weiner, *Stimulated Raman Scattering from Organic Liquids*, Phys. Rev. Lett. **9**, 455 (1962)

[39] M. Fleischmann, P.J. Hendra, and A.J. McQuillan, *Raman spectra of pyridine adsorbed at a silver electrode*, Chem. Phys. Lett. **26**, 163 (1974)

[40] P.D. Maker and R.W. Terhune, *Study of Optical Effects Due to an Induced Polarization Third Order in the Electric Field Strength*, Phys. Rev. **137**, A801 (1965)

[41] S.-Y. Lee and E.J. Heller, *Time-dependent theory of Raman scattering*, J. Chem. Phys. **71**, 4777 (1979)

[42] L.D. Barron and A.D. Buckingham, *Rayleigh and Raman Scattering from Optically Active Molecules*, Mol. Phys. **20**, 1111 (1971)

[43] R. Loudon, *The Raman Effect in Crystals*, Adv. Phys. **13**, 423 (1964)

CHAPTER 2

Raman Scattering

2.1 Classical description

The basic theory of light scattering is extensively discussed in countless books on condensed matter science and optical spectroscopy. This brief overview uses information and resources from various books [1–4], but is not intentionally based on any particular one.

The electric field of light can be written in the form $E(t) = A \cdot\ e^{-i\omega_E t}\ + c.c.$, with amplitude A and frequency ω_E. Upon interaction with matter, this oscillating electric field creates an oscillating dipole moment

$$\mu(t) = \alpha\ \cdot E(t)\ , \tag{2.1}$$

where α is the polarisability.[1] During such an oscillation, the polarisability is not constant but may changed by the excitation, e.g. if the movement of the ions deforms the electron cloud. To account for this, it can be expanded as a Taylor series up to first order in an operator of the excitation of interest.

---

[1] Interactions of matter with the magnetic field of light as well as higher order interactions with the electric field exist as well, but are usually ignored because in most systems, their contributions to scattering is minimal or non-existent. This will be discussed in detail in chapter 2.4.

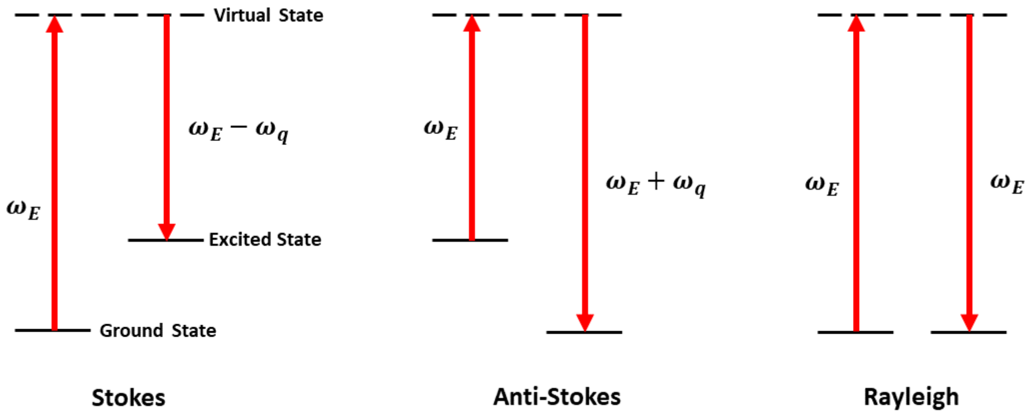

Figure 2.1: Exemplary energy level diagram of Stokes-, Anti-Stokes- and Rayleigh scattering.

For phonons, this is the normal vibrational coordinate q:

$$\alpha(t) = \alpha_0 + \frac{\delta \alpha}{\delta q} \cdot q(t) + O(q^2) \tag{2.2}$$

Corresponding expressions can be obtained for magnons by expanding in spin-exchange operators, for plasmons by expanding in terms of electron density oscillation coordinates, etc.
Approximating the phonons as a harmonic vibration with $q(t) = q_0(e^{i\omega_q t} + e^{-i\omega_q t})$, eq. (2.1) can be transformed to

$$\mu(t) = \alpha_0 A e^{-i\omega_E t} + A\frac{\delta \alpha}{\delta q}[e^{-i(\omega_E - \omega_q)t + i\phi} + e^{-i(\omega_E + \omega_q)t + i\phi}] + c.c. \tag{2.3}$$

This equation shows that upon interaction with light, the electric dipole moment may oscillate at different frequencies. The first term describes oscillation – and thus re-emission – of light at the frequency ω_E of incident light. This process is called Rayleigh scattering. The second and third terms describe dipole oscillation frequencies $\omega_E - \omega_q$ and $\omega_E + \omega_q$, respectively, where ω_E has been modified by the frequency of a phonon. These processes are called Stokes- and Anti-Stokes scattering, respectively. An energy diagram illustrating all three processes is shown in fig. 2.1. In this picture, for Rayleigh- and Stokes scattering, a phonon is excited from the ground

state to an intermediate state[2] at energy $\hbar\omega_E$ by an incoming photon. From there, the system can either transition back to the ground state under reremission of a photon at energy ω_E (Rayleigh scattering), or instead to an excited phonon state at energy $\hbar\omega_q$ with corresponding emission of a photon with energy $\hbar(\omega_E - \omega_q)$ (Stokes scattering). Anti-Stokes scattering is only possible if an excited state of the system is populated. Here, the incoming photon excites the system from that excited state to an intermediate state. The system then relaxes back to the ground state. In this case, the energy of the emitted photon will be the sum of the initial photon's energy and the excited state energy, $\omega_E + \omega_q$. The scattering cross section of this process is strongly dependent on the population of excited states, and thus, on temperature. Due to this, the ratio of Stokes- and Anti-Stokes scattering intensities can be used to measure temperature (*Raman thermometry*).
From eq. (2.3), it immediately follows that Stokes- and Anti-Stokes scattering can only contribute if $\frac{\delta\alpha}{\delta q} \neq 0$. This is the elementary condition to decide whether a vibration is Raman active or not. For example, in a linear molecule like CO_2, a symmetric stretching vibration is Raman active, but asymmetrical stretching and bending vibrations are not. These can instead be observed using infrared absorption spectroscopy, for which the condition is $\frac{\delta\mu}{\delta q} \neq 0$. In systems with inversion symmetry, the *rule of mutual exclusion* states that any given vibrational mode can only be either Raman- or infrared-active[3] [5].

2.1.1 Raman tensors and selection rules

In general, the polarisability α can be vastly different along different directions within a crystal. This requires switching from a scalar to the polarisability tensor (α_{ij}). The derivative with respect to the nuclear coordinate $\frac{\partial\alpha}{\partial q}$ is accordingly also a tensor and is commonly called the *Raman tensor* R.

---

[2] In non-resonant Raman scattering, the intermediate state is a virtual state, i.e. not an eigenstate of the system.

[3] The rule of mutual exclusion provides a necessary, but not a sufficient condition. There are also *silent* vibrational modes that are neither Raman- nor infrared active.

With this, the intensity of Raman scattered light can be expressed as

$$I \propto \left| \vec{e}_{in} \, R \, \vec{e}_{out} \right|^2 \quad . \tag{2.4}$$

$\vec{e}_{in/out}$ are the polarisation vectors of incoming and scattered light, respectively. In total, a crystal with N atoms in the unit cell has 3N vibrational modes. 3 of these are acoustic modes with E → 0 for k → 0. Since k is very small for visible light relative to the size of the Brillouin zone, and accordingly the energies of acoustic modes from which one can Raman scatter are very low, their detection requires other experimental methods like Brillouin spectroscopy [4]. The remaining 3N - 3 modes are optical phonons that can be Raman- or infrared active; or neither (or both, depending on the lattice symmetry).

Raman tensors are commonly written as a 3 x 3 matrix in a Cartesian basis. As they relate the electric field vectors of incoming polarisation to that of the scattered polarisation, see eq. 2.4, both of which are usually defined in the laboratory frame of reference, the basis vectors of the tensor correspond to that reference frame as well. The Raman tensors for all crystallographic space groups are known and tabulated [6]. Since in that depiction, the basis vectors are typically an orthogonal system based on the crystal axes, a basis transformation to the laboratory frame of reference might be necessary.

2.2 Quantum mechanical description

To obtain a more detailed expression for the transition polarisability, a quantum mechanical treatment based on time-dependent perturbation theory is required. The exact steps have been laid out in great detail in other works [2], so this section will merely present and explain the results. The polarisability tensor in the quantum mechanical formulation is

$$(\alpha_{\alpha\beta})_{if} = \frac{1}{\hbar} \sum_{v \neq i,j} \left\{ \frac{\langle f|\mu_\alpha|v\rangle\langle v|\mu_\beta|i\rangle}{\omega_{vi} - \omega} + \frac{\langle f|\mu_\beta|v\rangle\langle v|\mu_\alpha|i\rangle}{\omega_{vf} + \omega} \right\} \quad . \tag{2.5}$$

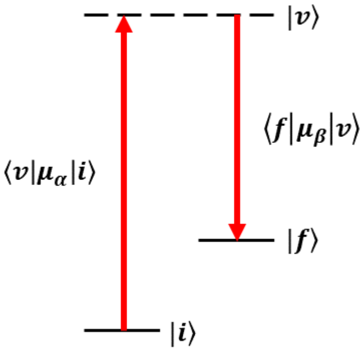

Figure 2.2: Illustration of the Raman scattering process in quantum mechanical description. Transition from an initial state $|i\rangle$ to a virtual intermediate state $|v\rangle$ via transition dipole moment μ_α, followed by a transition from that virtual state to a final state $|f\rangle$ with transition dipole moment μ_β.

.

$|i\rangle$, $|f\rangle$, $|v\rangle$ are shortened expressions for the time-independent parts of the wave functions $|\psi_i\rangle$, $|\psi_f\rangle$, $|\psi_v\rangle$ of the initial, final and intermediate state involved in the scattering process. Each term of the sum describes a transition from the initial state i to an intermediate state v, followed by a transition from that intermediate state to a final state f. The sum goes over a complete set of intermediate states, excluding the initial and final states, and each term is weighted by the inverse frequency denominator. $\mu_{\alpha,\beta}$ are the transition dipole moments, ω is the energy of incident light and $\omega_{vi} = \omega_v - \omega_i$ ($\omega_{vf} = \omega_v - \omega_f$) are the energy differences between virtual and initial (final) states, respectively. This formula operates under the assumption that the lifetimes of initial and final states are infinite, and thus the width of the energy levels is zero.

From here, the modus operandi is the same as in the classical description. The polarisability is extended according to Placzek's approximation

$$\alpha_{\alpha\beta}(q) = \langle f| \left(\alpha_{\alpha\beta}\right)_0 |i\rangle + \sum_k \left(\frac{\partial \alpha_{\alpha\beta}}{\partial q_k}\right)_0 \langle f|q_k|i\rangle \tag{2.6}$$

which again leads to the expression for the Raman tensor in eq. 2.4.

Bibliography

[1] H. Kuzmany, *Solid-State Spectroscopy: An Introduction*, Springer, Berlin, Heidelberg, 2009

[2] D.A. Long, *The Raman Effect: A Unified Treatment of the Theory of Raman Scattering by Molecules*, John Wiley & Sons Ltd., Chichester, 2002

[3] N. Ashcroft and N.D. Mermin, *Solid State Physics*, Saunders College Publishing, New York, 1976

[4] W. Hayes and R. Loudon, *Scattering of Light by Crystals*, Dover Publications, New York, 2004

[5] J.M. Hollas, *Modern Spectroscopy*, 4th ed., John Wiley & Sons Ltd., Chichester, 2004

[6] E. Kroumova, M.I. Aroyo, J.M. Perez-Mato, A. Kirov, C. Capillas, S. Ivantchev, and H. Wondratschek, *Bilbao Crystallographic Server: Useful Databases and Tools for Phase-Transition Studies*, Phase Transitions **76**, 155 (2003)

2.3 Chirality

The concept of chirality can be explained in just a few words: An object or structure is chiral if it can't be superimposed on its mirror image. Although this formal definition was only put forward by Lord Kelvin in the early 19th century, the effect itself is so fundamental and so present in nature that informal knowledge of it is likely as old as humanity itself. In biological organisms, it exists both on the microscopic scale as the handedness of molecules, and on the macroscopic scale, e.g. in human hands (hence the term *handedness*), cf. fig. 2.3a. The versions of the same object with different handedness are called its *enantiomers*. Over time, the concept of chirality has been extended to include not only static objects, but also motion. Especially, in condensed matter physics, it can be applied to ionic movements, and thus phonons. The common definition of chirality in motions requires the existence of two enantiomeric states that are interconvertible by spatial inversion, but not by time reversal [1]. The easiest example would be a circular motion in-plane combined with a propagation perpendicular to that plane, i.e., a spiral movement. Since in many cases this definition has not been exactly followed and the term *chiral phonon* has also commonly been applied to cases where the time reversal symmetry is intact, e.g. circular ion movement without propagation in the perpendicular direction, systems that fulfil the more strict condition given above are now sometimes referred to as *truly chiral*. Chiral phonons are highly sought after not only to satisfy a scientific curiosity about one of the fundamental concepts of nature, but also because they have been suggested to have promising technological applications, e.g. as one-dimensional heat diodes [2] and for generating spin-currents from a thermal gradient [3]. They can be controlled through electric [4] and magnetic fields [5] and strain [6]. The interaction of light with chiral structures or excitations can cause a number of experimental signatures, but the three most common measurable effects are optical activity, circular dichroism, and Raman optical activity. The first two of these are illustrated in fig. 2.3b). Among these, optical activity is probably the most well known. Its primary experimental consequence, the rotation of linear polarisation, has been ob-

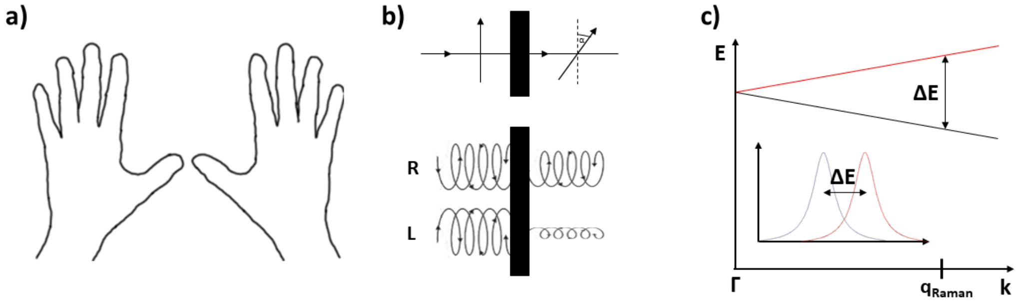

Figure 2.3: a) The outlines of the author's hands are fundamental examples for chiral objects. b) Illustration of optical activity (top) and circular dichroism (bottom). c) Schematic depiction of linear wave-vector shifts. Inset: Typical Raman spectrum obtained in such a system.

served as early as 1811 [7], more than 200 years ago. This rotation originates in different index of refraction n for left- and right circularly polarised light (LCP/RCP), and accordingly a different phase velocity ν of light. Optical activity can provide information about the overall chirality of a substance or structure and can be used e.g. to determine the ratio between left- and right-handed molecules in a solution, or the handedness of a chiral crystal, but it can't provide detailed information about the vibrational or electronic states of a system.

Circular dichroism (CD) describes the differential absorption of LCP and RCP [8]. It is usually measured and plotted over a larger wavelength range in the visible or near-UV range. Accordingly, it can provide information about the electronic states of chiral systems and transitions within these [9]. The extension of CD into the infrared range is called vibrational circular dichroism (VCD) [10]. It can detect the chirality of molecular vibrations and higher energy phonons, typically down to energies around ≈ 100 meV.

For the detection of chiral processes below 100 meV, Raman spectroscopy has turned out to be a very effective tool. In solids, measurements on systems with (truly) chiral phonons have observed an effect called linear wave-vector shift [11–20]. Here, phonon branches that are degenerate at the Γ point can split for finite q into two branches with opposite chirality, as can be seen in fig. 2.3c). These two branches will have opposite slope, and thus the

phonons will have group velocities of opposite sign, as $v_G = \frac{\partial\omega}{\partial k}$. In Raman spectroscopy with circularly polarised light, scattering from each of these branches is only allowed for either incoming LCP or RCP. The experiment thus shows a slight energy shift between the peak measured with LCP/RCP due to the small, but non-zero momentum transfer of visible light. It should be emphasised, however, that this shift is usually extremely small (< 1 cm^{-1}) and has only been successfully measured for a handful of systems [11–20].
The other type of Raman spectroscopic measurement that has been applied to chiral systems is Raman optical activity (ROA). This method, and especially its its application to solids, is examined in this thesis and will be described in more detail in the following.

2.4 Raman optical activity

As introduced in section 2.1, conventional Raman scattering formalism considers the electric transition dipole moment induced in a system through interaction with the electric field of light. Higher order interactions exist, but are usually discarded because their contribution to scattering is negligibly small. However, some of these terms can become relevant in chiral systems, or more specifically in systems that show optical activity. Thus, one must now consider not only the electric dipole moment created by interaction with the electric field of light, but also with the magnetic field, and take into account the effect of the electric field gradient:

$$\mu_\alpha = \alpha_{\alpha\beta} \ + G_{\alpha\beta} B_\beta \ + A_{\alpha\beta\gamma} \nabla_\beta E_\gamma \tag{2.7}$$

where α is the polarisability tensor as before, and G and A are both optical activity tensors. Not only do these additional interactions govern the additional terms described above, but they also cause an induced magnetic transition dipole moment m and electric transition quadrupole moment Θ:

$$m_\alpha \ = -G_{\alpha\beta} \ \cdot E_\beta \tag{2.8}$$

$$\Theta_{\alpha\beta} = A_{\alpha\beta\gamma} \cdot E_\gamma \tag{2.9}$$

In terms of scattering, G governs the electric dipole moment induced by the (time dependent) magnetic field of light, plus the induced magnetic transition dipole moment, while A describes the electric transition dipole moment induced by the electric field gradient, plus the electric transition quadrupole moment. Similar to the polarisability tensor elements (cf. chapter 2.2), the elements of the complex optical activity tensors can be expressed in quantum mechanical notation [21]:

$$(G_{\alpha\beta})_{if} = \frac{1}{\hbar}\sum_{v\neq i,j}\left\{\frac{\langle f|\mu_\alpha|v\rangle\langle v|m_\beta|i\rangle}{\omega_{vi}-\omega} + \frac{\langle f|m_\beta|v\rangle\langle v|\mu_\alpha|i\rangle}{\omega_{vf}+\omega}\right\} \tag{2.10}$$

$$(A_{\alpha\beta\gamma})_{if} = \frac{1}{\hbar}\sum_{v\neq i,j}\left\{\frac{\langle f|\mu_\alpha|v\rangle\langle v|\Theta_{\beta\gamma}|i\rangle}{\omega_{vi}-\omega} + \frac{\langle f|\Theta_{\beta\gamma}|v\rangle\langle v|\mu_\alpha|i\rangle}{\omega_{vf}+\omega}\right\} \tag{2.11}$$

with ω the frequency of incident light, $\omega_{vi} = \omega_v - \omega_i$ and $\omega_{vf} = \omega_v - \omega_f$ the frequency differences between the initial and final states, respectively, and the virtual state. μ, m and Θ are the electric dipole-, magnetic dipole- and electric quadrupole operators defined [21–25] as

$$\mu_\alpha = \sum_k e_k r_{k_\alpha} \tag{2.12}$$

$$m_\alpha = \frac{1}{2}\sum_k \frac{e_k}{m_k}\epsilon_{\alpha\beta\gamma} r_{k_\beta} p_{k_\gamma} \tag{2.13}$$

$$\Theta_{\alpha\beta} = \frac{1}{2}\sum_k e_k(3r_{k_\alpha}r_{k_\beta} - r_k^2\partial_{\alpha\beta}) \tag{2.14}$$

where the sum goes over all ions in a unit cell and r_k, p_k, m_k and e_k are their respective position, momentum, mass and charge. From these equations, it is instructive to interpret G (respectively A) as describing an electric dipole transition from initial state i to virtual state v and a consecutive magnetic dipole (electric quadrupole) transition from the virtual state v to the final state f. In the application discussed in this thesis, f is always an excited phonon state, but in general it can be any real state in a material. The inverted process, i.e. magnetic dipole- or electric quadrupole transitions from the ground state to a virtual state followed by electric dipole transitions to the excited phonon state, are described by the corresponding "scripted tensors" $\mathscr{G}$ and $\mathscr{A}$. For the case of hermitian operators, which is justified in far-from-resonance approximation, a separate treatment of these tensors is not necessary, as $\mathscr{G}_{\alpha\beta} = -G_{\beta\alpha}$ and $\mathscr{A}_{\alpha\beta\gamma} = A_{\alpha\beta\gamma}$ [21, 24]. In electric dipole approximation, the next step to obtain an expression for the scattering intensity was to extend the polarisability tensor according to Placzek's theory (see eq. 2.6 in chapter 2.2). The same procedure can also be applied to G and A:

$$G_{\alpha\beta}(q) = \langle f| \left(G_{\alpha\beta}\right)_0 |i\rangle + \sum_k \left(\frac{\partial G_{\alpha\beta}}{\partial q_k}\right)_0 \langle f|q_k|i\rangle \tag{2.15}$$

$$A_{\alpha\beta\gamma}(q) = \langle f| \left(A_{\alpha\beta\gamma}\right)_0 |i\rangle + \sum_k \left(\frac{\partial A_{\alpha\beta\gamma}}{\partial q_k}\right)_0 \langle f|q_k|i\rangle \tag{2.16}$$

As a result, in addition to $\left(\frac{\partial\alpha}{\partial q}\right)^2$, the Raman tensor will now also contain mixed terms $\left(\frac{\partial\alpha}{\partial q}\right)\left(\frac{\partial G}{\partial q}\right)$ and $\left(\frac{\partial\alpha}{\partial q}\right)\left(\frac{\partial A}{\partial q}\right)$. Typically, they can be estimated to be $\approx 10^3$ times weaker than the $\left(\frac{\partial\alpha}{\partial q}\right)^2$ contribution [22, 25]. Terms proportional to $\left(\frac{\partial G}{\partial q}\right)^2$ and $\left(\frac{\partial A}{\partial q}\right)^2$ are usually neglected, as they are accordingly around $\approx 10^6$ times weaker than $\left(\frac{\partial\alpha}{\partial q}\right)^2$.

From these equations, the condition for a phonon mode to be Raman optically active is that either $\frac{\partial G}{\partial q} \neq 0$ or $\frac{\partial A}{\partial q} \neq 0$. Thus, the intensity of optically active scattering provides a direct measure of the variation of G and A with nuclear configuration. Most importantly, these mixed terms in general lead to different scattering intensities for incoming and analysed LCP/RCP. The exact magnitudes and differences depend strongly on the scattering geometry and the polarisation vectors. Experimentally, this difference is conventionally expressed as

$$\Delta = \frac{I^{RR} - I^{LL}}{I^{RR} + I^{LL}} \tag{2.17}$$

with I^{RR} and I^{LL} the scattering intensities for RCP/LCP incoming and analysed light. The corresponding quantity for the difference between intensities

I^{RL} and I^{LR}, where the helicity of incoming and analysed light is opposite, can also be defined, but it can be shown that this difference is always zero in backscattering geometry [24].

The values can be very different for individual phonons or molecular vibrations, with the general rule that modes with vibrational patterns that strongly change the optical activity show high values for Δ. High Raman scattering intensity, on the other side, does not guarantee strong ROA [25].

The first successful experimental observation of ROA was achieved in 1973 by L.D. Barron, M.P. Bogaard and A.D. Buckingham on α-phenylethanole and α-phenylethylamine [26], and indeed, the ROA peaked around $\Delta \approx 10^{-3}$.

2.4.1 Experimental geometries

As mentioned above, the magnitude and the selection rules depend greatly on the geometry of the ROA experiment. Specifically, there are three conditions that can be varied: The scattering angle, the initial polarisation, and the analysed scattered polarisation.

For the scattering angle, theoretical considerations [24,27–30] commonly consider three possibilities: Forward scattering (0°), right-angle scattering (90°), and backscattering (180°). Although in first two decades of ROA experiments, 90° scattering was the norm, it was shown later that backscattering arrangements have a number of advantages, including a theoretically eight times higher signal-to-noise ratio [28] and a significantly lower sensitivity to measurement artefacts. In the standard scattering geometry employed for ROA experiments, the incident light is RCP or LCP, and the RCP and LCP components of the scattered light are analysed separately. This is called dual circular polarisation (DCP) ROA, and is sketched in fig. 2.4. The exact experimental setup is described in chapters 3.1 and 4.

Generalised ROA intensities have been calculated for various scattering geometries. In the relevant case for this work, i.e. DCP backscattering, and using far-from-resonance approximation, the resulting equation [21,31,32] for

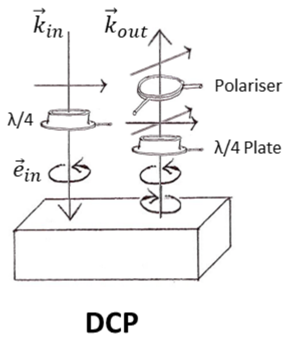

Figure 2.4: Sketch of the setup for ROA measurements in backscattering dual circular polarisation (DCP) geometry.

the ROA of a vibrational mode j is

$$\Delta = \frac{48\omega}{c} \left(\frac{1}{\omega}\gamma_j^2 + \frac{1}{3\omega}\delta_j^2 \right) \tag{2.18}$$

with

$$\begin{aligned} \gamma_j^2 = & \frac{1}{2}\left\{ \left(\frac{\partial\alpha_{xx}}{\partial Q_j} - \frac{\partial\alpha_{yy}}{\partial Q_j}\right)\left(\frac{\partial G'_{xx}}{\partial Q_j} - \frac{\partial G'_{yy}}{\partial Q_j}\right) \right. \\ & + \left(\frac{\partial\alpha_{xx}}{\partial Q_j} + \frac{\partial\alpha_{zz}}{\partial Q_j}\right)\left(\frac{\partial G'_{xx}}{\partial Q_j} - \frac{\partial G'_{zz}}{\partial Q_j}\right) + \left(\frac{\partial\alpha_{yy}}{\partial Q_j} - \frac{\partial\alpha_{zz}}{\partial Q_j}\right)\left(\frac{\partial G'_{yy}}{\partial Q_j} - \frac{\partial G'_{zz}}{\partial Q_j}\right) \\ & \left. + 3\left[\frac{\partial\alpha_{xy}}{\partial Q_j}\left(\frac{\partial G'_{xy}}{\partial Q_j} + \frac{\partial G'_{yx}}{\partial Q_j}\right) + \frac{\partial\alpha_{xz}}{\partial Q_j}\left(\frac{\partial G'_{xz}}{\partial Q_j} + \frac{\partial G'_{zx}}{\partial Q_j}\right) + \frac{\partial\alpha_{yz}}{\partial Q_j}\left(\frac{\partial G'_{yz}}{\partial Q_j} + \frac{\partial G'_{zy}}{\partial Q_j}\right)\right] \right\} \end{aligned} \tag{2.19}$$

and

$$\begin{aligned} \delta_j^2 = & \frac{\omega}{2}\left\{ \left(\frac{\partial\alpha_{yy}}{\partial Q_j} - \frac{\partial\alpha_{xx}}{\partial Q_j}\right)\frac{\partial A_{zxy}}{\partial Q_j} + \left(\frac{\partial\alpha_{xx}}{\partial Q_j} - \frac{\partial\alpha_{zz}}{\partial Q_j}\right)\frac{\partial A_{yzx}}{\partial Q_j} \right. \\ & + \left(\frac{\partial\alpha_{zz}}{\partial Q_j} - \frac{\partial\alpha_{yy}}{\partial Q_j}\right)\frac{\partial A_{xyz}}{\partial Q_j} + \frac{\partial\alpha_{xy}}{\partial Q_j}\left(\frac{\partial A_{yyz}}{\partial Q_j} - \frac{\partial A_{zyy}}{\partial Q_j} + \frac{\partial A_{zxx}}{\partial Q_j}\right) \\ & + \frac{\partial\alpha_{xz}}{\partial Q_j}\left(\frac{\partial A_{yzz}}{\partial Q_j} - \frac{\partial A_{zzy}}{\partial Q_j} + \frac{\partial A_{xxy}}{\partial Q_j} - \frac{\partial A_{yxx}}{\partial Q_j}\right) \\ & \left. + \frac{\partial\alpha_{yz}}{\partial Q_j}\left(\frac{\partial A_{zzx}}{\partial Q_j} - \frac{\partial A_{xzz}}{\partial Q_j} + \frac{\partial A_{xyy}}{\partial Q_j} - \frac{\partial A_{yyx}}{\partial Q_j}\right) \right\}. \end{aligned} \tag{2.20}$$

Due to their complexity, exact computation of these values is usually not possible. Multiple computational approaches to the simulation of ROA spectra exist [33–36], but they can only be applied to molecular vibrations.

2.4.2 Raman optical activity of solids

Although ROA has been established for decades as a leading spectroscopic method for chiral molecules and liquids, reports of measurements on solids are very rare. Successful application in crystals was predicted to possibly show much higher values than those reported for molecules due to the collective nature of phonons in contrast to isolated molecular vibrations [37]. On the other hand, perfect agreement with the fundamental ROA equations mentioned above is not expected, as their derivation requires the assumption of a completely isotropic system, i.e., a large number of randomly oriented molecules, and not a crystal with discrete symmetries [23, 25, 27, 31].

An early study of the different threshold intensity in stimulated Raman scattering with RCP/LCP on quartz [38] suggested a value of $\Delta \approx 0.2$, which is orders of magnitude higher than the values typically reported for molecules, but recent Raman scattering measurements with circularly polarised light [12] did not confirm this observation. Published results of actual ROA on solids, i.e., different scattering intensity for LCP/RCP, are very rare. Cubic crystals $NaBrO_3$ [39] and $NaClO_3$ [39, 40] showed values of $\Delta \approx 10^{-4}$, but this did not spark enough interest to establish it as a widespread research method for crystals.

Only recently, measurable ROA of notable magnitude was observed in 1T-TaS_2 [41], where it was said to originate from a light-induced chiral charge density wave, and in two-dimensional flakes of $\alpha-MoO_3$ [42], where it was reported as a signature of chiral phonons. However, it should be noted that neither of these materials has a chiral crystal structure.

Bibliography

[1] L.D. Barron, *Molecular Light Scattering and Optical Activity*, Cambridge University Press, Cambridge, 2004

[2] H. Chen, W. Wu, J. Zhu, Z. Yang, W. Gong, W. Gao, S.A. Yang and L. Zhang, *Chiral Phonon Diode Effect in Chiral Crystals*, Nano Lett. **22**, 1688 (2022)

[3] K. Kim, E. Vetter, L. Yan, C. Yang, Z. Wang, R. Sun, Y. Yang, A.H. Comstock, X. Li, J. Zhou, L. Zhang, W. You, D. Sun and J. Liu, *Chiral-phonon-activated spin Seebeck effect*, Nat. Mater. **22**, 322 (2023)

[4] H. Chen, Q. Wang, X. Feng, W. Wu and L. Zhang, *Phonon Chirality Manipulation Mechanism in Transition-Metal Dichalcogenide Interlayer-Sliding Ferroelectrics*, Nano Lett. **23**, 11266 (2023)

[5] L. Zhang and Q. Niu, *Angular momentum of phonons and the Einstein-de Haas effect*, Phys. Rev. Lett. **112**, 085503 (2014)

[6] H. Rostami, F. Guinea and E. Cappelluti, *Strain-driven chiral phonons in two-dimensional hexagonal materials*, Phys. Rev. B **105**, 195431 (2022)

[7] F. Arago, *Mémoire sur une modification remarquable qu'êprouvent les rayons lumineux dans leur passage à travers certains corps diaphanes et sur quelques autres nouveaux phénomènes d'optique*, Mémoires de la classe des sciences mathématiques et physiques de l'Institut National de France Año 1811, 1st part: 93 (1811)

[8] S.S. Andrews and J. Tretton, *Physical Principles of Circular Dichroism*, J. Chem. Educ. **97**, 4370 (2020)

[9] V. Raghavan and P.L. Polavarapu, *Chiroptical Spectroscopic Studies on Soft Aggregates and Their Interactions*, in Chiral Analysis, P.L. Polavarapu, ed., 2nd Edition, Elsevier, Amsterdam, 2018

[10] L. Nafie, *Vibrational Optical Activity: Principles and Application*, John Wiley & Sons Ltd, Chichester, United Kingdom (2011)

[11] K. Ishito, H. Mao, Y. Kousaka, Y. Togawa, S. Iwasaki, T. Zhang, S. Murakami, J.-I. Kishine, and T. Satoh, *Truly Chiral Phonons in α-HgS*, Nat. Phys. **19**, 35 (2023)

[12] E. Oishi, Y. Fujii, and A. Koreeda, *Selective observation of enantiomeric chiral phonons in α-quartz*, Phys. Rev. B **109**, 104306 (2024)

[13] K. Ishito, H. Mao, K. Kobayashi, Y. Kousaka, Y. Togawa, H. Kusunose, J.-I. Kishine, and T. Satoh, *Chiral phonons: circularly polarized Raman spectroscopy and ab initio calculations in a chiral crystal tellurium*, Chirality **35**, 338 (2023)

[14] J. Skórka, K.J. Kapcia, P.T. Jochym, and A. Ptok, *Chiral phonons in binary compounds ABi (A = K, Rb, Cs) with $P2_1/c$ structure*, Mater. Today Commun. **35**, 105888 (2023)

[15] A.S. Pine and G. Dresselhaus, *Linear Wave-Vector Shifts in the Raman Spectrum of α-Quartz and Infrared Optical Activity*, Phys. Rev. **188**, 1489 (1969)

[16] A.S. Pine and G. Dresselhaus, *Raman Spectra and Lattice Dynamics of Tellurium*, Phys. Rev. B **4**, 356 (1971)

[17] J.-P. Pinan-Lucarre, R. Ouillon, and P. Ranson, *Linear wave vector dependence of low-frequency Raman modes in two uniaxial gyrotropic quartz-type materials: α-$GaPO_4$ and α-$AlPO_4$*, Chem. Phys. Lett. **302**, 164 (1999)

[18] S.G. Garasevich, A.V. Slobodyanyuk, and Z.Z. Yanchuk, *Anomalous angular dependence of E-Mode splitting in Raman spectra of ZnP*$_2$ *and CdP*$_2$ *uniaxial gyrotropic crystals caused by spatial dispersion*, Phys. Lett. A **197**, 238 (1995)

[19] M.H. Grimsditch, A.K. Ramdas, S. Rodriguez, and V.J. Tekippe, *Piezospectroscopy of Raman lines exhibiting linear wave-vector dependence: α-quartz*, Phys. Rev. B **15**, 5869 (1977)

[20] H.M. Bizek, W. Imaino, A.K. Ramdas, and S. Rodriguez, *Linear wave-vector dependence of zone center optical phonons*, J. Raman Spectrosc. **10**, 106 (1981)

[21] D.A. Long, *The Raman Effect: A Unified Treatment of the Theory of Raman Scattering by Molecules*, John Wiley & Sons Ltd., Chichester, 2002

[22] A.D. Buckingham, *Introductory lecture. The theoretical background to vibrational optical activity*, Faraday Discuss. **99**, 1 (1994)

[23] L.D. Barron and A.D. Buckingham, *Vibrational optical activity*, Chem. Phys. Lett. **492**, 199 (2010)

[24] L.A. Nafie and T.B. Freedman, *Dual Circular Polarization Raman Optical Activity*, Chem. Phys. Lett. **154**, 260 (1989)

[25] L.D. Barron and L.D. Buckingham, *Rayleigh and Raman scattering from optically active molecules*, Mol. Phys. **20**, 1111 (1971)

[26] L.D. Barron, M.P. Boogard, and A.D. Buckingham, *Raman Scattering of Circularly Polarized Light by Optically Active Molecules*, J. Am. Chem. Soc. **95**, 603 (1973)

[27] L.D. Barron and J.R. Escribano, *Stokes-Antistokes Asymmetry in Natural Raman Optical Activity*, Chem. Phys. **98**, 437 (1985)

[28] L. Hecht, L.D. Barron, and W. Hug, *Vibrational Raman Optical Activity in backscattering*, Chem. Phys. Lett. **158**, 341 (1989)

[29] L.D. Barron, L. Hecht, W. Hug, and M.J. MacIntosh, *Backscattered Raman Optical Activity with a CCD detector*, J. Am. Chem. Soc. **111**, 8731 (1989)

[30] L. Hecht, L.D. Barron, *An Analysis of Modulation Experiments for Raman Optical Activity*, Appl. Spectrosc. **44**, 483 (1990)

[31] L. Hecht and L.A. Nafie, *Theory of natural Raman optical activity, Part I. Complete circular polarization formalism*, Mol. Phys. **72**, 441 (1991)

[32] P.L. Polavarapu and Z. Deng, *Structural Determinations using Vibrational Raman Optical Activity: From a Single Peptide Group to β-Turns*, Faraday Discuss. **99**, 151 (1994)

[33] P. Bour, *Computations of the Raman Optical Activity via the Sum-Over-States Expansion*, J. Comput. Chem. **22**, 426 (2001)

[34] K. Ruud and A.J. Thorvaldsen, *Theoretical Approaches to the Calculation of Raman Optical Activity Spectra*, Chirality **21**:E54 (2009)

[35] S.T. Mutter, F. Zielinski, P.L.A. Popelier, and E.W. Blanch, *Calculation of Raman optical activity spectra for vibrational analysis*, Analyst **140**, 2944 (2015)

[36] S. Luber, *Raman Optical Activity Spectra from Density Functional Perturbation Theory and Density-Functional-Theory-Based Molecular Dynamics*, J. Chem. Theory Comput. **13**, 1254 (2017)

[37] P.J. Stephens, A.D. Buckingham, L.A. Nafie, P.L. Polavarapu, T.A. Keiderling, R.E. Hester, L. Hecht, L.D. Barron, H. Weiser, A.V. Slobodyanyuk, M. Diem, P. Malon, A. Beil, D. Luckhaus, R. Marquardt, M. Quack, A. Hansen, B. Stewart, J.M. Hicks, H. Sugeta, J.P. Simons, P. Bour, T.B. Freedman, A.F. Drake, *General Discussions*, Faraday Discuss. **99**, 87 (1994)

[38] M. Klein and M. Maier, *Giant Raman optical activity of the 128 cm^{-1} mode in quartz*, Opt. Commun. **44**, 411 (1983)

[39] M. Lindner, B. Schrader, and L. Hecht, *Raman Optical Activity of Enantiomorphic Single Crystals*, J. Raman Spectrosc. **26**, 877 (1995)

[40] R. Ouillon, J.P. Pinan Lucarre, and P. Ranson, *First-Order Spatial Dispersion Effects in the Raman Spectrum of* $NaClO_3$, J. Raman Spectrosc. **25**, 489 (1994)

[41] E.M. Lacinska, M. Furman, J. Binder, I. Lutsyk, P.J. Kowalczyk, R. Stepniewski, and A. Wysmolek, *Raman Optical Activity of 1T-*TaS_2, Nano Lett. **22**, 2835 (2022)

[42] R. Kumar, P.K. Barman, P.K. Nayak, and M.S.R. Rao, *Chiral phonon and in-plane Raman optical activity of anisotropic layered* α*-*MoO_3, Phys. Rev. B **110**, 085423 (2024)

2.5 Crystal field theory

The interaction between electrons in the d-orbitals of transition metal cations and the surrounding ligand anions in a crystal is described by crystal field theory. Specifically, the main goal is to outline how the presence of this external charge distribution influences the energies of the five d-orbitals. These orbitals are energetically degenerate in a free ion, but the degeneracy is lifted in the presence of additional interactions.

The wave functions of the five d-orbitals are typically separated into a radial and an angular part: $\Psi(\vec{r}) = \mathrm{R(r)\ X}(\Theta,\phi)$. The angular part is expressed by the so-called cubic harmonics d_{xy}, d_{xz}, d_{yz}, $\mathrm{d}_{x^2-y^2}$ and d_{z^2}. These, in turn, are linear combination of Laplace spherical harmonics Y_l^m, which form a set of basis functions on spherical surfaces:

$$\begin{aligned}
d_{xy} &= \frac{1}{\sqrt{2}}\left(Y_{2,2} - Y_{2,-2}\right) = \sqrt{\frac{15}{4\pi}}\frac{xy}{r^2} \\
d_{yz} &= \frac{1}{\sqrt{2}}\left(Y_{2,1} + Y_{2,-1}\right) = \sqrt{\frac{15}{4\pi}}\frac{yz}{r^2} \\
d_{z^2} &= Y_{0,0} \qquad\qquad\quad\;\; = \sqrt{\frac{15}{4\pi}}\frac{1}{2\sqrt{3}}\frac{3z^2-r^2}{r^2} \\
d_{xz} &= \frac{1}{\sqrt{2}}\left(Y_{2,1} - Y_{2,-1}\right) = \sqrt{\frac{15}{4\pi}}\frac{xz}{r^2} \\
d_{x^2-y^2} &= \frac{1}{\sqrt{2}}\left(Y_{2,2} + Y_{2,-2}\right) = \sqrt{\frac{15}{4\pi}}\frac{x^2-y^2}{r^2}
\end{aligned} \tag{2.21}$$

The cubic harmonics are visualised in fig. 2.5.

In the simplest picture, all surrounding ions are assumed to be undeformable charged spheres. The combined electrostatic potential at a lattice site is the sum of electrostatic potentials $V = \frac{e}{r}$ caused by the surrounding charge distribution. In a perfect octahedral coordination, a transition metal cation sits in the centre of an octahedron of ligand anions, which produce a total electrostatic potential $V = \sum_{i=1}^{6} V_i$. The effect of this potential on the electronic orbitals is described by the crystal field Hamiltonian, which is

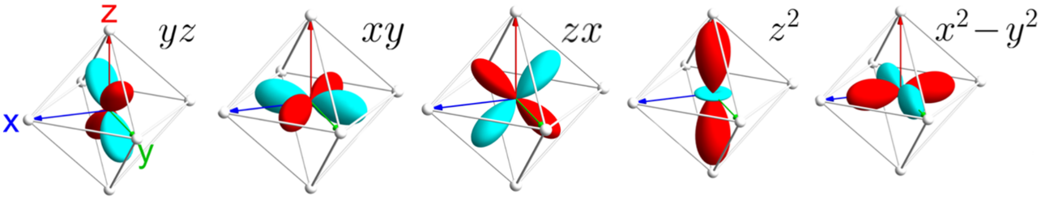

Figure 2.5: Graphic depiction of the cubic harmonics. From [M. Magnaterra, *RIXS interference in dimers, trimers, and tetrameters: bond-directional excitations and quasimolecular wavefunctions*, PhD Thesis, Universität zu Köln (2025)].

typically written using normalised spherical harmonics:

$$H_{CF} = \sum_{k=0}^{\infty} \sum_{m=-k}^{k} A_{km} C_k^m(\Theta, \phi) \tag{2.22}$$

with

$$C_m^k(\Theta, \phi) = \sqrt{\frac{4\pi}{2k+1}} Y_k^m(\Theta, \phi)) \quad . \tag{2.23}$$

Under the assumption of (symmetric) point charges, all terms for odd values of k vanish. Additionally, only terms with $0 \leq \ k \leq \ 2l$, with l = 2 for d ions, l = 3 for f ions, etc., can couple to the orbitals, so that the sum can be written as

$$H_{CF} = \sum_{k=0, keven}^{2l} \sum_{m=-k}^{k} A_{km} C_k^m(\Theta, \phi) \tag{2.24}$$

The pre-factors $A_{k,m}$ depend on the exact charge distribution around the metal ion. For the simplest case of O_h symmetry, only $A_{0,0}$ and $A_{4,0}$ are non-zero. To solve for the energies of the d-orbitals, H_{CF} can be expressed as a matrix with the spherical harmonics as basis functions:

$$H_{CF} = \begin{pmatrix} A_{0,0} + \frac{1}{21}A_{4,0} & 0 & 0 & 0 & \frac{5}{21}A_{4,0} \\ 0 & A_{0,0} - \frac{4}{21}A_{4,0} & 0 & 0 & 0 \\ 0 & 0 & A_{0,0} + \frac{2}{7}A_{4,0} & 0 & 0 \\ 0 & 0 & 0 & A_{0,0} - \frac{4}{21}A_{4,0} & 0 \\ \frac{5}{21}A_{4,0} & 0 & 0 & 0 & A_{0,0} + \frac{1}{21}A_{4,0} \end{pmatrix}$$

H_{CF} can be diagonalised by transforming from this basis to another one

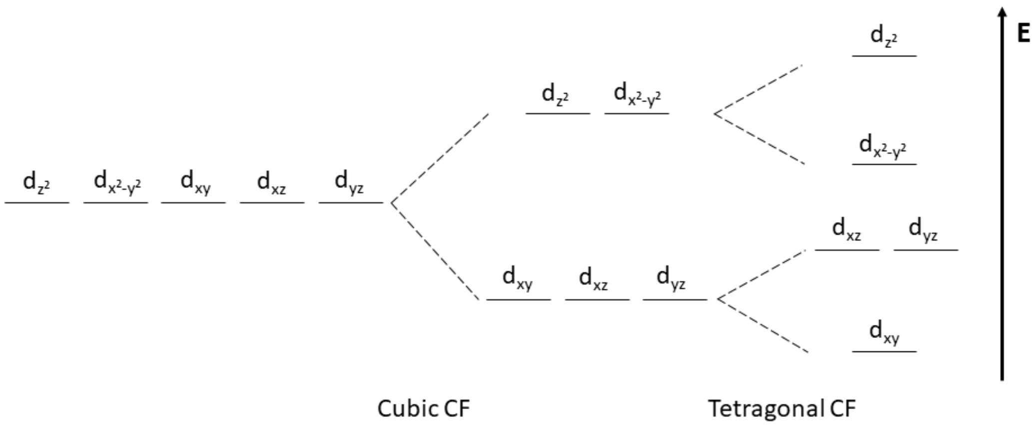

Figure 2.6: Crystal field (CF) splitting of d-orbitals. Left: Without CF, the five orbitals are energetically degenerate. Middle: The cubic crystal field splits them into a t_{2g} triplet and an e_g doublet. Right: Stretching or compressing the z axis lifts more of the degeneracies.

spanned by the cubic harmonics $d_{x^2-y^2}$, d_{z^2}, d_{xy}, d_{xz} and d_{yz}. This will yield the eigenenergies of the d orbital wavefunctions:

$$H_{CF} = \begin{pmatrix} A_{0,0} + \frac{2}{7}A_{4,0} & 0 & 0 & 0 & 0 \\ 0 & A_{0,0} + \frac{2}{7}A_{4,0} & 0 & 0 & 0 \\ 0 & 0 & A_{0,0} - \frac{4}{21}A_{4,0} & 0 & 0 \\ 0 & 0 & 0 & A_{0,0} - \frac{4}{21}A_{4,0} & 0 \\ 0 & 0 & 0 & 0 & A_{0,0} - \frac{4}{21}A_{4,0} \end{pmatrix}$$

The d_{xz}-, d_{xy}- and d_{yz}-orbitals form a lower energy triplet (t_{2g}) and the d_{z^2}- and $d_{x^2-y^2}$-orbitals form a higher energy doublet (e_g). This can also be understood by looking at the illustration of the orbitals in fig. 2.5. The orbitals whose wavefunction amplitude is maximised in the direction of a ligand are higher in energy, while those whose wavefunction amplitude is minimal towards the ligands have lower eigenenergy. The remaining degeneracy is typically lifted in the presence of crystal fields of lower symmetry, e.g. tetragonal or trigonal (right side in fig. 2.6), or spin-orbit coupling.

2.5.1 Filling rules

In a system with just one single electron in the d-orbitals, that electron will occupy the lowest energy state. As soon as there are more electrons, the order in which the orbitals are populated depends strongly on the relative strengths of the interactions within the system and the crystal field splitting. Since electrons that occupy the same orbital will have identical quantum numbers n, l, m_l and j, and the spin quantum number can only take the values $m_S \ = \pm \frac{1}{2}$, the Pauli exclusion principle [1] demands that any orbital can be occupied by at maximum two electrons. Systems in which the Coulomb repulsion U is the dominant interaction can be described by the *LS coupling* scheme. In this case, the quantum numbers l and s for each individual electron can be described by one total angular momentum number L and one total spin quantum number S for the entire atom. The ground state of such a system is determined by Hund's rules:

1. The lowest energy state is the one with the highest spin-multiplicity 2S + 1. In other words: All available orbitals will be singly occupied before the first one gets doubly occupied.

2. If multiple states with the same spin multiplicity exist, the one with the highest value of L is the ground state. In an intuitive picture, this means that it's energetically favourable for all electrons to orbit in the same direction.

3. If the outer orbital is less than half-filled, the term with lowest J is lowest in energy. If it's more than half-filled, the term with highest J is lowest in energy. This minimises the energy contribution from spin-orbit coupling.

Each electronic configuration is described by a *term symbol* of the form ${}^{2S+1}L_J$. It consists of a capital letter indicating the total orbital angular momentum L in spectroscopic notation (S, P, D, F, ... for L = 0, 1, 2, 3, ...), preceded by the spin multiplicity 2S + 1 as a superscript and succeeded by the total angular momentum quantum number J as a subscript.

2.5.2 Raman spectroscopy on crystal field excitations

The general principle of Raman spectroscopy on electronic states and its mathematical formulation are mostly similar to that on phonons presented in chapter 2. Light with electric field vector $\vec{E}$ and incident direction along $\vec{k}$ induces a polarisation $\vec{P} \ = \chi\vec{E}$ in the material. The excitations with eigenfrequencies ω_0 modulate χ and create components with $\omega_S \ = \omega_{in} \pm \omega_0$. The scattering intensity depends on the scattering cross section:

$$\frac{d^2\sigma}{d\Omega d\omega_S} \ = n g_{\omega_0}(\omega) \frac{e^2 \omega_L \omega_S^2}{(4\pi\epsilon_0 c^2)^2} \ (\alpha) \tag{2.25}$$

with n the number of active ions in the scattering valume, $g_{\omega_0}(\omega)$ is the line shape function of the excitation at ω_0 and α the single-ion polarisability.

If the electrons are extremely localised on a specific lattice site, the irreducible representation of the crystallographic point group of that site is mainly responsible for the selection rules of crystal field excitations [2].

The Raman activity of these transitions generally follows two rules:

1. Spin selection rule: An excitation can only be Raman active if it conserves the spin multiplicity 2S + 1, S = $\sum$ s the sum over all individual electron spins.

2. Parity selection rule (also called Laporte rule): If the transition metal ion is on a centrosymmetric site, intra-configurational transitions (d → d, f → f) are forbidden one-photon techniques, but still appear in parity-conserving two-photon processes like Raman [2].

The Laporte rule is only valid in for free ions, but may survive even in a crystal environment. Contrary to phonons, where according to Placzek's theory the polarisability tensor must be symmetric in electric dipole approximation, the polarisability tensor for electronic Raman scattering often contains asymmetric elements that induce magnetic dipole scattering, and symmetric, but anisotropic components that induce electric quadrupole scattering contributions [2].

2.5.3 Selection rules

As a general rule, transitions between electronic states are allowed if the direct product of the irreducible representations (*irreps*) of initial state, Raman tensor and final state contains the totally symmetry representation. In linearly polarised measurements, parallel polarisation couples to symmetric irreps like A_{1g} and E_g, and crossed polarisation couples to asymmetric irreps like T_{2g}. For the simple case of a cubic crystal field, there are three different types of excitations:

$$\begin{aligned} t_{2g} \leftrightarrow e_g: &\quad T_{2g} \otimes E_g = T_{1g} \oplus T_{2g} \\ intra - e_g: &\quad E_g \otimes E_g = A_{1g} \oplus A_{2g} \oplus E_g \\ intra - t_{2g}: &\quad T_{2g} \otimes T_{2g} = A_{1g} \oplus E_g \oplus T_{1g} \oplus T_{2g} \end{aligned} \tag{2.26}$$

where $\otimes$ and $\oplus$ denote a tensor product and a direct sum of representations, respectively. Accordingly, excitations between t_{2g} and e_g states are Raman active in crossed polarisation, intra-e$_g$ transitions are active in parallel polarisation, and intra-t_{2g} excitation are active in both.

As discussed before, in most real systems, there are additional interactions that play a role and alter this simplified picture, like trigonal crystal fields and spin-orbit coupling (SOC). These effects can massively influence the selection rules.

In the presence of trigonal crystal fields, the t_{2g} triplet splits into a non-degenerate a_{1g} and a degenerate e_g' state [3–5]. The splitting is quantified by the trigonal CF parameter Δ_{trig}, which can be positive or negative. The corresponding irrep also splits:

$$T_{2g} \rightarrow A_{1g} \oplus E_g \quad , \tag{2.27}$$

so the components of T_{2g} are redistributed to A_{1g} and E_g. The e_g doublet typically doesn't split, but is shifted in energy. In a polarisation selective Raman measurement, the presence of a trigonal crystal field causes the previously strictly cross polarised intra-t_{2g} excitations to also appear in the parallel polarisation spectrum. Observation of such a leakage is thus a hallmark of broken cubic symmetry.

The presence of SOC has a different effect on the electronic states. The additional interaction mixes the spins (S=1/2) with the effective orbital momentum $L_{eff} = 1$ of the t_{2g} triplet and causes an energy contribution

$$H_{SOC} = \lambda \overrightarrow{L} \cdot \overrightarrow{S} \tag{2.28}$$

with the spin-orbit coupling constant λ determining the mixing amplitude [6]. This produces two total angular momentum multiplets: A higher energy $J_{eff} = 1/2$ doublet and a lower energy $J_{eff} = 3/2$ quartet.

The transition between these multiplets is of T_{2g} symmetry, which causes it to be active in crossed polarisation Raman scattering. In many real systems, both trigonal crystal field and SOC are present. Their relative strength determines which effect is dominant. Three cases can be differentiated:

$\lambda \gg \Delta_{trig}$: Energy levels reorganise into $J_{eff} = 1/2$ and $J_{eff} = 3/2$ states. Raman active excitations correspond to transitions between these J_{eff} multiplets, and the selection rules are governed by SOC. This picture is very common in iridium-based compounds because of the strong SOC in 5d ions.

$\Delta_{trig} \gg \lambda$: The electronic states mostly correspond to the case for trigonal splitting, but there is additional intensity redistribution between the linear polarisation channels. The presence of SOC can also cause the appearance of (weak) peaks corresponding to transitions that are otherwise symmetry-forbidden.

$\lambda \approx \Delta_{trig}$: Neither the orbital nor the J_{eff} picture describe the electronic structure well. All excitations are between mixed energy levels, the Raman spectra show broadened and/or split features. There is no clear polarisation dependence, but the spectra in parallel/crossed polarisation may still show characteristic differences.

In the absence of additional interactions, the intensities of excitations in different polarisation channels can be used as an indicator for the relative strengths of these two interactions.

Bibliography

[1] W. Pauli, *Über den Zusammenhang des Abschlusses der Elektronengruppen im Atom mit der Komplexstruktur der Spektren*, Z. Phys. **31**, 765 (1925)

[2] G. Schaack, *Raman Scattering by Crystal-Field Excitations*, in M. Cardona, G. Güntherodt, eds., *Light Scattering in Solids VII: Crystal Field and Magnetic Excitations*, Springer, Berlin (2000)

[3] H. Liu, J. Chaloupka, and G. Khaliullin, *Exchange interactions in d^5 Kitaev materials: From Na_2IrO_3 to α-$RuCl_3$*, Phys. Rev. B **105**, 214411 (2022)

[4] S. De, A. Chauhan, B.R.K. Nanda, and A. Banerjee, *Tuning the interplay of spin-orbit coupling and trigonal crystal-field effect in the Ising-like spin system $Ca_3Co_2O_6$*, Phys. Rev. B **107**, 014418 (2023)

[5] S. Agrestini, C.-Y. Kuo, K.-T. Ko, Z. Hu, D. Kasinathan, H.B. Vasili, J. Herrero-Martin, S.M. Valvidares, E. Pellegrin, L.-Y. Jang, A. Henschel, M. Schmidt, A. Tanaka, and L.H. Tjeng, *Electronically highly cubic conditions for Ru in α-$RuCl_3$*, Phys. Rev. B **96**, 161107(R) (2017)

[6] G.L. Stamokostas and G.A. Fiete, *Mixing of t_{2g}-e_g orbitals in 4d and 5d transition metal oxides*, Phys. Rev. B **97**, 085150 (2018)

CHAPTER 3

Instrumentation for Raman Spectroscopy

Although the basic principle of Raman spectroscopy is easy to understand, the low scattering cross-section for the underlying process means that using Raman spectroscopy for scientific research requires a set of finely tuned optical components. As mentioned in chapter 1.2, lasers are commonly used as a light source, because they provide highly monochromatic, coherent light at high powers. The most common type of laser nowadays are diode-pumped solid-state (DPSS) lasers, mostly because of their higher energy conversion efficiency, better beam quality and longer lifetimes in comparison to gas lasers [1]. The output wavelengths can vary over the entire visible range, depending on the specific application. After some beam conditioning, the light is focussed onto a sample, and the scattered light is collected, collimated and directed towards a spectrometer. Typically, the polarisation of the light before and after interaction with the sample is controlled by polarisation filters, and the elastically scattered light is filtered out either by a notch filter or a pre-monochromator. The light is then focussed onto the entrance slit of the spectrometer. As inelastically scattered light generally consists of photons spread across an extended range of energies, this lens, and also any filters in the scattered light beam path, need to be achromatic. The numerical

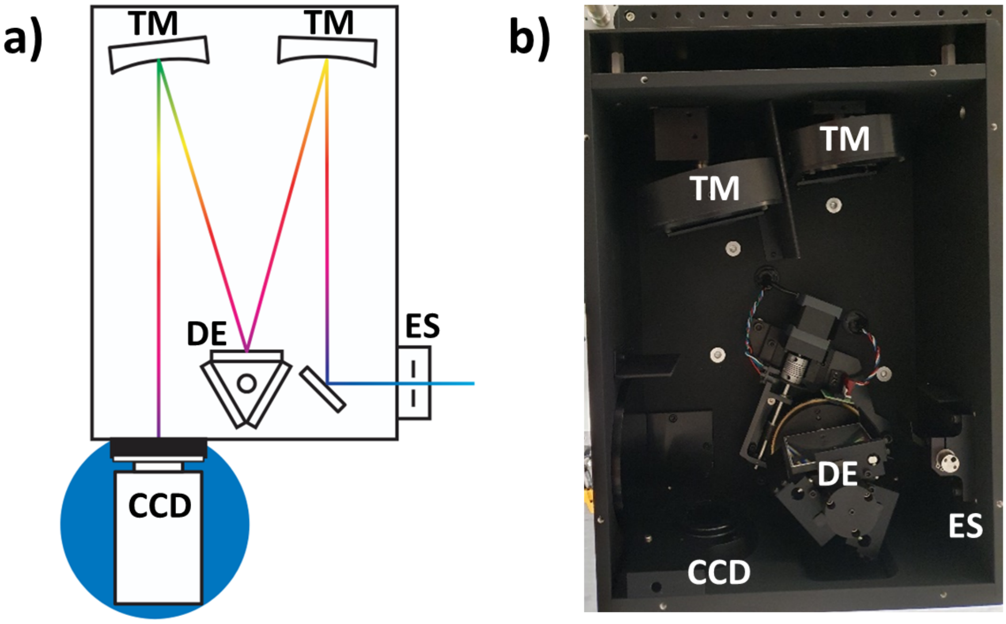

Figure 3.1: a) Schematic drawing of the principal components of a spectrometer: Entrance slit (ES), toroidal mirrors (TM), dispersive element (DE) and exit to the CCD camera [4]. b) Photograph of the inside of a Princeton HRS-300 spectrometer.

aperture (NA) of the lens should match that of the spectrometer:

$$NA = n\frac{D}{2f} \ , \tag{3.1}$$

with D and f the diameter and focal length of the lens, respectively, and n the refractive index of the surrounding medium (typically n ≈ 1 for operation in air).

The spectrometer analyses the scattered light. The standard layout of a single-grating spectrometer is shown in fig. 3.1a. It consists of the entrance slit, two toroidal mirrors, a dispersive element, and an exit slit or CCD camera. The basic functionality of a spectrometer can be summarised by the following quote [3]:

> *"A spectrometer is an imaging system that maps a plurality of monochromatic images of the entrance slit onto the detector plane."*

The entrance slit defines the initial image that is projected. A narrow slit leads to a better energy resolution in the final spectrum, but it also reduces the intensity of the detected signal. The width is usually adjustable using a micrometer screw, with typical values between 30 and 200 μm. Inside the spectrometer, the light is collimated by a toroidal mirror and directed towards the dispersive element, which can be either a grating or a prism. In most spectroscopy applications, gratings are used, as they have a significantly higher efficiency due to the light being reflected rather than transmitted, better energy resolution, can be optimised for the desired energy region, and are more manageable in size [1]. The grating disperses the light according to Bragg's law

$$n\lambda = 2d * sin(\Theta) \tag{3.2}$$

with n the order of diffraction, λ the wavelength of light, d the distance between grooves and Θ the dispersion angle. A second spherical mirror focusses the light onto a CCD camera (or an exit slit in case of single-channel detection). The CCD camera records the spatial distribution of incoming photons. When the desired integration time is reached, the number of photons that impacted each pixel of the camera is read out and transmitted to a PC. CCD cameras for spectrometry are usually cooled in order to avoid an influence of thermally excited electrons ("*dark current*") on the measurement. Since the efficiency of the grating is usually different for horizontal and vertical polarisation of light, it is advisable to use a half-wave plate in front of the entrance slit in order to rotate the detected polarisation to the direction of maximum efficiency.

3.1 The low energy Raman setup

The Raman setup used for two of the three projects covered in this thesis (chapters 4 and 5) is sketched in fig. 3.2. A Cobolt Samba Nd:YAG laser emits light with a wavelength of 532 nm and a power of 1 W. A combina-

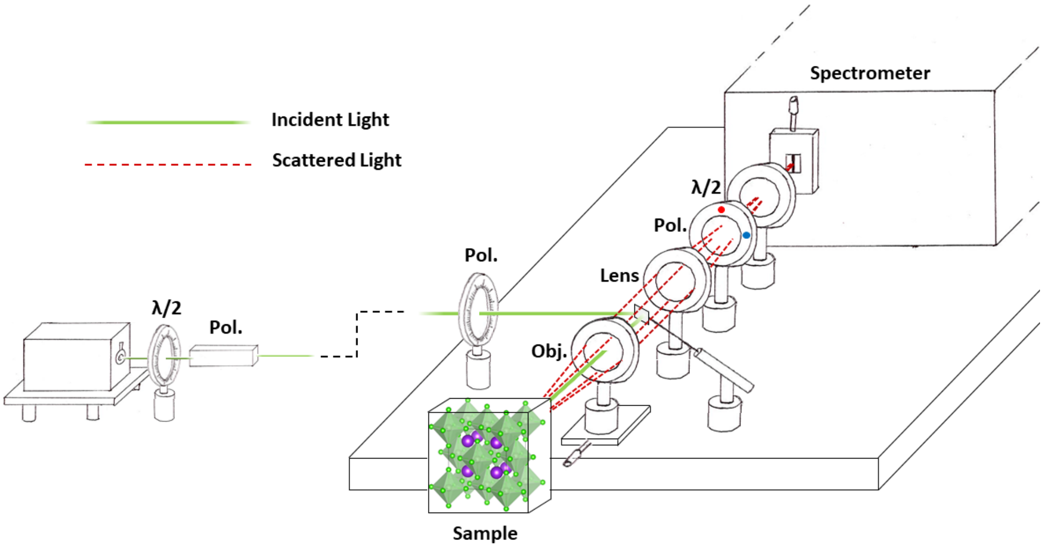

Figure 3.2: Sketch of the low-energy Raman setup using the Horiba Jobin Yvon T64000 spectrometer.

tion of half-wave plate and Glan-Thompson polariser can be used to finely tune the beam power, and a telescope consisting of two lenses with equal focal lengths reduces beam dispersion. The light is then directed upwards (not shown in fig. 3.2) to the elevation of the spectrometer's optical axis, and propagates in a 90° angle from that axis towards the entrance area of the spectrometer. A polariser with an extinction ratio $>$ 100000:1 ensures horizontal polarisation, and a tiny mirror that sits on the optical axis of the spectrometer reflects the light to the sample area. The samples are usually mounted in a Janis ST-500 cryostat which is evacuated down to pressures of $\approx 10^{-5}$ mbar and can be cooled by liquid helium flow down to temperatures around 5 K. It is placed on an xy translation stage in order to control the position of the laser spot on the sample. The incoming light is focussed down to a spot size of around 30 μm by a camera objective, which is mounted on a z-translation stage to adjust the focal depth. For measurements with circularly polarised light, a quarter-wave plate can be inserted between the tiny mirror and the objective. The scattered light is collected and collimated by that same objective (*backscattering geometry*) and focussed onto the entrance slit of the spectrometer by a lens with focal length f = 30 cm. A final

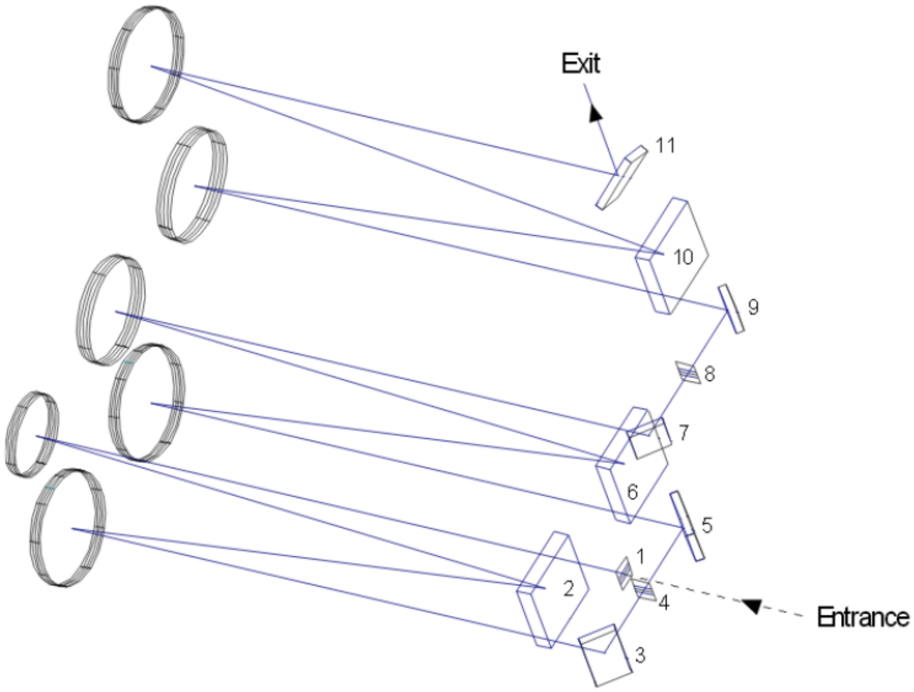

Figure 3.3: Sketch of the parts and light path inside the Horiba Jobin Yvon T64000 spectrometer [5]. Entrance slit (1), Gratings (2, 6, 10), internal slits (4 & 8) and mirrors (3, 5, 7, 9, 11).

polariser behind that lens allows selection of one direction of polarisation to be analysed, and a half-wave plate in front of the entrance slit ensures that the incoming light is always vertically polarised to guarantee maximum detection efficiency. Unless otherwise noted, the slit width is typically 100 μm. This, in combination with the grating constant discussed below, the optical path length in the spectrometer, and a typical excitation wavelength of 532 nm, leads to an energy resolution of ≈ 2 cm^{-1}.

The scattered light is analysed by a Horiba Jobin Yvon T64000 triple grating spectrometer. Its internal components and the beam path are shown in fig. 3.3. The first two gratings (labels 2 and 6) combined with an internal slit (4) form a monochromator, whose main purpose is to block the elastically scattered light. The third grating (10) with a grating constant of 1800 grooves/mm disperses the light and a spherical mirror images it onto a LN_2 cooled CCD camera. The signal is then read out for each pixel and transferred to a PC, where it is recorded and displayed by the LabSpec 5 software.

3.2 Motivation for a high energy Raman setup

The Raman setup using the Jobin Yvon T64000 spectrometer has proven to be a very useful and reliable way to measure Raman active phonons, low-energy continua and magnetic excitations in the energy range up to ≈ 100 meV. There are, however, other kinds of Raman active excitations whose excitation energies are significantly higher. These are generally transitions between electronic states that are split in energy by crystal fields, and spin-orbit interaction. Measurement of these can thus provide direct information about the electronic structure of a material. It can also confirm or deny the presence of additional effects like Jahn-Teller splitting and orbital mixing.
High energy Raman spectroscopy and other techniques that can measure excitations in the energy range between 100 meV and ≈ 2 eV, like resonant inelastic x-ray scattering (RIXS) and infrared absorption, are thus complementary. Raman spectroscopy of these high energy excitations is highly desirable, but provides some challenges. The inelastically scattered photons will have wavelengths in the upper visible- to lower infrared range, where the efficiency of gratings and the detection efficiency of CCD cameras can be very low. Spectrometers designed for detection of phonons with a good energy resolution have high grating constants to ensure high density of pixels per energy unit, but this also means that the total spectral coverage of the CCD array is limited. In order to cover a wide energy range, the measurement needs to be repeated several times with slightly different grating angles, leading to extremely long measurement times. Electronic excitations can also have widths that exceed the spectral coverage of such a spectrometer, which usually means that the shape of the excitations can't be properly measured, an effect sometimes referred to as *windowing*. Spectrometers designed for the detection of low energy excitations often use sets of two additional gratings as pre-monochromators in order to remove the elastic scattering peak from

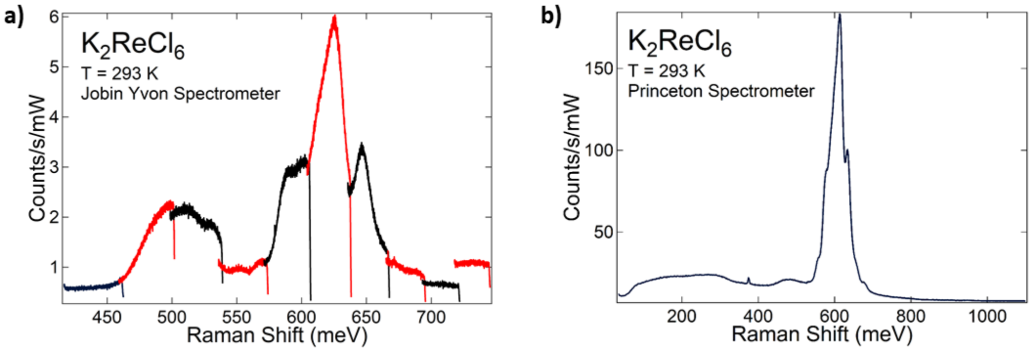

Figure 3.4: Raman Spectra of K_2ReCl_6 at room temperature. a) Measured with the Jobin Yvon T64000 spectrometer. This spectrum consists of 10 separately measured energy windows. b) Measured with the Princeton HRS-300 spectrometer.

the spectra. Although necessary in that case, this becomes a disadvantage when measuring above the phononic energy range, as efficient blocking of the elastic scattering is not required anymore, and the use of additional gratings severely reduces the efficiency of a spectrometer. An example of this is shown in fig. 3.4a. K_2ReCl_6 has a group of luminescence peaks that, when measured with an incident wavelength of 532 nm, appear in the spectrum in the energy region between 450 meV and 700 meV (the material will be discussed in detail in chapter 5). To cover this region, 10 consecutive measurements at different grating angles have to be done. Fig. 3.4b shows the same spectral region measured with a single lower groove density grating and a less energy dependent detection efficiency. The count rates are ≈ 30 times higher and the entire spectrum between 100 meV and 1100 meV can be recorded in one scan. It can also be seen by comparing the left and right panels that the windowing and the strongly wavelength-dependent detection lead to distorted representation of the relative intensities of the individual features.

It is thus desirable to complement the existing Raman setup that is optimised for detection of low-energy excitations with one that is optimised for detection in higher energy regimes.

3.3 Design of the high energy Raman setup

The spectrometer that was set up as part of this thesis is a Princeton HRS-300 equipped with a 150 grooves/mm grating. The spectra are then recorded by a Peltier cooled Princeton PIXIS 100 CCD camera with an operating temperature of -75°, and array of 1340 x 100 pixels with a pixel width of 20 μm. The setup uses the same lasers that are also used for the setup described in chapter 3.1. The light can be diverted towards this new setup using a flip mirror that is placed after the respective telescopes. The high energy Raman setup is built entirely on a separate breadboard. It stands on the optical table on four 30 cm long metal legs. Thus, the whole setup can be moved without affecting the alignment and can be placed in any other location or setup as desired, only requiring a light source and a computer to function. A setup sketch can be seen in fig. 3.5. The incident light is linearly polarised by a filter (not shown) and passes a beam splitter with a 45° angle of incidence. 30% of the light is reflected down in a 90° angle towards the sample stage, while the remaining 70% is transmitted and hits a beam block. An Olympus LMPLANFL N objective with 50x magnification, NA =

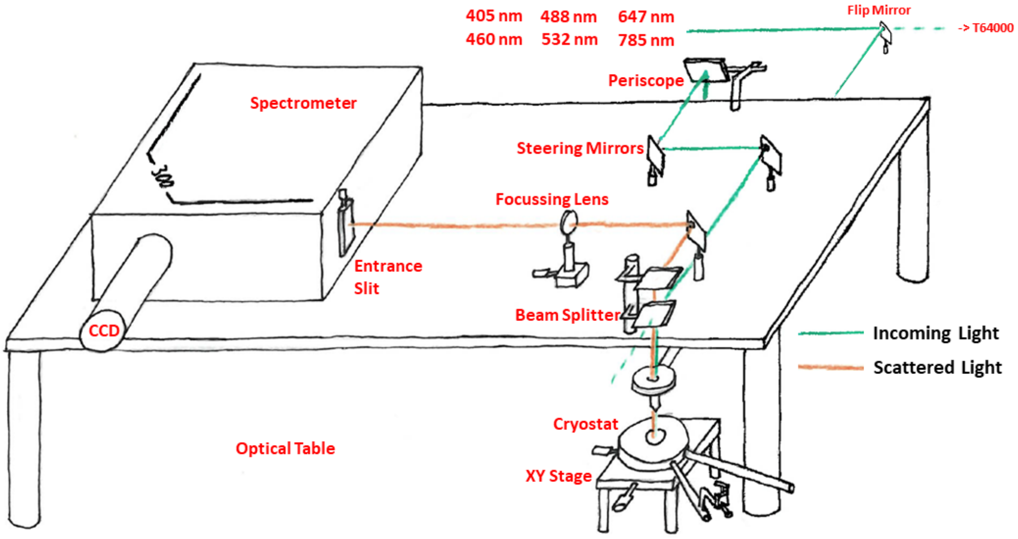

Figure 3.5: Sketch of the high energy Raman setup.

0.5 and working distance 10.6 mm focusses the light onto the sample. The diameter of the spot on a sample is typically around 15 μm. The scattered light is collected and collimated by the same objective, passes through the beam splitter and is directed towards the spectrometer. It is focussed onto the entrance slit by a lens with a diameter of 1" and a focal length of 100 mm. These specifications were chosen to match the numerical aperature NA = f/3.9 of the spectrometer. The width of the entrance slit is adjustable from 10 μm to 3 mm. All measurements with this setup presented in chapter 6 use an entrance slit width of 50 μm, which was chosen for optimised resolution without severe intensity loss.

The grating constant of 150 grooves/mm causes a spatial dispersion of 21.1 nm/mm. Multiplying this with the pixel width and the width of the entire CCD array, respectively, yields the spectral coverage per pixel of 0.42 nm and the spectral coverage of 565 nm for the whole detector. This, combined with the typical entrance slit width of 50 μm, results in a spectral resolution of 1.05 nm.

The Peltier cooling of the CCD minimises the dark current to $<$ 1 electron/h, and the readout noise of the electronics is 3 - 5 counts. The signal is then transfered to a PC and plotted by the Princeton Instruments Lightfield software.

3.3.1 Choice of excitation wavelength

For practical use, spectral coverage, detection efficiency and energy resolution are the main factors that have to be taken into account when selecting the optimal wavelength for a Raman experiment. Specifically, it is possible to define a wavelength range in which the detection process works most efficiently. The quantum efficiency of the grating is plotted in fig. 3.6a (orange curve). It is highest in the range between 600 and 800 nm and drops off rapidly for shorter wavelengths. The grating thus defines a lower limit of $\approx$ 400 nm below which detection becomes too inefficient. This limit has no real practical relevance, of course, since incident wavelengths below 400 nm are not commonly used in Raman spectroscopy and the wavelength increases in

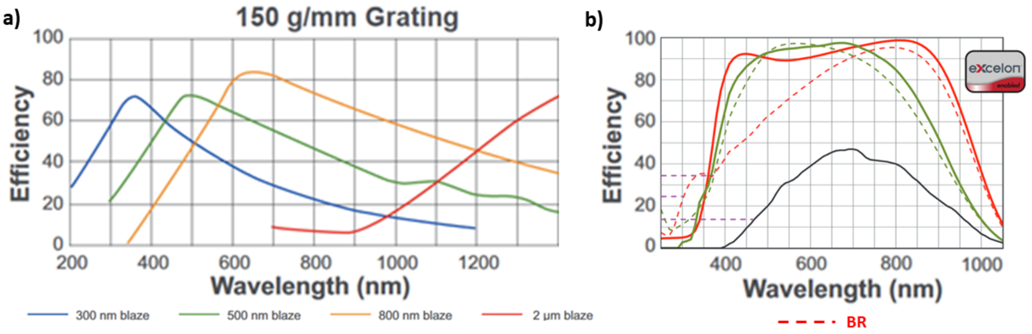

Figure 3.6: Left: Quantum efficiency curves for the 150 grooves/mm grating [Adapted from [4]]. The setup described in this chapter uses the 800 nm blaze (orange curve). Right: Quantum efficiency spectrum of the PIXIS-100 CCD [Adapted from [6]]. This setup uses the *BR* variant (red dashed line).

Stokes scattering.

Fig. 3.6b shows the corresponding curve for the CCD camera (red dashed line). The optimal detection efficiency ($> 90\%$) is achieved in the range 700 - 850 nm, with a steep drop for higher wavelengths. Combining these two curves thus results in an optimised detection range of 600 - 850 nm. Within this range, the spectral resolution (see previous section) of 1.05 nm converts to an energy resolution of ≈ 3 meV. The CCD efficiency also sets a relatively sharp upper detection limit of 1000 nm.

Since energies in Raman spectra are typically not plotted over wavelength or absolute energy but as Raman shift from the incident excitation energy, the position of this optimised detection region and the upper detection limit vary accordingly. By chosing an appropriate laser source, it is thus possible

	785 nm	**532 nm**	**460 nm**	**405 nm**
Most Efficient (meV)	-490 – 120	250 – 850	650 – 1250	1000 – 1600
Upper Limit (meV)	340	1090	1460	1820
"2nd Order" (meV)	790	1165	1348	1531

Table 3.1: Regions of most efficient detection, upper detection limit and position of the apparent 2nd elastic scattering line in the Raman spectra for different excitation wavelengths. Note that for $\lambda_{exc} = 785$ nm, the range of most efficient detection stretches into the Anti-Stokes scattering region.

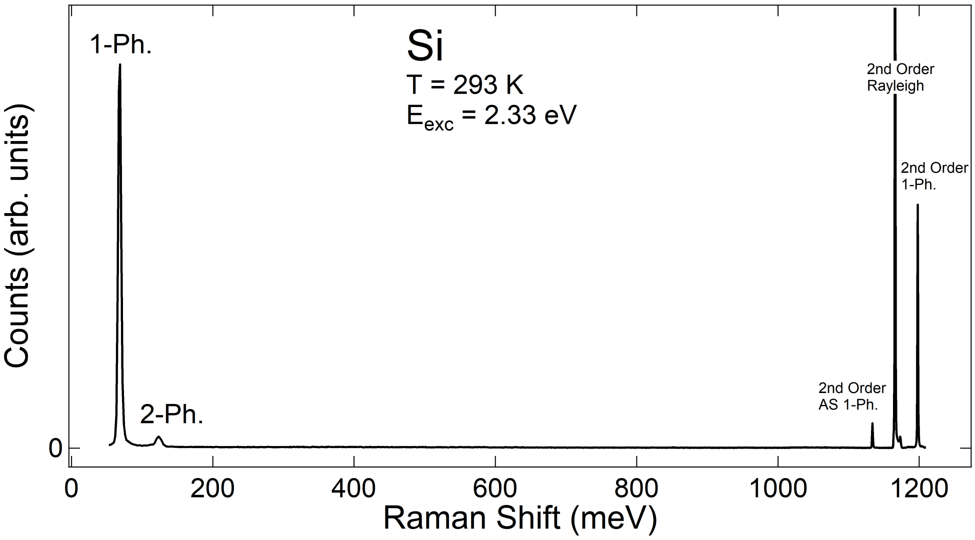

Figure 3.7: Raman spectrum of Silicon recorded with the Princeton HRS-300 spectrometer at T = 293 K with λ_{exc} = 532 nm (E$_{exc}$ = 2.33 eV). The low energy region shows the 1- and 2-phonon peaks (*1-Ph.* and *2-Ph.*, respectively) of silicon. The high energy region shows the 2nd diffraction order of the Anti-Stokes (AS) 1-phonon peak, Rayleigh line, and Stokes 1-phonon peak.

to obtain maximum detection efficiency for the desired energy range. The spectral regions corresponding to the optimal wavelength range and the maximum detection energy for the available incident wavelengths for this thesis work are listed in table 3.1.

Some generalised conclusions can be drawn from this table. Lasers that emit red light are typically unsuited for high energy Raman measurements, because the scattered light will have energies in the infrared regime, for which the detectors are not optimised. If the spectral range of interest is above the phonon regime but below 1 eV, wavelengths around 500 nm provide optimal performance. The detection of higher energy excitations (above 1 eV) necessitates the use of shorter wavelengths at the UV edge of the visible spectrum. Shortening the wavelength, however, has an additional, unwanted effect as soon as the wavelength becomes smaller than the spectral coverage of the detector (λ_{exc} < 565 nm): The diffraction angle off the grating becomes so

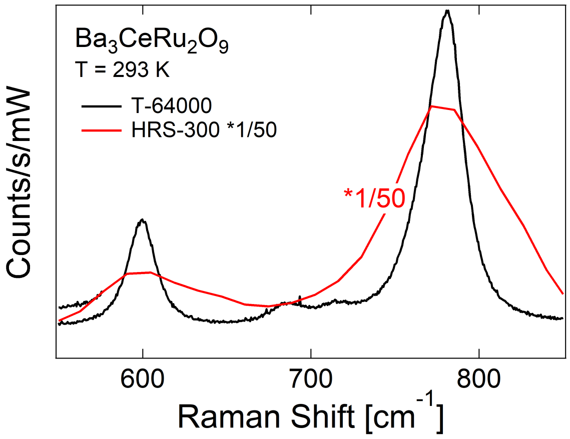

Figure 3.8: Comparison of phonon Raman spectra of BCRO (parallel polarisation) measured with the T64000 (black) and HRS-300 (red) spectrometers.

small that the interference maxima of 2nd order reach the detector as well. When plotted over wavelength λ, the 2nd order interference maximum of the Rayleigh scattered light would appear as an additional peak at twice the incident wavelength. Since Rayleigh scattering is orders of magnitude stronger than Raman scattering, this limits the detectable energy range to λ_{exc} < E < $2\lambda_{exc}$. When plotted in energy units relative to the incident energy E_{exc}, it would appear in that spectrum at an energy E = E_{exc} / 2. This *apparent* position of the 2nd order elastic line is also listed in table 3.1. When measuring at temperatures high enough that excited vibrational states are thermally populated, the 2nd order diffraction signal of the Anti-Stokes Raman scattered light may even appear significantly below $2\lambda_{exc}$ An example of this can be seen in fig. 3.7. It displays a Raman spectrum of Silicon measured with an incident wavelength of λ_{exc} = 532 nm under ambient conditions. The grating angle is chosen so that the elastic scattering line at zero energy is not projected onto the CCD. The 1-phonon- and 2-phonon excitations can be seen at 66 meV and 132 meV, respectively. The 2nd diffraction order of the elastic scattering line appears at 1165 meV, as calculated in tab. 3.1, with the corresponding Stokes- and Anti-Stokes lines from the phonon on both sides of it. To end this section about experimental setups, table 3.2 provides a comparison of the most relevant spectral parameters between the

	Resolution		**Spec. Coverage**		**Count Rate (Si)**
	cm^{-1}	meV	cm^{-1}	eV	Counts/s/mW
T-64000	2	0.25	600	0.075	≈ 50
HRS-300	40	5	8800	1.09	≈ 1200

Table 3.2: Comparison of parameters between the Jobin Yvon T-64000 and the Princeton HRS-300 spectrometers in for detection at $\lambda \approx 550$ nm: Energy resolution and -coverage, and typical experimental count rates for the Silicon T_{2g} phonon.

two setups discussed. Experimentally, the difference in detection efficiency between the two setups is very large. Comparing the phonon count rates for different materials when excited with a 532 nm laser, the spectra measured with the HRS-300 can show up to 50 times higher intensity. Examples of this can be seen in fig. 3.4 for Ni_3TeO_6 and in fig. 3.8 on $Ba_3CeRu_2O_9$, which will be discussed in detail in chapters 5 and 6, respectively.

3.4 Notes on presentation and analysis of Raman spectra

Raman spectra are typically plotted as two-dimensional graphs with the Raman shift on the horizontal axis and either an absolute count number or a count rate on the vertical axis. Raman shift is not an absolute energy unit, but a measure of the energy loss of the photons in comparison to the energy of the incident photons. The typical unit for Raman shift is cm^{-1}, (*”wavenumbers”*), and is defined as the inverse of the wavelength of the light, or, in commonly used units:

$$\nu(cm^{-1}) = \frac{10^7}{\lambda(nm)} \ . \tag{3.3}$$

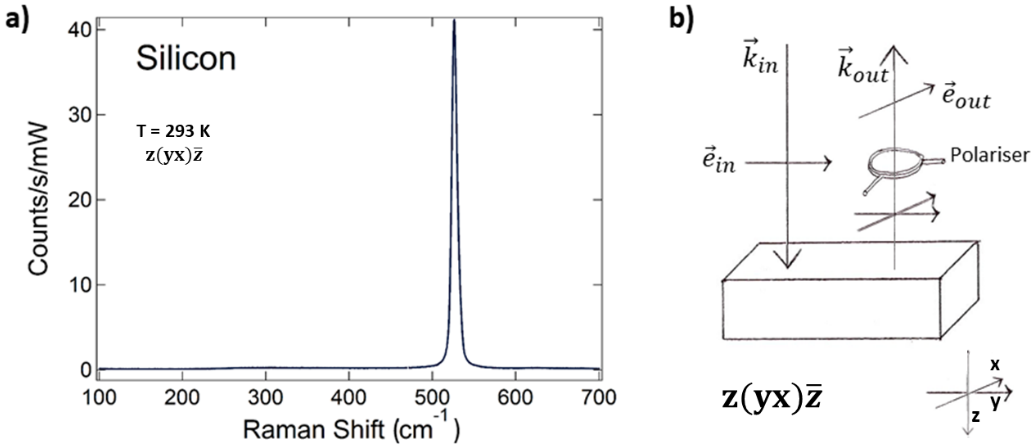

Figure 3.9: (a) Raman spectrum of a silicon single crystal (001) plane in crossed polarisation geometry. The spectrum features a single, Lorentzian shaped Raman peak at 521 cm^{-1}. (b) Schematic Raman scattering setup in $z(xy)\bar{z}$ geometry.

Alternatively, Raman shifts can also be expressed in the energy unit millielectronvolt (meV), which is linearly related to wavenumbers:

$$E(meV) = hf = \frac{hc}{\lambda} = hc * 10^2 * \nu(cm^{-1}) \approx \frac{\nu(cm^{-1})}{8.06554} \ , \tag{3.4}$$

with h the Planck constant in units of meV/Hz and c the speed of light. The Raman shift of an excitation is independent of the chosen excitation wavelength. The count number on the vertical axis refers to the absolute number of photons counted by the CCD detector, modified by electronic readout noise. It is usually normalised to 1 second of integration time and 1 milliwatt (mW) of incident of power, and thus written as counts/s/mW. Discrete excitations manifest in this spectrum as peaks of finite width. This width is a result of the finite lifetime of excited states, inhomogeneous broadening, and the instrumental resolution. Typically, line shapes are describable by either a Lorentzian function (if the lifetime broadening dominates) or a Gaussian function (if inhomogeneous broadening dominates, or the width approaches the experimental resolution), or a convolution of both. In more complex spectra, discrete and continuous excitations within the same energy region may interact to form spectral lines with more complicated shapes, like Fano resonances [18]. A measured Raman spectrum of the (001) plane of a silicon single crystal can be seen in fig. 3.9a. The experimental scattering geometry is conveyed in Porto's notation [8]. It contains information about the direction of polarisation of the incident and analysed light in relation to either the laboratory frame of reference or the crystal axes. In the typical backscattering configuration, it is of the form $u(vw)\bar{u}$, where u and $\bar{u}$ are the propagation directions and v and w are the polarisation directions of incident and scattered light, respectively. If the incident and/or analysed light is circularly polarised, the letters R and L (for left- and right circularly polarised light) are used instead. As an example, the configuration for a z(yx)$\bar{z}$ measurement is shown in fig. 3.9(b).

Bibliography

[1] H. Kuzmany, *Solid State Spectroscopy: An Introduction*, Springer, Berlin, Heidelberg, 2009

[2] S.F. Parker, *Vibrational Spectroscopy with Neutrons*, in Encyclopedia of Biophysics, G.C.K. Roberts, ed., Springer, Berlin, 2013, pp. 2729-2734

[3] B&W Tek (2016, December 2), *An Introduction to a Spectrometer - The Optical Bench*, AZo Materials, https://www.azom.com/article.aspx?ArticleID=13367

[4] Teledyne Princeton Instruments, *Spectra Pro HRS Series Datasheet* (2018)

[5] Horiba, *Jobin Yvon T64000 System User Manual* (2009)

[6] Teledyne Princeton Instruments, *Pixis 100 Datasheet*

[7] U. Fano, *Effects of Configuration Interaction on Intensity and Phase Shifts*, Phys. Rev. **124**, 1866 (1961)

[8] T.C. Damen, S.P.S. Porto, and B. Tell, *Raman Effect in Zinc Oxide*, Phys. Rev. **142**, 570 (1966)

CHAPTER 4

Raman Optical Activity in Chiral and Polar Ni_3TeO_6

Raman optical activity (ROA) measures the difference in Raman scattering intensity for right- and left circularly polarised light and reflects the chirality of excitations. In solids, ROA is commonly very weak. For some phonons in chiral and polar Ni_3TeO_6, we find a giant ROA with magnitude 100 times higher than commonly reported for solids. A systematic analysis based on a combination of phonon selection rules and ROA equations allows complete separation of the chiral and achiral scattering components. Calculation of ROA values confirms these observations, and establishes dynamic modification of the interband Berry curvature through phonon excitation as the origin of ROA in solids.

This chapter is based on a manuscript that is being prepared for submission to a peer-reviewed journal. In accordance with the stylistic requirements of the journal, this chapter uses American English spelling.

4.1 Introduction

Chirality, the breaking of all inversion symmetries of static objects or dynamic motions, is one of the fundamental concepts in nature. Its relevance encompasses all fields of science, from the handedness of electroweak interaction to the function of biomolecules in life science. Similarly, it also plays a remarkable role in a plethora of phenomena in condensed matter physics, from the basic, long-known concept of optical activity to more recent discoveries like Klein tunneling of chiral fermions in graphene [1] and orbital momentum monopoles in chiral systems for use in orbitronics [2]. Chiral bosons, or specifically chiral phonons, are a much more recent discovery [3]. The term implies a unidirectional circular motion of atoms. They are expected to have a strong impact on the physical properties of materials [4–7], specifically applications such as controllable phononic heat transport [8–10]. They are also promising as robust information carriers for solid state quantum information applications [11], specifically because they can be selectively manipulated by coupling with circularly polarized light [9, 12]. Raman scattering has recently been rediscovered [9, 13–15] as a detection method for chiral systems by utilizing the phenomenon of linear wave-vector shifts that lead to energy splitting of degenerate phonon modes close to the Γ point [16–21], but the small momentum transfer from visible light to the material causes the effect to be extremely weak. Using higher energy photons in one way to circumvent this problem [22]. Another way to detect chirality of vibrations that has been long established in spectroscopy of chiral molecules [23–26] could be Raman optical activity (ROA), which instead of an energy splitting measures the difference in scattering intensity for incident left- or right circularly polarized light (LCP/RCP). This effect, first described by Barron and Buckingham in 1971 [23], originates from the finite influence of magnetic dipole- and electric quadrupole transition moments in chiral systems, besides the conventionally considered interaction in Raman scattering, which assumes electric dipole transitions for both the absorption and emission part of the scattering process. This creates additional, chiral scattering terms in the Raman intensity:

$$I_{Raman} \propto I_{pp} + I_{pm} + I_{p\Theta} + \text{higher orders}, \tag{4.1}$$

where I_{pp} is the usual achiral contribution due to purely electric dipole processes, while I_{pm} and $I_{p\Theta}$ are the chiral electric dipole - magnetic dipole and electric dipole - electric quadrupole contributions. Although ROA has been established first and foremost as a technique for identifying chiral molecules, the principle can be applied just as well to crystals. Nevertheless, only few results for ROA on crystalline materials have been reported, and those mostly show weak effects [28], or aquire chirality only through external influences like magnetic field [29] or chiral charge-density waves [30]. More recently, a ROA-like signature in Raman spectra of $NiCo_2TeO_6$ was attributed to ferroaxial phonons [31].

Ni_3TeO_6 crystallizes in the chiral and pyroelectric R3 structure [32–35], with planes of edge-sharing NiO_6 and TeO_6 octahedra that are stacked in a spiral pattern along the c axis. Below $T_N = 52$ K [35, 36], collinear antiferromagnetic order emerges and is accompanied by a spin-induced electric polarization change. Here, we show that in this crystal, some phonons display a ROA that is orders of magnitude higher than what has been reported for naturally chiral solid state systems. Additionally, selection rules for the chiral and achiral scattering contributions allow for complete separation of the two components in the Raman spectrum for one phonon type by controlling the polarization of incident and scattered light.

From the modeling perspective, although tools to compute ROA for molecules exist [37–40], the situation is fundamentally different for a periodic solid: Optical responses are intimately connected to the quantum geometry and topology of the band structure. Transition dipoles are directly related to the components of the quantum geometric tensor, while the magnetic dipole and electric quadrupole are directly related to the interband Berry curvature. So far, only static quantum geometry has been considered, but phonons dynamically split the bands and give rise to time-dependent quantum geometry, which has not been considered before. Here we show that the ROA of phonon

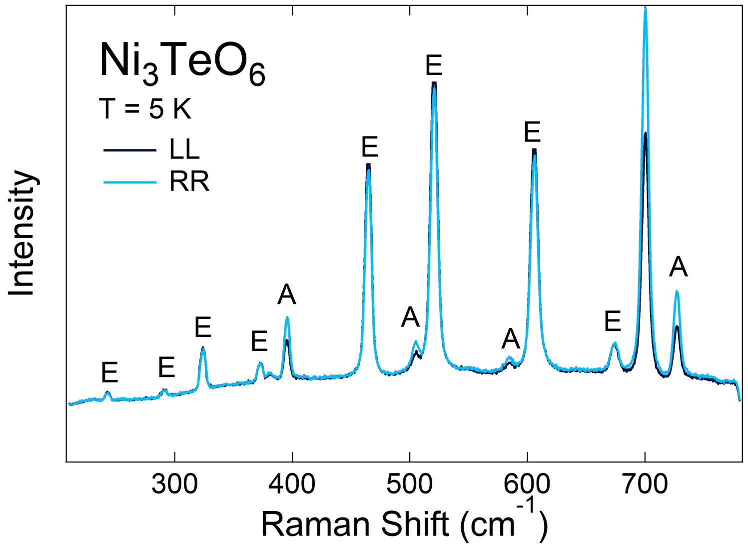

Figure 4.1: Raman spectra of Ni_3TeO_6 at $T = 5$ K in (LL) (black) and (RR) (blue) circular polarization configurations. Labels A/E refer to phonon type.

modes is directly related to how they modify quantum geometry.

Concerning the topic of chiral phonons, we show their existence in Ni_3TeO_6, but their chirality does not contribute to ROA for light propagating along c.

4.2 Raman- and Raman optical activity spectra

Selection rules for electric dipole - electric dipole transitions to excited phonon states are tabulated [43]. For this system, they predict 27 Raman-active phonons; 9 of these are vibrations with the normal coordinate along the c axis of the crystal (A modes). The remaining 18 have their normal coordinate in the ab plane and can be grouped into 9 pairs of energetically degenerate phonons (E modes). Assignment of this symmetry to the measured Raman peaks is done using measurements with linearly polarised light (see Appendix and ref. [44]). In a measurement with circularly polarized light, the electric dipole - electric dipole signatures of the A modes are detectable exclusively in cross-circular (LR and RL) geometries, while those of the E modes are

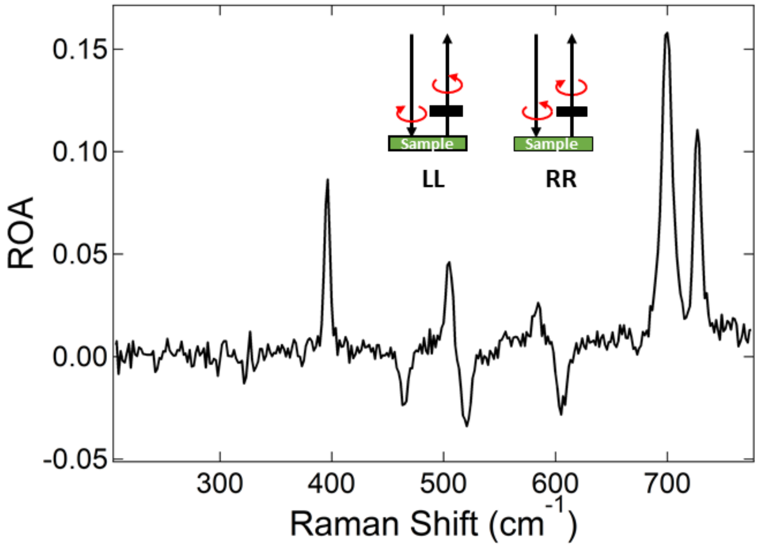

Figure 4.2: ROA spectrum obtained from the spectra in fig. 4.1 through eq. 4.2. Inset: Schematic depiction of co-circular LL/RR geometries.

detectable exclusively in co-circular (LL and RR) geometries.

The difference in scattering intensity for LCP and RCP is visualised by calculating the Raman optical activity

$$\Delta = \frac{I_R - I_L}{I_R + I_L}, \tag{4.2}$$

where the index R/L refers to the right- or left circular polarization of incident light. The helicity of analyzed light can be the same as that of the incident light (co-circular ROA) or opposite (cross-circular ROA).

Theoretical considerations [46] predict that a difference in scattering intensity for incident LCP/RCP, and thus finite ROA, can only occur for measurements in co-circular geometries. For cross-circular geometries, all chiral contributions to the scattering intensity should disappear, and thus the spectra measured in RL and LR configuration should be identical.

Fig. 4.1 shows the Raman spectra in co-circular LL (black line) and RR (blue line) configurations. The 8 peaks at energies 243 cm^{-1}, 291 cm^{-1}, 313 cm^{-1}, 362 cm^{-1}, 464 cm^{-1}, 521 cm^{-1}, 606 cm^{-1}, and 674 cm^{-1} are 8 of the

9 E modes expected for this crystal, the 9th mode likely being too weak to be observed. Surprisingly, most of the A modes (cf. Appendix and [44]) are also detectable here, albeit with significantly reduced intensity. Notably, the peak intensity of most phonons is different in RR and LL geometry. This is most visible for the strongest A modes at 385 cm^{-1}, 694 cm^{-1} and 715 cm^{-1} . Fig. 4.2 shows the ROA spectrum calculated from the above spectra with eq. 4.2. It shows that phonons of both A and E symmetry contribute. The A modes always show positive ROA, while the E modes, show negative ROA. The highest values are observed in the energy region between 680 cm^{-1} and 720 cm^{-1}, peaking around 17%. This exceeds the magnitude of typically reported ROA values by a factor of 100 at least. The broadness of the peak in the ROA spectrum around 690 cm^{-1} suggests the presence of an additional A mode at 691 cm^{-1}, which would complete the set of A modes expected for this space group. The phonons at lower energies show smaller ROA values between 1 and 5%.

Since the Raman selection rules forbid an appearance of achiral electric dipole - electric dipole scattering I_{pp} for the A modes in LL and RR spectra, their signatures in fig. 4.1 can be interpreted as stemming exclusively from the chiral I_{pm} and $I_{p\Theta}$ scattering contributions. The fact that a simple polarization-selective measurement allows for complete separation of pure electric transition dipole- and higher order multipole scattering for the A modes provides an easy way to analyse the latter without an influence of the achiral scattering. Integrating the spectral peaks from the A modes in co- and cross-circular polarisation measurements tells us that the chiral scattering is approximately 80 times weaker than its achiral counterpart.

To illustrate the temperature dependence of the effect, the development of ROA with increasing temperature is plotted in fig. 4.3 (see Methods section for details). Within the magnetically ordered phase, the ROA magnitude stays approximately the same, slightly increasing from 22% at 5 K to 24% at 40 K. Around the transition to the paramagnetic state at T$_N$ = 52 K, it shows a sharp jump up to 30%. This corresponds to an increase by a factor 1.25. Above that temperature, the integrated ROA is constant within error bars. For higher temperatures (T > 100 K), determination becomes

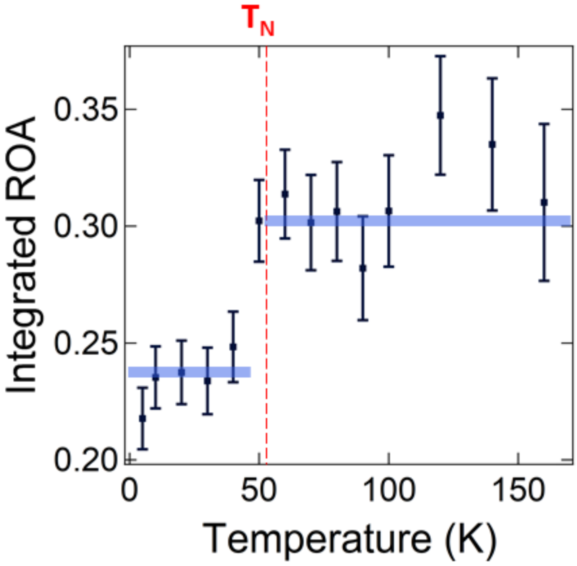

Figure 4.3: Temperature dependence of ROA for the strongest feature in the Raman spectrum around 695 cm^{-1}.

more difficult and the error of the process increases because of the declining intensity of the spectral features.

4.3 Modelling

Calculations of ROA are implemented for molecules in quantum chemistry codes [47], although, to the best of our knowledge, no implementation for periodic crystals exists at the moment. We develop a computational approach in the spirit of frozen phonon framework.

The Hamiltonian for an electron interacting with the electromagnetic field of light is:

$$H = \frac{1}{2m}\left[\hat{\boldsymbol{p}} - \frac{e}{c}\boldsymbol{A}(\boldsymbol{r})\right]^2 - e\boldsymbol{E}\cdot\boldsymbol{r}. \tag{4.3}$$

Taylor expanding for small $\boldsymbol{E}$, $\boldsymbol{A}$ and using the symmetric gauge $\boldsymbol{A} = \frac{1}{2}[\boldsymbol{B}\times\boldsymbol{r}]$, we obtain for the interaction with light:

$$V = -E_i r_i - \frac{e\epsilon_{ijk}B_i r_j p_k}{mc} - e\frac{\partial E_i}{\partial r_j} r_i r_j, \tag{4.4}$$

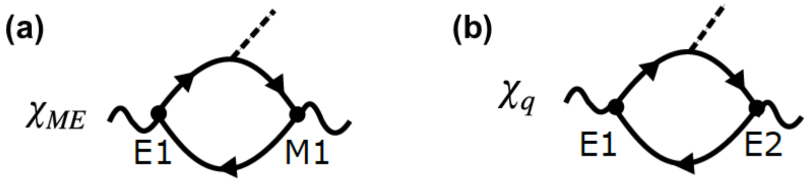

Figure 4.4: Dominant processes leading to non-resonant Raman optical activity. Contribution from (a) magneto-electric susceptibility χ_{ME} with electric dipole-magnetic dipole vertices and (b) quadrupolar susceptibility χ_q with electric dipole-electric quadrupole vertices.

where Einstein summation over repeated indices i, j, k is assumed and the three terms represent the electric dipole (E1), magnetic-dipole (M1) and electric-quadrupole (E2) contributions. Defining the polarization vectors of incoming and outgoing circularly polarized electromagnetic waves as $\boldsymbol{E}_i^R = \boldsymbol{E}_o^L \propto (1, i, 0)$, $\boldsymbol{E}_o^R = E_i^L \propto (1, -i, 0)$, with the time evolution $\boldsymbol{E}_{i,o} \propto e^{-i\omega_{i,o}t}$, the optical absorption is proportional to $\frac{\partial R}{\partial u_\nu} u_\nu e^{-i\Omega t}$ with the scattering operator

$$R \propto |\langle v|V|c\rangle|^2/(\omega_i - \omega_f \pm \Omega), \tag{4.5}$$

containing E1×E1, E1×E2, E1×M1 contributions. The photon absorption rate in the latter two processes corresponds to the imaginary part of the photon self-energy, Fig. 4.4: The photon, indicated by a wavy line, creates an electron-hole pair (solid lines), one of which emits or absorbs a phonon (dashed line) before they recombine.

From the Maxwell equation $-\frac{\partial B}{dt} = \nabla \times E$, assuming for a plane wave $E, B \propto e^{-i\omega t}$, we find $\boldsymbol{B} = \boldsymbol{k} \times \boldsymbol{E}/\omega$. Since each term in V is linear in E, the resulting absorption intensity is $I \propto |E_i E_o|^2$, therefore, we can write $I = |E_i^o R_{ij} E_j^i|^2$. Each term under the absolute value comes from a product of two matrix elements from V, thus leading to E1×E1, E1×E2, E1×M1 terms. The E1×E1 term results in a symmetric R_{ij}, while the ROA is proportional to the imaginary part of the antisymmetric matrix elements:

$$\Delta \propto \mathrm{Im} \frac{R_{12}}{R_{11} + R_{22}}$$

Terms with E2 and M1 are proportional to the photon wave vector k, i.e.

represent spatial dispersion. In nonresonant Raman spectra, the Stokes peak intensities can be computed within the Placzek approximation, which considers only the terms in the polarizability, linear in phonon amplitudes:

$$\begin{aligned} I^\nu &\propto |e_i \cdot R^\nu \cdot e_s|^2 \frac{n_\nu + 1}{\omega_\nu}, && (4.6) \\ R^\nu_{lm} &= \sum_{k,\gamma} \frac{\partial^3 \varepsilon^{el}}{\partial E_l \partial E_m \partial u_{k\gamma}} \frac{w^\nu_{k\gamma}}{\sqrt{M_\gamma}}, && (4.7) \end{aligned}$$

where R^ν is the Raman tensor, e_i and e_s are the polarization vectors of incoming and scattered photons, parallel to the electric field of light, and n_ν and ω_ν are the Bose-Einstein occupation and the frequency of the phonon state ν. The Raman tensor R^ν_{lm} for the phonon mode ν is expressed through the derivative of the total energy with respect to the photon fields $\boldsymbol{E}_i, \boldsymbol{E}_o$ and a phonon amplitude $u_{k\nu}$, equal to the projection of the ionic displacements on the mode polarization vector $w^\nu_{k\gamma}/\sqrt{M_\gamma}$. The triple derivative here is essentially the derivative of the polarizability $\chi_{lm} = \partial^2 \varepsilon^{el}/\partial E_l \partial E_m$ with respect to the phonon mode amplitude.

Using $\epsilon = 1 + 4\pi\chi = 1 + 4\pi i\sigma/\omega$ and substituting (4.6) in (4.2), we find that the ROA is proportional to the antisymmetric component of the optical conductivity (see appendix for details)

$$\Delta_\nu = -i \frac{d}{du_\nu} \left(\frac{\sigma_{xy} - \sigma_{yx}}{\sigma_{xx} + \sigma_{yy}} \right). \tag{4.8}$$

Hence, we expressed the ROA in terms of derivatives of the off-diagonal matrix element of optical conductivity with respect to the phonon amplitudes and approximate it by freezing finite displacements of individual phonon modes. In Cartesian coordinates with the z axis along the C_3 rotational axis we have $\sigma_{xx} = \sigma_{yy}$ and $\sigma_{xy} = -\sigma_{yx}$, therefore $\Delta = -4i\sigma_{xy}/\sigma_{xx}$.

The off-diagonal component of the optical conductivity σ_{xy} at non-absorbing frequencies in an antiferromagnet has contributions from the electric dipole-magnetic dipole and electric dipole-electric quadrupole processes, illustrated in Fig. 4.4. These contributions arise from first order spatial dispersion in

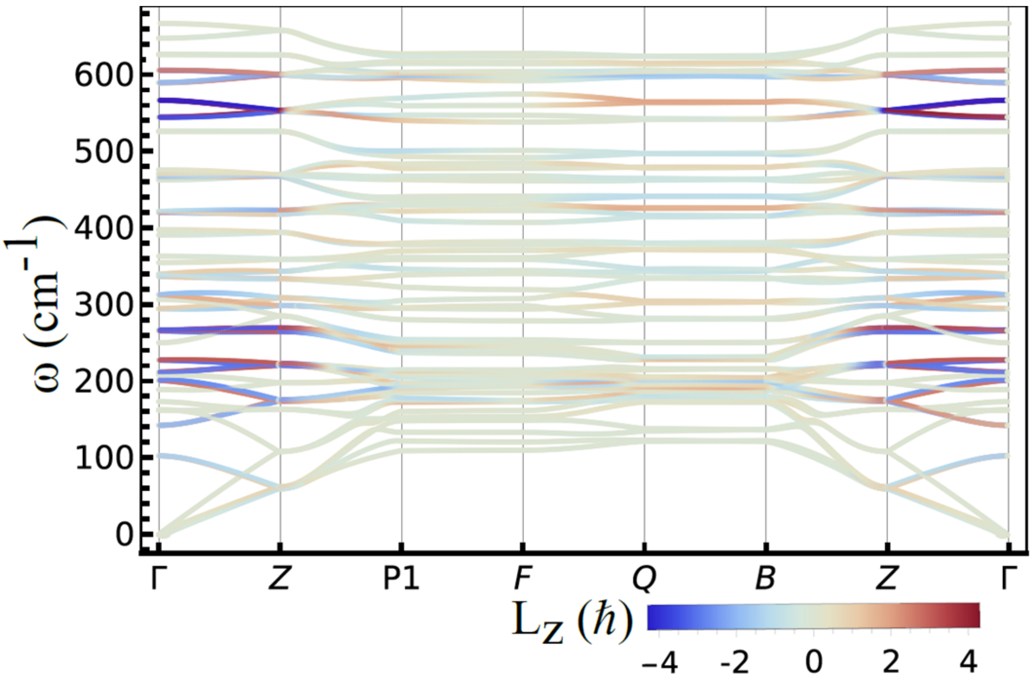

Figure 4.5: Phonon dispersion in the Brillouin zone, with the color encoding phonon angular momentum.

the conductivity tensor,

$$\sigma_{ab}(q,\omega) = \sigma^0_{a,b}(\omega) + i\sigma_{abc}(\omega)q_c, \tag{4.9}$$

with σ_{abc} expressed in terms of the Berry connection and curvature [48]. The doubled magnetic unit cell has AFM ordering ↑↓↓↓↑↑ of magnetic Ni ions positioned along the three-fold rotation axis. The phonon dispersion for Ni_3TeO_6 was computed using DFPT as implemented in VASP code and is shown in Fig. 4.5. The color of phonon branches encodes the phonon angular momentum $L_z = [\boldsymbol{e} \times \dot{\boldsymbol{e}}]$. Chiral phonons, representing circular rotations of ions within xy plane, clockwise and counterclockwise, are highlighted in red and blue.

The thermal amplitudes of individual phonon modes are

$$m_\nu \omega_\nu^2 u_\nu^2 = \hbar\omega_\nu \left(n_{BE}(\hbar\omega_\nu/T) + \frac{1}{2} \right),$$

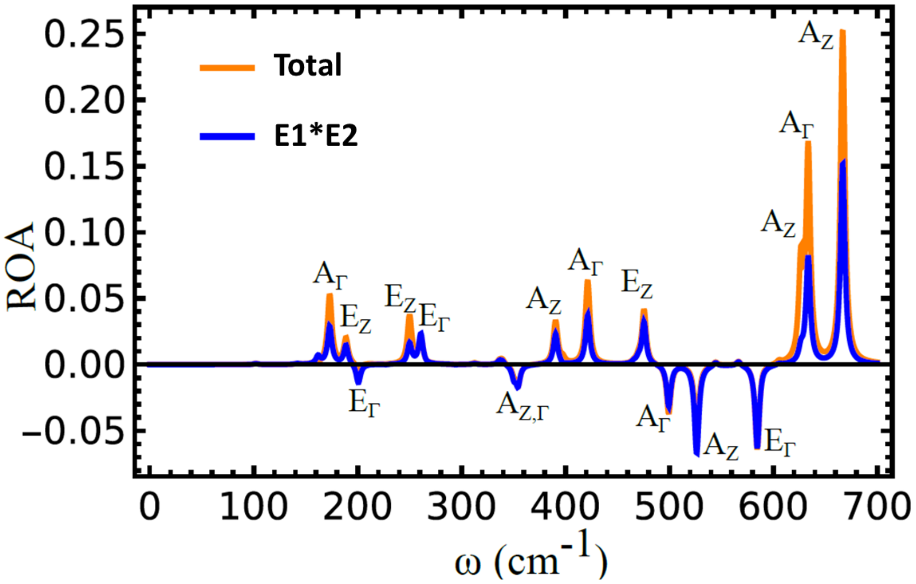

Figure 4.6: Raman optical activity (total, red line) and electric quadrupole contribution (blue line). The irreducible representations of the phonon modes A and E are indicated. The subscripts z and Γ denotes whether the mode belongs to magnetic unit cell or non-magnetic cell.

resulting in $u_{\nu,T} = [(2n_{\nu,T} + 1)\ell_\nu^2]^{\frac{1}{2}}$, where n_{BE} is the Bose-Einstein occupation of the ν-th mode and $\ell_\nu = (\hbar/(2M_p\omega_\nu))^{1/2}$ is the corresponding zero-point vibrational amplitude, with M_p denoting the proton mass.

4.3.1 Electronic band structure calculations

The above explained multipole degrees of freedom are closely related to the electronic band structure in periodic solids. The E modes contribute to ROA in the $E1 - M1$ channel when the magnetic field of light is in-plane, while the A modes contribute in $E1 - E2$ channel. The highest-frequency phonon modes correspond to displacements of light oxygen atoms, whose p-orbitals have large polarizability, thus delivering the largest ROA contribution. We computed the M1 and E2 contributions separately. Fig. 4.6 shows the total conductivity calculations and E2 contributions. The highest energy modes are found to contribute the most and we analyze them through electronic band structure topology. The experiment is performed across T_N, where a

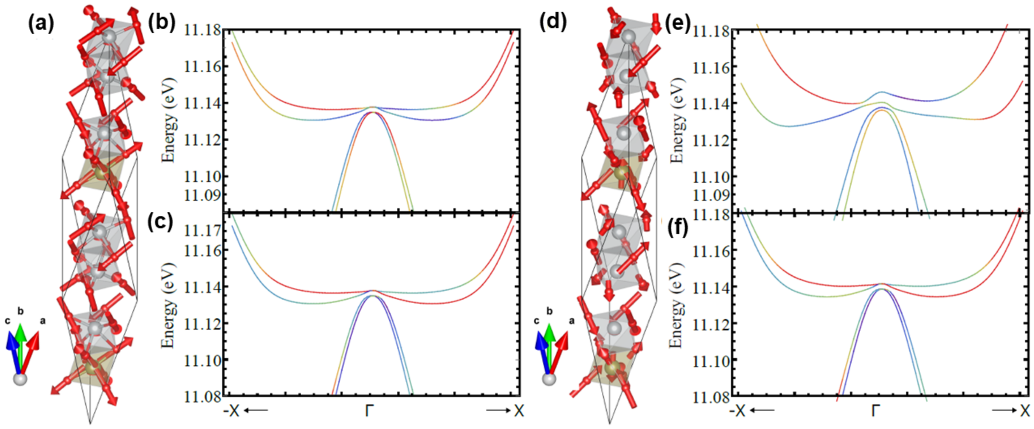

Figure 4.7: (a) The A8 mode with displacements shown in red arrows. (b-c) Electronic band structure with and without A8 mode frozen. (d) A7 mode and (e-f) electronic band structure with and without A7 mode frozen.

pronounced jump in ROA signal is observed. This necessitates consideration of the magnetically ordered unit cell. In the AFM phase, the unit cell doubles along the polar axis compared to the nonmagnetic case . In our analysis we therefore include phonons modes at both the Γ and Z points. The band structure analysis reveals that the dominant ROA contributions arise near the "Γ" point. Consequently, we focus on the zone center to uncover the underlying microscopic mechanism.

Our calculations show that the $A7$ phonon mode induces a splitting of the top valence bands by approximately 0.1 meV (fig. 4.7) – a remarkable observation, since this mode exhibits the largest ROA response. Importantly, this splitting is related to the phonon mode in presence of magnetic ordering. Thus, in the magnetically ordered state, the contributions from the Γ and Z phonon modes compete, whereas above T_N this competition is absent. The jump in ROA across T_N is therefore fully consistent with the calculated response. Furthermore, the bands at the Γ point exhibit a Rashba-like crossing. A detailed analysis of this crossing reveals a sharp change in orbital character at the intersection, giving rise to a pronounced orbital magnetization contribution.

4.4 Conclusion

We employed circularly polarized Raman spectroscopy in backscattering geometry to measure the Raman optical activity of Ni_3TeO_6 above and below the magnetic ordering temperature $T_N = 52$ K. Both types of phonon modes show huge intensity differences for incident left- and right circularly polarized light, leading to peak ROA values of $\approx 17\%$. The origin of ROA are strong, chiral magnetic dipole- and electric quadrupole transition moments. A new computational approach shows that these contributions are induced by a modification of the quantum topology of the system, i.e., the Berry curvature of the electronic band structure. This previously unrecognized connection between band topology and chiral scattering contributions establishes ROA, which is primarily used as a technique to research the chirality of molecules, is a suitable probe for solid samples as well.

The detection of a ROA signal in a material with a magnetic phase transition also made it possible for the first time to analyze the influence of such a transition on the chiral scattering contributions. We showed that the ROA magnitude of the phonon that contributes the most changes significantly at T_N because the doubling of the unit cell adds a competing contribution from another phonon mode.

Calculations of phonon angular momentum additionally enabled the identification of chiral phonons in the system, and establishes that the chirality of a phonon is not intrinsically connected to its ROA.

Acknowledgements

The authors would like to thank S.-W. Cheong for inspiring discussions. Funded by the Deutsche Forschungsgemeinschaft (DFG, German Research Foundation) – Project number 277146847 – CRC 1238.

4.5 Methods

Samples

High-quality single crystal samples of Ni_3TeO_6 were grown as described in [49] using the chemical transport reaction method and subsequently characterized by x-ray diffraction and polarisation microscopy. The crystals are green, transparent, hexagonal plates with a diameter of $\approx$ 1 mm.

Raman measurements

The sample was mounted in a liquid helium flow cryostat. Measurements were performed on a polished (ab) surface in backscattering geometry using a 532 nm solid state laser with a power of 1 mW at the sample and a spot size of 30 μm. The wavelength lies within a small energy window where the absorption of the sample is minimal [41]. The linearly polarized light from the laser is converted to circular polarisation by a quarter-wave plate in front of the sample, and the backscattered light is converted back to linearly polarised light by the same optics. A linear polariser is then used to select the polarisation to be analysed. This allows for measurement of all 4 dual circular polarisation configurations LL, RR, LR and RL, where the first and second letter denote the helicity of the incident and analysed light, respectively. This setup corresponds to the backscattering dual circular polarisation geometry that has been shown to detect ROA most efficiently and with the least experimental artifacts [42]. Spectra were recorded using a Jobin Yvon T64000 triple grating Raman spectrometer equipped with a liquid nitrogen cooled CCD yielding a total energy resolution well below 1 meV. Since there are no phonons at energies below 170 cm^{-1}, we restrict ourselves to the energy range between 160 cm^{-1} and 750 cm^{-1}, thereby covering the entire phonon energy range of this material. Measurements in RR and LL geometry were done at various temperatures between 5 K and 200 K, with 10 K steps between 10 and 100 K and 20 K steps above. The integration time per spectrum was 10 minutes. Additionally, measurements with exposure times of 30 minutes were done in LR and RL geometry at room temperature.

Contributions

This project was conceived by Paul H.M. van Loosdrecht and Markus Grüninger as part of the CRC1238, sub-area B03. Samples were grown and provided by Vladimir Tsurkan and Istvan Kézsmárki (Universität Augsburg). Sample polishing and characterisation with polarisation microscopy and Laue diffraction, Raman spectroscopic measurement and analysis of the data was done by me. Band structure and vibrational patterns were calculated by Ravi Kaushik, Sergey Artyukhin (both Italian Institute of Technology, Genova, Italy), Evgenia V. Komleva and Sergey V. Streltsov (both Ural Federal University, Ekaterinburg, Russia). ROA and phonon chirality were modelled and calculated by Ravi Kaushik and Sergey Artyukhin. The paper draft was written by me and Ravi Kaushik, with input from Thomas Koethe, Markus Grüninger, Sergey Artyukhin and Paul H.M. van Loosdrecht.

Bibliography

[1] M.I. Katsnelson, K.S. Novoselov, and A. Geim, *Chiral tunneling and the Klein paradox in graphene*, Nat. Phys. **2**, 620 (2006)

[2] Y. Yen, J.A. Krieger, M. Yao, I. Robredo, K. Manna, Q. Yang, E.C. McFarlane, C. Shekhar, H. Borrmann, S. Stolz, R. Widmer, O. Gröning, V.N. Strocov, S.S.P. Parkin, C. Felser, M.G. Vergniory, M. Schüler, and N.B.M. Schröter, *Controllable orbital angular momentum monopoles in chiral topological semimetals*, Nat. Phys. (2024), https://doi.org/10.1038/s41567-024-02655-1

[3] H. Zhu, J. Yi, M.-Y. Li, J. Xiao, L. Zhang, Ch.-W. Yang, R.A. Kaindl, L.-J. Li, Y. Wang, and X. Zhang, *Observation of Chiral Phonons*, Science **359**, 579 (2018)

[4] L. Zhang and Q. Niu, *Chiral Phonons at High-Symmetry Points in Monolayer Hexagonal Lattices*, Phys. Rev. Lett. **115**, 115502 (2015)

[5] S.-W. Cheong and X. Xu, *Magnetic chirality*, npj Quantum Mater. **7**, 40 (2022)

[6] S. Park and B.-J. Yang, *Phonon Angular Momentum Hall Effect*, Nano Lett. **20**, 7694 (2020)

[7] J. Cui, E.V. Boström, M. Ozerov, F. Wu, Q. Jiang, J.-H. Chu, C. Li, F. Liu, X. Xu, A. Rubio, and Q. Zhang, *Chirality selective magnon-phonon hybridization and magnon-induced chiral phonons in a layered zigzag antiferromagnet*, Nat. Commun. **14**, 3396 (2023)

[8] N. Li, J. Ren, L. Wang, G. Zhang, P. Hänggi, and B. Li, *Colloqium: Phononics: Manipulating heat flow with electronic analogs and beyond*, Rev. Mod. Phys. **84**, 1045 (2012)

[9] H. Chen, W. Wu, J. Zhu, Z. Yang, W. Gong, W. Gao, S.A. Yang, and L. Zhang, *Chiral Phonon Diode Effect in Chiral Crystals*, Nano Lett. **22**, 1688 (2022)

[10] T. Pandey, C.A. Polanco, V.R. Cooper, D.S. Parker, and L. Lindsay, *Symmetry-driven phonon chirality and transport in one-dimensional and bulk Ba_3N-derived materials*, Phys. Rev. B **98**, 241405(R) (2018)

[11] H. Chen, W. Wu, J. Zhu, S.A. Yang, and L. Zhang, *Propagating Chiral Phonons in Three-Dimensional Materials*, Nano Lett. **21**, 3060 (2021)

[12] E. Oishi, Y. Fujii, and A. Koreeda, *Selective observation of enantiomeric chiral phonons in α-quartz*, Phys. Rev. B **109**, 104306 (2024)

[13] K. Ishito, H. Mao, Y. Kousaka, Y. Togawa, S. Iwasaki, T. Zhang, S. Murakami, J.-I. Kishine, and T. Satoh, *Truly Chiral Phonons in α-HgS*, Nat. Phys. **19**, 35 (2023)

[14] K. Ishito, H. Mao, K. Kobayashi, Y. Kousaka, Y. Togawa, H. Kusunose, J.-I. Kishine, and T. Satoh, *Chiral phonons: circularly polarized Raman spectroscopy and ab initio calculations in a chiral crystal tellurium*, Chirality **35**, 338 (2023)

[15] J. Skórka, K.J. Kapcia, P.T. Jochym, and A. Ptok, *Chiral phonons in binary compounds ABi (A = K, Rb, Cs) with $P2_1/c$ structure*, Mater. Today Commun. **35**, 105888 (2023)

[16] A.S. Pine and G. Dresselhaus, *Linear Wave-Vector Shifts in the Raman Spectrum of α-Quartz and Infrared Optical Activity*, Phys. Rev. **188**, 1489 (1969)

[17] A.S. Pine and G. Dresselhaus, *Raman Spectra and Lattice Dynamics of Tellurium*, Phys. Rev. B **4**, 356 (1971)

[18] J.-P. Pinan-Lucarre, R. Ouillon, and P. Ranson, *Linear wave vector dependence of low-frequency Raman modes in two uniaxial gyrotropic quartz-type materials: α-GaPO$_4$ and α-AlPO$_4$*, Chem. Phys. Lett. **302**, 164 (1999)

[19] S.G. Garasevich, A.V. Slobodyanyuk, and Z.Z. Yanchuk, *Anomalous angular dependence of E-Mode splitting in Raman spectra of ZnP$_2$ and CdP$_2$ uniaxial gyrotropic crystals caused by spatial dispersion*, Phys. Lett. A **197**, 238 (1995)

[20] M.H. Grimsditch, A.K. Ramdas, S. Rodriguez, and V.J. Tekippe, *Piezospectroscopy of Raman lines exhibiting linear wave-vector dependence: α-quartz*, Phys. Rev. B **15**, 5869 (1977)

[21] H.M. Bizek, W. Imaino, A.K. Ramdas, and S. Rodriguez, *Linear wave-vector dependence of zone center optical phonons*, J. Raman Spectrosc. **10**, 106 (1981)

[22] H. Ueda, M. García-Fernández, S. Agrestini, C.P. Romao, J. van den Brink, N.A. Spaldin, K.-J. Zhou, and U. Staub, *Chiral phonons in quartz probed by X-rays*, Nature **618**, 946 (2023)

[23] L.D. Barron and A.D. Buckingham, *Rayleigh and Raman scattering from optically active molecules*, Mol. Phys. **20**, 1111 (1971)

[24] L.D. Barron, M.P. Boogard, and A.D. Buckingham, *Raman Scattering of Circularly Polarized Light by Optically Active Molecules*, J. Am. Chem. Soc. **95**, 603 (1973)

[25] L.D. Barron, M.P. Boogard, and A.D. Buckingham, *Differential Raman Scattering of Right and Left Circularly Polarized Light by Asymmetric Molecules*, Nature **241**, 113 (1973)

[26] L.D. Barron, *Methyl group as a probe of chirality in Raman optical activity*, Nature **255**, 458 (1975)

[27] L.D. Barron and A.D. Buckingham, *Vibrational Optical Activity*, Chem. Phys. Lett. **492**, 199 (2010)

[28] M. Lindner, B. Schrader, and L. Hecht, *Raman Optical Activity of Enantiomorphic Single Crystals*, J. Raman Spectrosc. **26**, 877 (1995)

[29] A. Sahasrabudhe, M.A. Prosnikov, T.C. Koethe, P. Stein, V. Tsurkan, A. Loidl, M. Grüninger, H. Hedayat, and P.H.M. van Loosdrecht, *Chiral excitations and the intermediate-field regime in the Kitaev magnet α-$RuCl_3$*, Phys. Rev. Research **6**, L022005 (2024)

[30] E.M. Lacinska, M. Furman, J. Binder, I. Lutsyk, P.J. Kowalczyk, R. Stepniewski, and A. Wysmolek, *Raman Optical Activity of 1T-TaS_2*, Nano Lett. **22**, 2835 (2022)

[31] V.A. Martinez, Y. Gao, J. Yang, F. Lyzwa, Z. Liu, C.J. Won, K. Du, V. Kiryukhin, S.W. Cheong, and A.A. Sirenko, *Ferroaxial phonons in chiral and polar $NiCo_2TeO_6$*, Phys. Rev. B **112**, 064411 (2025)

[32] R.E. Newnham and E.P. Meagher, *Crystal structure of Ni_3TeO_6*, Mater. Res. Bull. **2**, 549 (1967)

[33] R. Becker and H. Berger, *Reinvestigation of Ni_3TeO_6*, Acta Cryst. **62**, i222 (2006)

[34] X. Wang, F.-T. Huang, J. Yang, Y.S. Oh, and S.-W. Cheong, *Interlocked chiral/polar domain walls and large optical rotation in Ni_3TeO_6*, APL Mater. **3**, 076105 (2015)

[35] I. Živković, K. Prša, O. Zaharko, and H. Berger, *Ni_3TeO_6 - a collinear antiferromagnet with ferromagnetic honeycomb planes*, J. Phys.: Condens. Matter **22**, 056002 (2010)

[36] Y.-S. Oh, S. Artyukhin, J.J. Yang, V. Zapf, J.W. Kim, D. Vanderbilt, and S.-W. Cheong, *Non-hysteretic colossal magnetoelectricity in a collinear antiferromagnet*, Nat. Commun. **5**:3201 (2014)

[37] P. Bour, *Computations of the Raman Optical Activity via the Sum-Over-States Expansion*, J. Comput. Chem. **22**, 426 (2001)

[38] K. Ruud and A.J. Thorvaldsen, *Theoretical Approaches to the Calculation of Raman Optical Activity Spectra*, Chirality **21**:E54 (2009)

[39] S.T. Mutter, F. Zielinski, P.L.A. Popelier, and E.W. Blanch, *Calculation of Raman optical activity spectra for vibrational analysis*, Analyst **140**, 2944 (2015)

[40] S. Luber, *Raman Optical Activity Spectra from Density Functional Perturbation Theory and Density-Functional-Theory-Based Molecular Dynamics*, J. Chem. Theory Comput. **13**, 1254 (2017)

[41] M.O. Yokosuk, H.-S. Kim, K.D. Hughey, J. Kim, A.V. Stier, K.R. O'Neal, J.Yang, S.A. Crooker, K. Haule, S.-W. Cheong, D. Vanderbilt, and J. Musfeldt, *Nonreciprocal directional dichroism of a chiral magnet in the visible range*, npj Quantum Mater. **5**, 20 (2020)

[42] L. Hecht, L.D. Barron, and W. Hug, *Vibrational Raman Optical Activity in Backscattering*, Chem. Phys. Lett. **158**, 341 (1989)

[43] E. Kroumova, M.I. Aroyo, J.M. Perez-Mato, A. Kirov, C. Capillas, S. Ivantchev, and H. Wondratschek, *Bilbao Crystallographic Server : Useful Databases and Tools for Phase-Transition Studies*, Phase Transitions **76**, 155 (2003)

[44] S. Skiadopoulou, F. Borodavka, C. Kadlec, F. Kadlec, M. Retuerto, Z. Deng, M. Greenblatt, and S. Kamba, *Magnetoelectric excitations in multiferroic* Ni_3TeO_6, Phys. Rev. B **95**, 184435 (2017)

[45] M.O. Yokosuk, S. Artyukhin, A. al-Wahish, X. Wang, J. Yang, Z. Li, S.-W. Cheong, D. Vanderbilt, and J.L. Musfeldt, *Tracking the continuous spin-flop transition in* Ni_3TeO_6 *by infrared spectroscopy*, Phys. Rev. B **92**, 144305 (2015)

[46] L.A. Nafie and T.B. Freedman, *Dual Circular Polarization Raman Optical Activity*, Chem. Phys. Lett. **154**, 260 (1989)

[47] J.M.H. Olsen et al., *Dalton Project: A Python platform for molecular- and electronic-structure simulations of complex systems*, J. Chem. Phys. **152**, 214115 (2020)

[48] A. Malashevich and I. Souza, *Band theory of spatial dispersion in magnetoelectrics*, Phys. Rev. B **82**, 245118 (2010)

[49] D. Maluski, M. Langenbach, D. Szaller, S. Reschke, L. Prodan, I. Cámara Mayorga, S.-W. Cheong, V. Tsurkan, I. Kézsmárki, J. Hemberger, and M. Grüninger, *Giant natural optical rotation from chiral electromagnons in a collinear antiferromagnet*, arXiV: 2312.02733v1 (2023)

4.6 Appendix / Supplemental Information

Raman spectra in linear polarization geometry

In order to be able to differentiate between A and E modes, a Raman measurement with linearly polarized incoming and analyzed light has been carried out. The irreducible representation for R3 space group is $\Gamma_{Raman} = 9\ A + 9\ E(x) + 9\ E(y)$. According to the selection rules, the 9 A modes should only be detectable in $z(xx)\bar{z}$ geometry, while the 9 degenerate pairs of E modes should be active in both $z(xx)\bar{z}$ and $z(xy)\bar{z}$ geometries. The result of these measurements at room temperature is shown in fig. 4.8. The incident laser power was 1 mW, and the measurement time was 30 minutes for $z(xx)\bar{z}$ and 75 minutes for $z(xy)\bar{z}$ geometries. The observed phonon energies are listed in table 4.1.

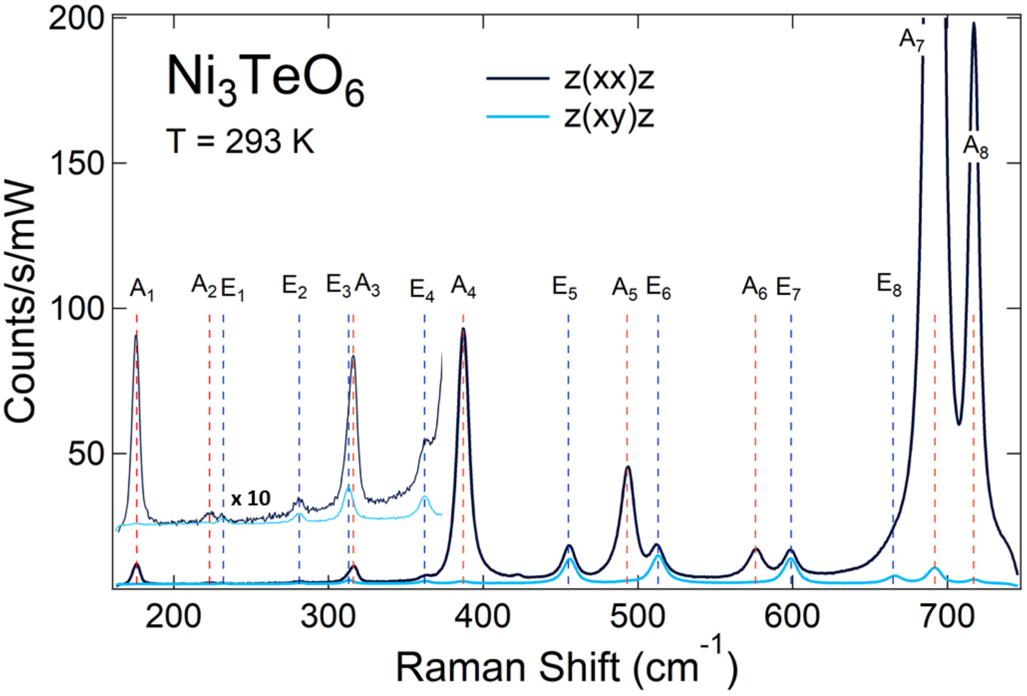

Figure 4.8: Raman spectra of Ni_3TeO_6 measured in linear $z(xx)\bar{z}$ and $z(xy)\bar{z}$ geometries. Labels indicate phonon representation. Inset: Ten times magnified depiction of the low energy region.

Energy (cm^{-1})	Symmetry	Energy (cm^{-1})	Symmetry
175	A	455	E
223	A	493	A
232	E	513	E
280	E	576	A
313	E	599	E
316	A	665	E
362	E	692	A
387	A	717	A

Table 4.1: Phonon mode energies and symmetry assignment at T = 293 K.

Raman spectra in cross-circular geometries

In cross-circular geometries, i.e., RL and LR configuration, all 9 *A* modes should be active, while the 9 pairs of degenerate *E* modes are forbidden. Additionally, there should be no Raman optical activity. The Raman spectra in RL and LR configuration are shown in fig. 4.9. As expected, they show the 8 *A* modes known from fig. 4.8, with no intensity differences between LR and RL, and accordingly no ROA.

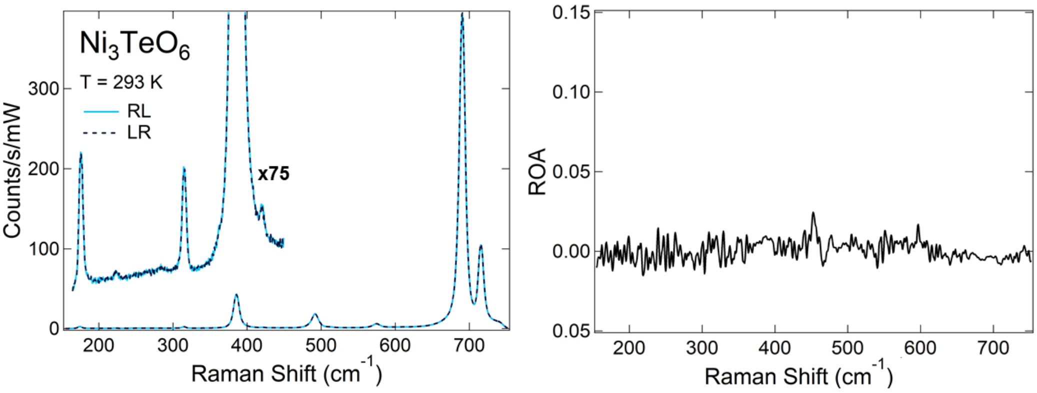

Figure 4.9: Left: Raman spectra of Ni_3TeO_6 in RL and LR configurations. The *A* modes known from fig. 4.8 are visible, and there is no intensity difference for LR/RL. Inset: Magnified version of the low energy region. Right: The ROA spectrum obtained for this geometry is flat.

Sign change in ROA for different domains

The sample of Ni_3TeO_6 used for the measurements in this work shows well separated domains of the L- and R-variant of the crystal structure. While all measurements shown in the main part of this article were measured on the same domain, measurements on the other domain were also done and are shown in fig. 4.10. As expected, the sign of ROA is opposite for the other domain type in the sample.

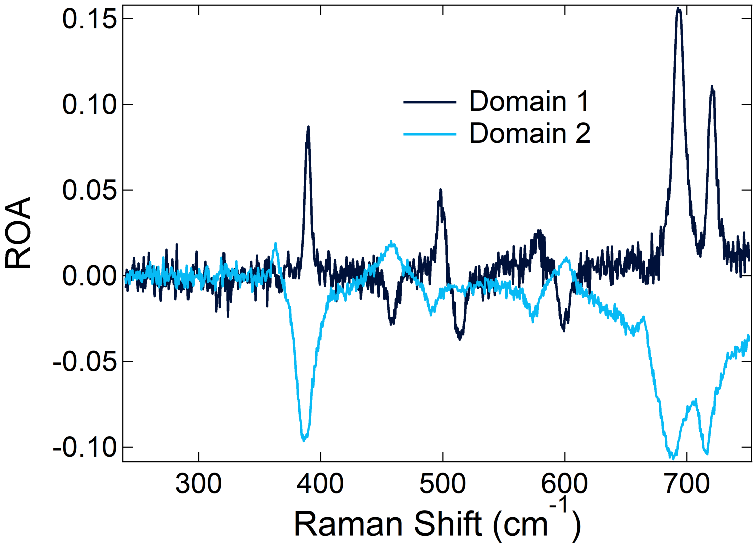

Figure 4.10: ROA spectra of Ni_3TeO_6 measured in the L- and R chiral domains. The spectra show the same features, but with opposite sign.

Proof of equation 7 in main text

In non-resonant Stokes Raman spectra of harmonic solids, under Placzek approximation the peak intensities are computed as:

$$\begin{aligned} I^\nu &\propto |e_i \cdot A^\nu \cdot e_s|^2 \tfrac{n_\nu + 1}{\omega_\nu} && (4.10) \\ A^\nu_{lm} &= \textstyle\sum_{k,\gamma} \tfrac{\partial^3 \varepsilon^{el}}{\partial E_l \partial E_m \partial u_{k\gamma}} \tfrac{w^\nu}{\sqrt{M_\gamma}} && (4.11) \end{aligned}$$

$$\Delta = \frac{I_{RR} - I_{LL}}{I_{RR} + I_{LL}} \tag{4.12}$$

Defining circularly polarized incoming and outgoing light polarization:

$$E_i^R = E_0 \begin{pmatrix} 1 \\ i \\ 0 \end{pmatrix} = E_o^L, E_o^R = E_i^L = E_i^{R*} \tag{4.13}$$

Substituting (4.10) and (4.13) in (4.12),

$$\Delta = \frac{|E_o^R \cdot A \cdot E_i^R|^2 - |E_o^L \cdot A \cdot E_i^L|^2}{|E_o^R \cdot A \cdot E_i^R|^2 + |E_o^L \cdot A \cdot E_i^L|^2} \tag{4.14}$$

$$A_{lm}^{\nu} = \operatorname{Im} \partial \chi_{lm} / \partial u_{\nu}$$

Polarizability is $\chi = i\sigma/\omega$ with $\chi^{+} = \chi, \sigma^{+} = -\sigma$.

The ROA contributions are specific to first order spatial dispersion in the conductivity tensor,

$$\sigma_{ab}(q, \omega) = \sigma_{a,b}^{0}(\omega) + i\sigma_{abc}(\omega) q_c, \tag{4.15}$$

Hence,

$$\sigma_{abc}^{\dagger} = \sigma_{abc}, \sigma_{abc} = \sigma'_{abc} + i\sigma''_{abc}, \sigma_{abc}^{\dagger} = \sigma'_{abc} - i\sigma''_{abc},$$

therefore, substituting, $\sigma_{abc} = \sigma'_{bac}$ and $\sigma''_{abc} = -\sigma''_{bac}$, we obtain

$$\Delta = \frac{-4(\sigma''_{xy})(\sigma'_{xx} + \sigma'_{yy})}{(\sigma'_{xx} + \sigma'_{yy})^2 + (\sigma''_{xx} + \sigma''_{yy})^2 + 4(\sigma''_{xy})^2} \tag{4.16}$$

The factor $\frac{\sigma_{xy}+\sigma_{yx}}{\sigma_{xx}+\sigma_{yy}}$ is negligible as $\sigma_{xx} \gg \sigma_{xy}$ and the denominator ≈ 1. Hence,

$$\Delta = \frac{-4i(\sigma_{xy} - \sigma_{yx})}{(\sigma_{xx} + \sigma_{yy})} \tag{4.17}$$

Reducing by taking into account C_3 rotational symmetry specific to Ni_3TeO_6, $\sigma_{xy} = -\sigma_{yx}$

Raman interaction operators in ab initio and Bloch formalism

To accurately describe ROA, it is essential to account for electronic multipole contributions, which capture the spatial anisotropy of material response functions. In classical electromagnetism, electric (E) multipoles arise from the expansion of the scalar potential and correspond to polar tensors that are even under time reversal, while magnetic (M) multipoles originate from the expansion of the vector potential and correspond to axial tensors that are odd under time reversal. In the independent particle approximation, the multipole expansion terms are explained to arise from matrix generalizations of the intrinsic magnetic moment and quantum metric [1]. The Bloch wavefunctions are defined as:

$$\psi_{n\mathbf{k}}(\mathbf{r}) = e^{i\mathbf{k}\cdot\mathbf{r}} u_{n\mathbf{k}}(\mathbf{r})$$

Here n is the band index, $\mathbf{k}$ is the crystal momentum, and $u_{n\mathbf{k}}(\mathbf{r})$ is a lattice-periodic function.

$$E1^{*}E1 = \mathcal{M}_{fi}^{(dd)} \propto \sum_{n} \frac{\langle f|\hat{\mathbf{r}}|n\rangle\langle n|\hat{\mathbf{r}}|i\rangle}{E_i + \hbar\omega_i - E_n + i\eta}$$

$$E1^{*}M1 = \mathcal{M}_{fi}^{(dm)} \propto \sum_{n} \frac{\langle f|\hat{\mathbf{r}}|n\rangle\langle n|\hat{\mathbf{m}}|i\rangle}{E_i + \hbar\omega_i - E_n + i\eta}$$

$$E1^{*}E2 = \mathcal{M}_{fi}^{(dq)} \propto \sum_{n} \frac{\langle f|\hat{\mathbf{r}}|n\rangle\langle n|\hat{Q}^{\alpha\beta}|i\rangle}{E_i + \hbar\omega_i - E_n + i\eta}$$

With Bloch matrix elements:

$$\langle l_{\mathbf{k}_\alpha}|\hat{\mathbf{r}}_\alpha|n_{\mathbf{k}_\alpha}\rangle = i\langle u_{l\mathbf{k}_\alpha}\,|\nabla_{\mathbf{k}_\alpha} u_{n\mathbf{k}_\alpha}\rangle = A_{\alpha,ln}$$

$$\langle l_{\mathbf{k}}|\hat{\mathbf{m}}_{\alpha\beta}|n_{\mathbf{k}}\rangle = i\langle \nabla u_{l\mathbf{k}_\alpha}| \times \hat{H} - \bar{\epsilon}\,|\nabla_{\mathbf{k}_\beta} u_{n\mathbf{k}_\beta}\rangle - \frac{g_s}{2m_e}\epsilon_{\alpha\beta\gamma}S_{\gamma,ln}$$

Table of calculated phonon energies

Magnetic Unit Cell		Non-Magnetic Unit Cell	
Energy (cm^{-1})	**Symmetry**	**Energy (cm^{-1})**	**Symmetry**
666.5	A_z	633.2	A
626.0	A_z	605.6	E
588.6	E_z	584.0	A
566.0	E_z	544.3	E
525.9	A_z	498.9	A
475.2	A_z	469.8	E
465.5	E_z	421.1	A
421.0	E_z	419.8	E
339.0	E_z	397.5	A
312.3	E_z	390.0	A
266.1	E_z	354.3	A
227.0	E_z	350.1	A
188.7	A_z	336.5	E
173.0	A_z	294.0	E
162.5	A_z	265.5	E
142.0	E_z	260.7	A
		249.9	A
		211.4	E
		200.7	E
		200.5	A
		161.7	A
		101.9	E

Table 4.2: Vibrational modes of Ni_3TeO_6, separated into magnetic unit cell modes and non-magnetic unit cell modes.

Bibliography

[1] Ó. Pozo Ocaña and I. Souza, *Multipole theory of optical spatial dispersion in crystals*, SciPost Phys. **14**, 118 (2023)

CHAPTER 5

Local symmetry breaking and low-energy continuum in K_2ReCl_6

Using polarization selective spontaneous Raman scattering, we have investigated the $5d$ transition metal compound K_2ReCl_6 which displays a series of structural phase transitions. We observe a violation of the Raman selection rules in the cubic high temperature phase as well as a low-energy scattering continuum persistent throughout the investigated temperature range from 300 down to 5 K. The continuum couples to one of the phonon modes at temperatures above the lowest structural phase transition at 76 K. We propose a common origin of these observations caused by disorder in the orientation of the $ReCl_6$ octahedra which locally breaks the long-range cubic symmetry. Consistent results from the related non-magnetic compound K_2SnCl_6 support this interpretation.

This chapter has been published as a peer-reviewed article in Physical Review B [1]. The following is a reformatted version of the original paper as published. Reprinted with permission from Phys. Rev. B 107, 214301 (2023). Copyright 2023 American Physical Society. In accordance with the stylistic requirements of the journal, this chapter uses American English spelling. Reference [15] was updated to reflect its changed publication status.

5.1 Introduction

The material class of composition $A_2M(\mathrm{Cl,Br})_6$ where A is typically an alkaline metal and M a tetravalent main group element or transition metal, features a significant variety of structural and magnetic properties [2]. The parent compound $\mathrm{K_2PtCl_6}$ has a stable cubic antifluorite structure (Fm$\bar{3}$m), with $\mathrm{PtCl_6}$ octahedra on a face centered cubic (fcc) lattice and potassium ions occupying the tetrahedral voids, see Fig. 5.1. Many members of the family display a series of crystallographic phase transitions as a function of temperature [3–7]. A prime example of this class is $\mathrm{K_2ReCl_6}$, which in its high temperature phase has the cubic structure of its parent compound. $\mathrm{K_2ReCl_6}$ shows three structural phase transitions at $T_{\mathrm{c3}} = 111$ K, $T_{\mathrm{c2}} = 103$ K and $T_{\mathrm{c1}} = 76$ K, all of which are easily observable in thermodynamic measurements [8, 9], along with a long-range ordered antiferromagnetic phase below $T_{\mathrm{N}} = 12$ K [10, 11]. Early reports have claimed that all structural phase transitions are driven by soft modes corresponding to consecutive rotations of the octahedra around different axes [12–14]. Upon cooling below T_{c3}, the structure becomes tetragonal with minimal deviations from the cubic phase. The low-temperature phases below T_{c2} possess monoclinic symmetry. Remarkably, the correct crystallographic structure of the tetragonal phase and the nature of the octahedral rotations have been determined only very recently [15]. Lately, the strong interest in unconventional phenomena driven by spin-orbit interactions has spawned renewed attention for this material class, in part motivated by recent theoretical studies which have proposed a spin-orbit assisted Jahn-Teller activity for certain materials of this family [16]. In particular, the t_{2g}^3 configuration of $\mathrm{K_2ReCl_6}$ (Re: $5d^3$) was suggested to be a potential realization.

Previous Raman measurements on this compound at ambient and liquid helium temperatures have identified the Raman active phonon modes [12]. The appearance of additional modes at the phase transitions reflects the lowering of the symmetry, and soft rotary modes have been identified [12, 13] as the driving force behind these transitions. In this work, we investigate $\mathrm{K_2ReCl_6}$ using temperature dependent Raman spectroscopy in two orthogonal polar-

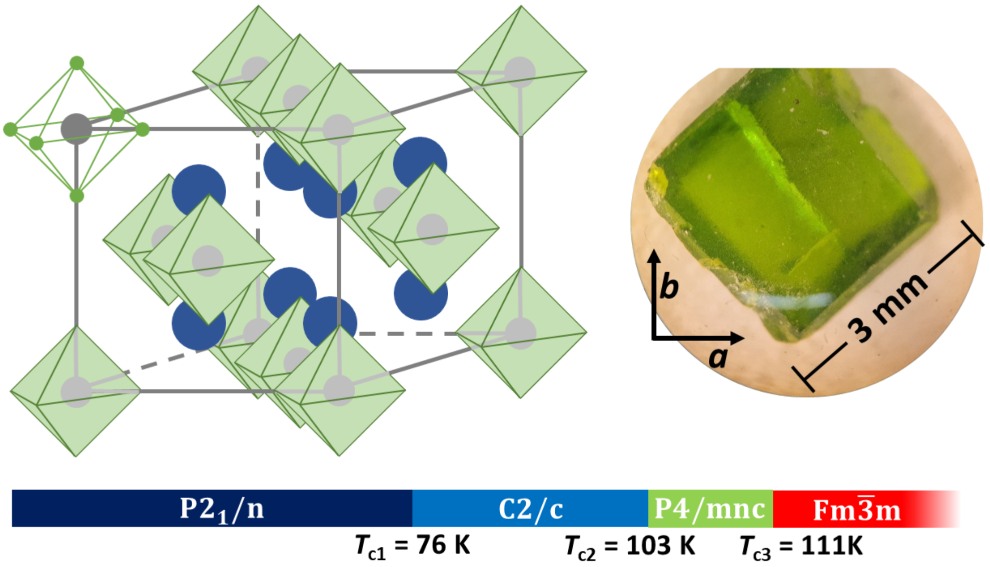

Figure 5.1: Left: Schematic illustration of the room temperature structure with space group $Fm\bar{3}m$. Blue, grey and green spheres represent K^+, Re^{4+} and Cl^- ions, respectively. Right: The (001) surface used for these measurements. The orientation of the cubic a and b axes is indicated. Bottom: The different crystallographic phases and transition temperatures of K_2ReCl_6 within the temperature range covered.

ization configurations extending to lower energies than previously reported. We observe that the cubic symmetry is already broken locally in the high temperature phase. Furthermore, we reveal a low-energy excitation continuum and discuss its relationship to the local symmetry breaking observed at high temperature.

5.2 Experimental

High-quality transparent single crystal samples of K_2ReCl_6 were grown from HCl solution by controlled slow evaporation of the solvent and subsequently characterized by x-ray diffraction, specific heat and susceptibility measurements [15]. A picture of the sample can be seen in Fig. 5.1. The sample was mounted in a liquid helium flow cryostat. Measurements were performed on a polished (001) surface in backscattering geometry with the polarization of incoming light parallel to the cubic a axis using a 532 nm solid state laser with a power of 0.5 mW at the sample and a spot size of 30 μm. The total integration time was eight minutes per temperature step in the range from 5 K up to room temperature.

Spectra were recorded using a triple grating spectrometer equipped with a liquid nitrogen cooled CCD camera yielding a total energy resolution well below 1 meV. The phonon energies were determined by applying a multi-peak fit using Lorentzian and Fano line shapes, where appropriate.

Crystal growth and Raman measurements of K_2SnCl_6 were done analogously with a slightly lower laser power due to stronger scattering as compared to K_2ReCl_6.

5.3 Results

The vibrational spectrum of K_2ReCl_6 is split into two regions. The internal vibrations of the octahedra sit in the higher energy part of the spectrum above 15 meV, while the external lattice modes have energies below 12 meV. The irreducible representation of the Raman active modes in the high-temperature cubic phase is $\Gamma' = 1\mathrm{A}_{1\mathrm{g}} + 1\mathrm{E}_\mathrm{g} + 2\mathrm{T}_{2\mathrm{g}}$, where one of the $\mathrm{T}_{2\mathrm{g}}$ modes is the external potassium mode and the remaining three modes are internal vibrations of the octahedra. By symmetry, the selection rules predict that in our experimental geometry, the $\mathrm{A}_{1\mathrm{g}}$ and E_g modes are detectable exclusively in the (xx) polarization configuration, where only the component of scattered light with the polarization vector parallel to that of the incoming light is analyzed, while the two $\mathrm{T}_{2\mathrm{g}}$ modes only appear in the (xy) polarization configuration, where the polarization vectors of incoming and analyzed light are perpendicular. The Raman spectrum of the room temperature phase in these two configurations is shown in Fig. 5.2. The four Raman active modes can be seen at the energies of 10 meV, 22 meV, 37 meV and 44 meV, respectively, in agreement with the values reported in previous Raman scattering experiments [12] and density of states calculations [17].

The comparably weak external phonon mode at $\approx$10 meV is shown 10 times expanded in the inset of Fig. 5.2. It has a strongly asymmetric Fano

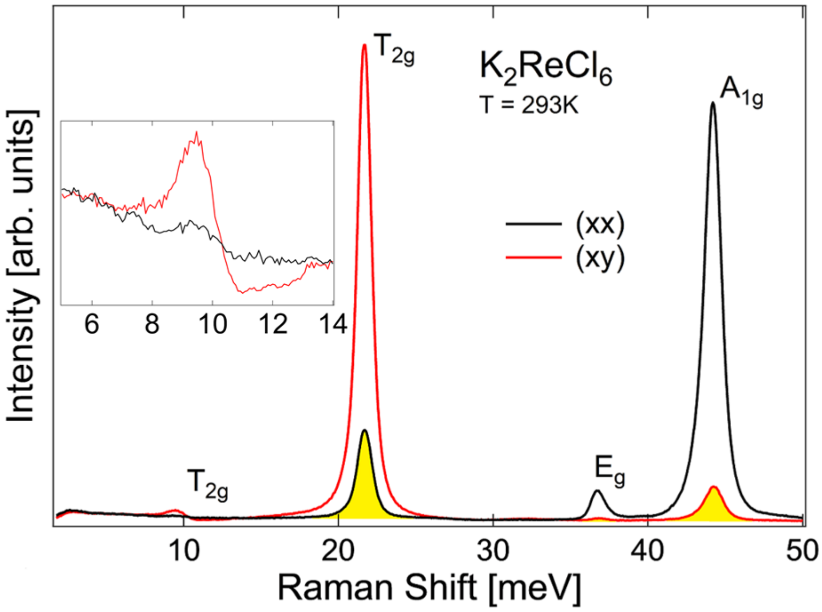

Figure 5.2: Raman spectra of K_2ReCl_6 at $T = 293$ K in (xx) (black) and (xy) (red) polarization configurations. Yellow areas indicate the violation of cubic selection rules. The inset shows a blow-up of the low-energy region containing the lattice phonon.

line shape, which indicates an interaction of the vibrational excitation with a scattering continuum [18]. Indeed, such a continuum is present in our data at energies reaching up to at least 12 meV. We note that previous reports have failed to resolve this low-energy continuum due to less efficient suppression of elastic scattering from the excitation light source.

As marked by the yellow areas in Fig. 5.2, the cubic selection rules are not perfectly fulfilled in this crystal. The spectrum taken in (xy) configuration contains both the A_{1g} and E_g modes with about 5% of their intensity in the (xx) configuration. Similarly, the T_{2g} modes appear in the (xx) spectrum with 10% of their intensity from the (xy) polarization. Since the sample has been oriented using Laue diffraction, and both the experimental alignment and polarization of the light have been carefully verified, so-called leakage of a scattering signal into the wrong polarization channel due to misalignment or insufficient polarization can be ruled out. Moreover, the Raman tensor

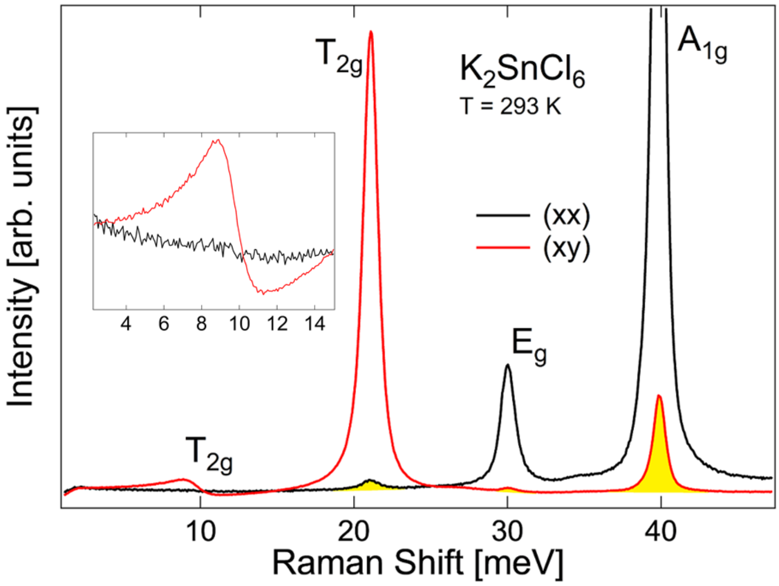

Figure 5.3: Room temperature Raman spectra of K_2SnCl_6 in (xx) (black) and (xy) (red) polarization configuration, cf. fig. 5.2.

of the A_{1g} mode is rotationally invariant, therefore it is excluded to observe this mode in (xy) configuration for cubic symmetry.

In order to test whether or not the experimental observations might be related to the electronic or magnetic properties of the material, we have investigated the related non-magnetic compound K_2SnCl_6, where Sn has a filled shell $4d^{10}$ configuration. The room temperature Raman spectra for both the (xx) and (xy) configurations shown in fig. 5.3 reveal a violation of the cubic selection rules as well as a low-energy scattering continuum, consistent with the results of K_2ReCl_6. We thus conclude that the origin of these observations must be related to the properties of the lattice structure rather than its electronic or magnetic nature. The same features can also be observed in a spectrum of K_2ReCl_6 measured with an excitation wavelength of 488 nm (not shown), which excludes that these features are caused by resonance scattering effects.

We now turn to the temperature dependence of the Raman spectra of K_2ReCl_6. We focus on the low energy region below 13 meV shown in fig. 5.4 for both

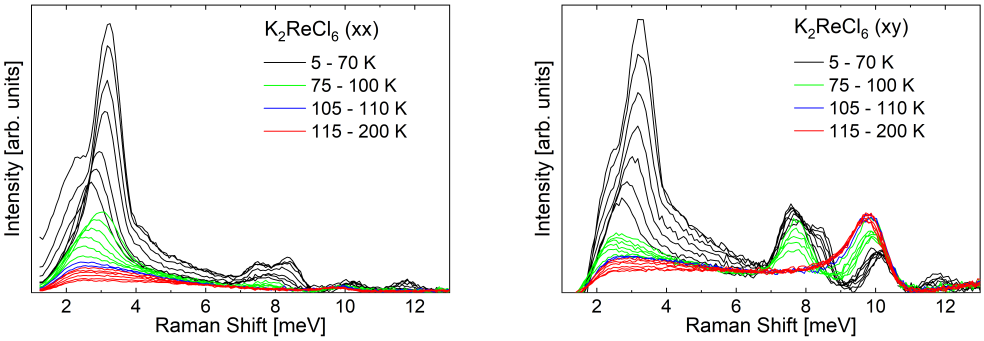

Figure 5.4: Bose-factor corrected Raman spectra of K_2ReCl_6 in the energy region below 13 meV at temperatures between 5 and 200 K; Left: (xx) polarization configuration; Right: (xy) polarization configuration. The different colors represent the four distinct crystallographic phases.

(xx) (left) and (xy) (right) polarization configurations. To extract the bare scattering strength, a constant offset has been subtracted from the raw data, and the prefactor $(n + 1)$ of the scattering cross section, with the energy- and temperature-dependent Bose occupation n, has been corrected for. Despite the lowering of the symmetry at the transition from the cubic (shown in red) to the tetragonal (blue) phase, no additional phonons are detected below $T_{\mathrm{c}3} = 111$ K, in agreement with previous reports on several materials in this family [19–24]. We infer that the small degree of deformations in the tetragonal phase results in a minute energy splitting of modes which is insignificant in comparison to the lifetime and therefore not observed.

The transition from tetragonal to the monoclinic C2/c structure at $T_{\mathrm{c}2} = 103$ K is clearly marked by two additional modes in the spectra (green). At 7.6 meV a reasonably strong mode emerges below $T_{\mathrm{c}2}$ in both polarization configurations, though more pronounced in (xy). Around 3 meV, another mode grows out of the low energy continuum in (xx) configuration. Right below the transition, the 3 meV mode is rather weak and thus difficult to distinguish from the strong scattering continuum, but it gains weight and definition towards lower temperatures. Below $T_{\mathrm{c}1} = 76$ K, the mode also appears in (xy) configuration, cf. black spectra in fig. 5.4 (right). As can be seen in Fig. 5.5 (a), its excitation energy shows a weak anomaly at $T_{\mathrm{c}1}$, and

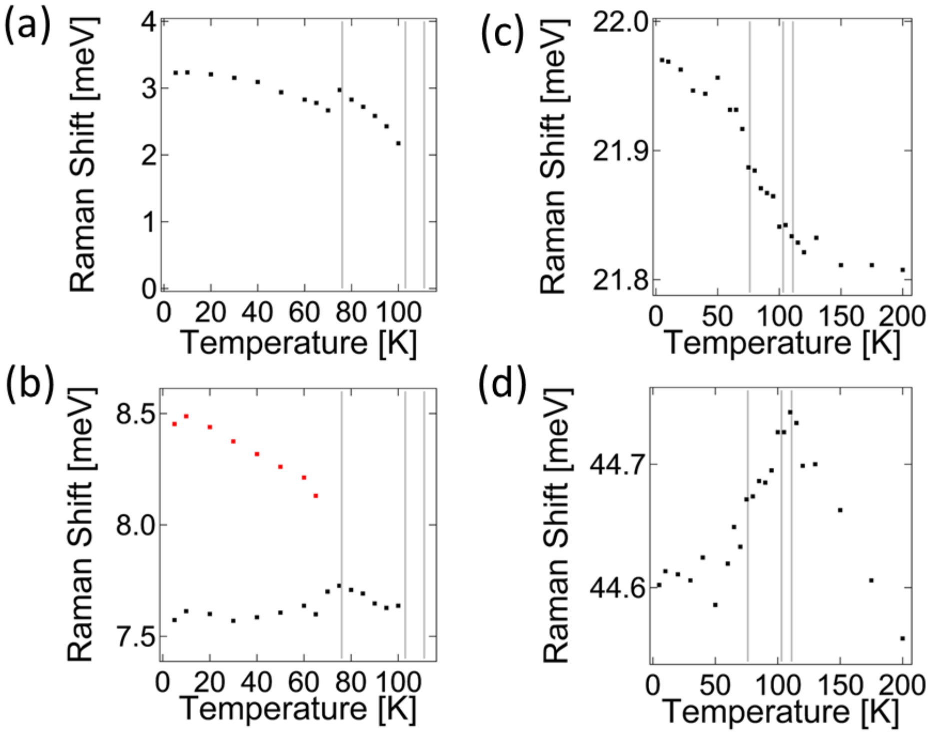

Figure 5.5: Temperature dependence of phonon energies: (a) The low-energy rotary mode; (b) The monoclinic modes near 8 meV; (c) The octahedral T_{2g} mode; (d) The octahedral A_{1g} mode. Vertical bars indicate phase transition temperatures.

it softens substantially as the temperature approaches T_{c2} from below. It is thus identified as the rotary mode previously proposed to drive the phase transition [12, 13, 15].

In the low-temperature monoclinic $P2_1/n$ phase below $T_{c1} = 76$ K (shown in black in Fig. 5.4), a distinct mode appears at 12 meV, and yet another one splits off of the phonon at 7.6 meV. The latter one again gains weight towards lower temperatures and shows significant softening towards T_{c1}, see Fig. 5.5 (b). It is worth mentioning that the low-temperature spectrum agrees with previous reports [12], with the notable exception of the aforementioned scattering continuum observed at low energies.

The temperature dependence of the energies of the octahedral T_{2g} and A_{1g} phonons, shown in Figs. 5.5 (c) and (d), respectively, reveals anomalies at

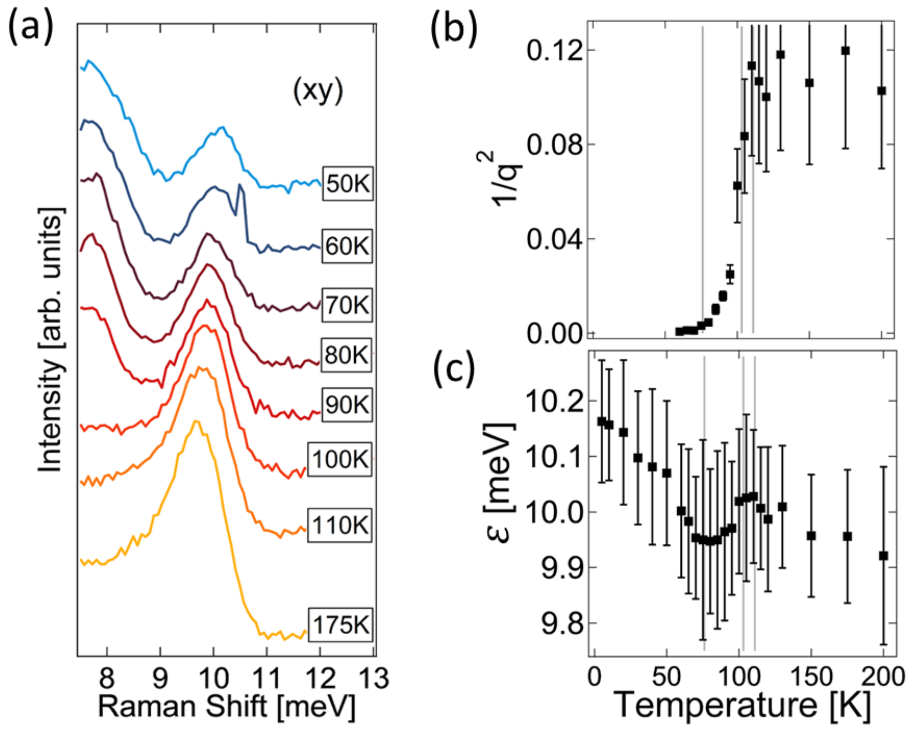

Figure 5.6: Temperature dependence of the external lattice mode: (a) Raman spectra from 50 to 175 K; (b) The coupling strength between phonon and continuum represented by $1/q^2$; (c) Reduced energy ε. Vertical bars indicate phase transition temperatures.

the phase transitions. However, a splitting of the octahedral modes is not observed (not shown), indicating the absence of a sizable deformation of the octahedra down to the lowest temperatures.

We now take a closer look at the cubic lattice mode at 10 meV which involves vibrations of the potassium ions, cf. fig. 5.6. The asymmetric line shape hints at a coupling of the mode with a continuous excitation band, and can be described by the Fano model [18],

$$I = I_0 \frac{(q+\varepsilon)^2}{1+\varepsilon^2}$$

with the Fano parameter q and the reduced energy ε. The coupling strength between the phonon and the continuum, which can be quantified by $1/q^2$, is substantial and essentially constant above T_{c2}, but drops rapidly below 100

K and vanishes below $T_{\mathrm{c1}} = 76$ K, see Fig. 5.6 (b). This is directly visible in the Raman spectra as the mode gets more and more symmetric when the temperature is lowered [Fig. 5.6 (a)]. The temperature dependence of the model parameter ε corresponding to the bare phonon energy is depicted in Fig. 5.6 (c). It shows anomalies at the same temperatures: the mode hardens down to approximately T_{c2}, then its energy decreases, before it begins to rise again below T_{c1}.

5.4 Discussion

Our main experimental results are threefold:
(i) The Raman selection rules in the high-temperature cubic phase are violated;
(ii) Below 12 meV, we observe a wide scattering continuum that shows an unusual temperature dependence and persists up to 300 K;
(iii) The vibrational mode of the cubic phase involving motions of the K^+ ions strongly couples to this continuum.
As we will discuss in the following, all three observations are consistently explained by a local breaking of the cubic symmetry due to randomly rotating $ReCl_6$ octahedra.
The cubic crystal structure in the high-temperature phase of this material, as well as many other members of the K_2PtCl_6 family, has been well established experimentally using x-ray and neutron diffraction techniques [13, 15, 25]. Anomalously high values of the atomic displacement parameters and finite librational angles of the octahedra have been reported previously for several members of this material class, including K_2ReCl_6 [26–28]. Corresponding disorder was recently found for the isostructural compounds K_2IrBr_6 and K_2IrCl_6 [27–29]. This leads us to the conclusion that the local symmetry of the octahedra deviates from the average symmetry which is retained on large length scales. The origin of this disorder may be dynamic fluctuations, static displacements, chlorine isotope disorder (natural abundance 75.8% ^{35}Cl, 24.2% ^{37}Cl), or a combination of these. Being sensitive to the local symmetry, Raman scattering will reveal such local deviations from the

global symmetry through apparently modified selection rules.

Here, it is instructive to recall a peculiarity of the crystal structure of the K_2PtCl_6 family. The lattice can be imagined to be derived from the perovskite structure ABO_3 with half of the B sites not occupied. The stability and stiffness of the perovskite structure originates to a large part from the interlocking of corner-sharing octahedra which requires any local deformation to propagate throughout the lattice, as is commonly observed in many perovskite materials [30]. However, with half of the B site ions missing in the lattice of the K_2PtCl_6 family, the octahedra disconnect and the structure loses much of its rigidity. In fact, the filled octahedra are even substantially compressed [26] and can thus be considered as only weakly interacting objects placed on the face-centered cubic positions of the antifluorite lattice. Therefore, the energy potential for rotations of the octahedra must be unusually flat and strongly anharmonic. Such an anharmonic potential shape gives rise to low-lying excitations connected to fluctuations in both the tilt angles and axes, resulting in a low-energy scattering continuum, as observed in Raman scattering.

As shown in fig. 5.4, the scattering strength of the continuum decreases continuously with increasing temperature, which is unexpected. The presence of several phonon modes overlapping with the continuum prevents a quantitative determination of the continuum spectral weight. Note that such local fluctuations of the octahedral orientation would not show up in the previously mentioned phonon density-of-states calculation [17]. We conclude that the continuum spectral weight must be determined by the density of states of the low energy excitations which itself depends on the details of the potential landscape in which they exist. This requires a detailed analysis of the potential and its temperature dependence, which is beyond the scope of this study.

A similar low-energy continuum caused by fluctuations in the octahedral orientations has recently been observed in Raman scattering of perovskite-derived metal-organic hybrid materials [31, 32]. Interestingly, the observed fluctuations have been related to structural phase transitions in the material. It is important to note that the continuum in the case of K_2ReCl_6 is at best moderately affected by the structural phase transitions. The preferred average orientation of the octahedra changes across the structural phase transitions, but the fluctuations persist in a very similar way around the new average orientation. This is consistent with previous claims that the structural phase transitions in this material class are purely displacive in nature and do not feature ordering of any kind, as an order-disorder transition would require a much higher entropy than that obtained in thermodynamic measurements [2,8]. Together with the fact that the continuum persists throughout the temperature range of our measurements, these observations indicate that the arrangement of the octahedra remains in a disordered state down to at least 5 K. This agrees with the idea of a very weak interaction between the octahedra, resulting in liquidlike properties. Future investigations of this phenomenon at the lowest experimentally accessible temperatures are highly desired.

In a recent publication [29], a similar low-energy scattering feature that also shows increasing intensity towards lower temperatures was reported for the isostructural K_2IrCl_6 and identified as a central peak. As central peaks are a byproduct of second-order structural phase transitions [33–36], this was seen as an indication for the existence of such a phase transition at very low temperatures. In our case, the continuous increase in continuum weight towards lower temperatures even across the two second-order structural phase transitions at $T_{\mathrm{c}2}$ and $T_{\mathrm{c}3}$ indicates that the continuum is unrelated to the possible spectral signatures of a central peak.

The asymmetric line shape of the cubic potassium mode at 10 meV above 76 K results from the significant coupling to the continuum. This indicates a strongly anharmonic decay of the phonon, as has previously been reported for perovskite metal-organic hybrid materials [31, 32].

Remarkably, this coupling nearly vanishes in the low-temperature monoclinic phase, while the scattering continuum persists, cf. Figs. 5.4, 5.6. As has been discovered very recently, the phase transitions at $T_{\mathrm{c}2}$ and $T_{\mathrm{c}3}$ are characterized by in-phase and out-of-phase rotations of the octahedra, respectively, while the phase transition at $T_{\mathrm{c}1}$ is accompanied by a discontinuous change in the tilt axis of the octahedra [15]. We infer that this is responsible for the

observed suppression of the coupling between the potassium phonon mode and the continuum.
Finally, we address another experimental observation which is considered to be unrelated to the main observations and their interpretation, yet worth mentioning. In contrast to previous reports that the octahedral phonon modes do not reflect the structural changes related to the crystallographic phase transitions [12, 19, 21, 24], our spectra do reveal such signatures, although comparatively moderate, see Figs. 5.5(c) and (d). The failure to detect these has previously been taken as a proof that the $ReCl_6$ octahedra remain undistorted through all of the phase transitions. We believe that this conclusion still holds, despite the weak sensitivity of the octahedral modes. In particular, we observe no indication for substantial spin-orbit related Jahn-Teller distortions of the octahedra [16], which are expected to lead to a splitting of the degenerate octahedral phonons.

Our interpretation is further supported by the observation that our three main results are also present in Raman spectra of K_2SnCl_6, see fig. 5.3. In this material, Sn has a $4d^{10}$ electronic configuration where both spin-orbital effects and Jahn-Teller interaction are absent.

5.5 Conclusion

Polarization-selective Raman spectroscopy was performed on a (001) surface of K_2ReCl_6 in the temperature range between 5 K and room temperature. We observe a violation of the selections rules in the cubic high-temperature phase, together with a low-energy scattering continuum which shows unusual temperature dependence. We propose that both observations originate from disordered local tilts and rotations of the $ReCl_6$ octahedra. Thus the cubic symmetry is broken locally but remains intact on average over large length scales. Although this global structure changes at the phase transitions, the disorder survives down to temperatures of at least 5 K due to the very weak interaction between neighboring $ReCl_6$ octahedra. The sharp signatures of the octahedral phonon modes in the Raman spectrum, the significant size of the thermal displacement ellipsoids [37], and the increase of continuum

weight for lower temperatures point to dynamic disorder as the origin of these phenomena, although a possible role of static disorder, e.g., caused by the different isotopes of Cl, cannot be fully excluded with our experimental methods. The coupling between the potassium phonon mode and the low-energy scattering continuum results in anharmonic decay and gets suppressed at the transition to the low-temperature phase at T_{c1}. The persistence of the octahedral tilting down to low temperatures could be of great relevance to the magnetic interactions in the material, especially of the kind proposed for the sister compounds K_2IrCl_6 and K_2IrBr_6 [27, 28].
Lastly, we did not detect any spectral features indicative of a sizable Jahn-Teller distortion that was suggested for this compound based on the large spin-orbit coupling in $5d$ transition materials.

Acknowledgements

The authors would like to thank A. Bertin, M. Braden, D. Khomskii, T. Lorenz, F. Parmigiani, and P. Warzanowski for inspiring discussions. Funded by the Deutsche Forschungsgemeinschaft (DFG, German Research Foundation) – Project No. 277146847 – CRC 1238.

Contributions

This project was conceived by Paul H.M. van Loosdrecht and Markus Grüninger as part of the CRC1238. Samples were grown and provided by Petra Becker and Ladislav Bohatý. Characterisation of the samples, polishing and Raman measurements were done by me. The data was analysed by me and Thomas Koethe. The manuscript was written by me, with input from Thomas Koethe, Markus Grüninger and Paul H.M. van Loosdrecht.

Bibliography

[1] P. Stein, T.C. Koethe, L. Bohatý, P. Becker, M. Grüninger, and P.H.M. van Loosdrecht, *Local symmetry breaking and low-energy continuum in* K_2ReCl_6, Phys. Rev. B **107**, 214301 (2023)

[2] R.L. Armstrong, *Structural Properties and Lattice Dynamics of 5d Transition Metal Antifluorite Crystals*, Physics Reports **57**, 343 (1980)

[3] R.H. Busey, R.B. Bevan, Jr., R.A. Gilbert, *The Heat Capacity of Potassium Hexabromorhenate(IV) from 7 to 300°K. Manifestation of Thermal History Behaviour. Antiferromagnetic Anomaly near 15°K. Entropy and Free Energy Functions*, J. Phys. Chem. **69**, 3471 (1965)

[4] A.K. Das, I.D. Brown, *A low temperature phase of* $(NH_4)_2TeBr_6$, Can. J. Chem. **47**, 4288 (1969)

[5] V. Novotny, C.A. Martin, R.L. Armstrong, P.P.M. Meincke, *Thermodynamical properties of* K_2OsCl_6 *and* K_2ReCl_6 *at low temperatures and near their structural phase transitions*, Phys. Rev. B **15**, 382 (1977)

[6] Y. Noda, T. Ishi, M. Mori, *Successive Rotational Phase Transitions in* K_2SeBr_6*. I. Structure*, J. Phys. Soc. Jpn. **48**, 1279 (1980)

[7] H. Boysen, A.W. Hewat, *A Neutron Powder Investigation of the Structural Changes in* K_2SnCl_6, Acta Cryst. B **34**, 1412 (1978)

[8] R.H. Busey, H.H. Dearman, R.B. Bevan, Jr., *The Heat Capacity of Potassium Hexachlororhenate(IV) from 7 to 320K. Anomalies near 12, 76, 103, and 111K. Entropy and Free Energy Functions. Solubility and*

Heat of Solution of K_2ReCl_6. Entropy of the Hexachlororhenate Ion, J. Phys. Chem. **66**, 82 (1962)

[9] H.W. Willemsen, C.A. Martin, P.P.M. Meincke, R.L. Armstrong, *Thermal-expansion study of the displacive phase transition in K_2ReCl_6 and K_2OsCl_6*, Phys. Rev. B **16**, 2283 (1977)

[10] R.H. Busey, E. Sonder, *Magnetic Susceptibility of Potassium Hexachlororhenate (IV) and Potassium Hexabromorhenate (IV) from 5 to 300K*, J. Chem. Phys. **36**, 93 (1962)

[11] H.G. Smith, G.E. Bacon, *Neutron-Diffraction Study of Magnetic Ordering in K_2ReCl_6*, J. Appl. Phys. **37**, 979 (1966)

[12] G.P. O'Leary, R.G. Wheeler, *Phase Transitions and Soft Librational Modes in Cubic Crystals*, Phys. Rev. B **1**, 4409 (1970)

[13] J.W. Lynn, H.H. Patterson, G. Shirane, R.G. Wheeler, *Soft Rotary Mode and Structural Phase Transitions in K_2ReCl_6*, Solid State Commun. **27**, 859 (1978)

[14] A.G. Brown, R.L. Armstrong, *Direct Measurement of an Order Parameter Associated with the 110.9-K Displacive Phase Transition in K_2ReCl_6*, Phys. Rev. B **8**, 121 (1973)

[15] A. Bertin, T. Dey, D. Brüning, D. Gorkov, K. Jenni, A. Krause, P. Becker, L. Bohaty, D. Khomskii, , V. Pomjakushin, L. Keller, M. Braden, T. Lorenz, *Interplay of magnetic order and ferroelasticity in the spin-orbit coupled antiferromagnet K_2ReCl_6*, Phys. Rev. B **109**, 094409 (2024)

[16] S.V. Streltsov, D.I. Khomskii, *Jahn-Teller Effect and Spin-Orbit Coupling: Friends or Foes?*, Phys. Rev. X **10**, 031043 (2020)

[17] D. Durocher, P. Dorain, *Phonon density of states and the vibronic spectra of impurities in K_2PtCl_6-type single crystals*, J. Chem. Phys. **61**, 1361 (1974)

[18] U. Fano, *Effects of Configuration Interaction on Intensities and Phase Shifts*, Phys. Rev. **124**, 1866 (1961)

[19] J. Winter, K. Rössler, J. Bolz, J. Pelzl, *Mössbauer Effect and Raman Studies of the Structural Phase Transitions in* $K_2[SnCl_6]$, Phys. Stat. Sol. (b) **74**, 193 (1976)

[20] J. Pelzl, P. Engels, R. Florian, *Raman Spectroscopic Study of the Structural Phase Transitions in* K_2SnCl_6, Phys. Stat. Sol. (b) **82**, 145 (1977)

[21] R.W. Berg, F.W. Poulsen, N.J. Bjerrum, *Low temperature vibrational spectroscopy. I. Hexachlorotellurates*, J. Chem. Phys. **67**, 1829 (1977)

[22] B.I. Swanson, *Displacive Phase Transitions in* K_2SnBr_6, Phys. Stat. Sol. (a) **47**, K95 (1978)

[23] S.L. Chodos, R.W. Berg, *Low temperature vibrational spectra, lattice dynamics, and phase transitions in some potassium hexahalometallates:* $K_2[XY_6]$ *with X=Sn or Te and Y=Cl or Br*, J. Chem. Phys. **70**, 4864 (1979)

[24] K. Negita, N. Nakamura, H. Chihara, *Study of Structural Phase Transitions in* $(NH_4)_2SnBr_6$ *by Raman Scattering*, Solid State Commun. **34**, 949 (1980)

[25] B. Aminoff, *Über die Kristallstruktur von* K_2ReCl_6, Z. Krist. **94**, 246 (1936)

[26] H.D. Grundy, I.D. Brown, *A Refinement of the Crystal Structures of* K_2ReCl_6*,* K_2ReBr_6 *and* K_2PtBr_6, Can. J. Chem. **48**, 1151 (1970)

[27] N. Khan, D. Prishchenko, Y. Skourski, V.G. Mazurenko, A.A. Tsirlin, *Cubic symmetry and magnetic frustration on the fcc spin lattice in* K_2IrCl_6, Phys. Rev. B **99**, 144425 (2019)

[28] N. Khan, D. Prishchenko, M.H. Upton, V.G. Mazurenko, A.A. Tsirlin, *Towards cubic symmetry for* Ir^{4+}*: Structure and magnetism of the antifluorite* K_2IrBr_6, Phys. Rev. B **103**, 125158 (2021)

[29] S. Lee, B.H. Kim, M.-J. Seong, K.-Y. Choi, *Noncubic local distortions and spin-orbit excitons in* K_2IrCl_6, Phys. Rev. B **105**, 184433 (2022)

[30] A. M. Glazer, *The Classification of Tilted Octahedra in Perovskites*, Acta Cryst. B **28**, 3384 (1972)

[31] M. Menahem, Z. Dai, S. Aharon, R. Sharma, M. Asher, Y. Diskin-Posner, R. Korobko, A.M. Rappe, O. Yaffe, *Strongly Anharmonic Octahedral Tilting in Two-Dimensional Hybrid Halide Perovskites*, ACS Nano **15**, 10153 (2021)

[32] R. Sharma, Z. Dai, L. Gao, T.M. Brenner, L. Yadgarov, J. Zhang, Y. Rakita, R. Korobko, A.M. Rappe, O. Yaffe, *Elucidating the atomistic origin of anharmonicity in tetragonal* $CH_3NH_3PbI_3$ *with Raman scattering*, Phys. Rev. Materials **4**, 092401(R) (2020)

[33] A. Kania, K. Roleder, G.E. Kugel, M.D. Fontana, *Raman scattering, central peak and phase transitions in* $AgNbO_3$, J. Phys. C: Solid State Phys. **19**, 9 (1986)

[34] B.E. Vugmeister, Y. Yacoby, J. Toulouse, H. Rabitz, *Second-order central peak in the Raman spectra of disordered ferroelectrics*, Phys. Rev. B **59**, 8602 (1999)

[35] A.G. Kuznetsov, V.K. Malinovski, N.V. Surovtsev, *Specific features in the behaviour of the central peak in Raman spectra of lithium tantalate*, Phys. Solid State **48**, 2317 (2006)

[36] V.S. Gorelik, T.G. Golovina, A.F. Konstantinova, *Central Peak in the Raman Spectra of Quartz Crystals in a Wide Temperature Range*, Crystallography Rep. **65**, 605 (2020)

[37] A. Bertin, M. Braden, Private communication (2022)

CHAPTER 6

Raman Scattering on Phonons and Electronic States in Ruthenium Dimers

6.1 Cluster Mott insulators

Mott insulators are materials that are electrically insulating although conventional band theory predicts that they should be conductive. This generally happens in cases where electron-electron interaction is strong enough to prevent charge transfer between neighbouring ions. Mott insulators are most easily described by the Mott-Hubbard model [1–3], which introduces the on-site Coulomb repulsion parameter U between electrons occupying the same site and the hopping parameter t, which is the energy required for an electron to hop to an adjacent site. If U > t, the material is insulating. Changes in the charge carrier density, e.g. through doping, can cause a phase transition between conducting and Mott insulating state, which is called a Mott transition.

In some materials, metal ions and their surrounding ligands may form structural clusters of two or more sites. In this case, the hopping parameter is different for electron transfer between ions within the same cluster (*intra-cluster hopping*, t_{intra}) on the one side, and transfer to another cluster (*inter-cluster hopping*, t_{inter}) on the other side. If both hopping parameters are small compared to U, the material is still a Mott insulator. Materials with $t_{inter} < U$, but $t_{intra} >> U$ are called *cluster Mott insulators.* Hopping between clusters is strongly suppressed, but within any given cluster, the energy required for an electron to transfer to a different site is very low. In the limiting case, it can even be assumed that $\frac{t_{intra}}{U}$ is infinite, and thus the electrons are completely delocalised over the entire cluster. The materials discussed in this chapter house clusters consisting of two transition metal ions (*dimers*), but compounds with larger clusters, like *trimers, tetramers,* and so on, exist as well.

Cluster Mott insulating states are well known to occur in 5d transition metal compounds, chiefly those with IrO_6 octahedra, like $Ba_3CeIr_2O_9$ [4], $Ba_3InIr_2O_9$ [5], $Ba_3Ti_{3-x}Ir_xO_9$ [6] (all dimers), and the trimer compound $Ba_4NbIr_3O_9$ [7], but also Ta-based systems, e.g. $GaTa_4Se_8$ [8]. The situation is different for 3d transition metals, as in most of these compounds, the picture of localised single-site moments is more appropriate. The different behaviour of 3d and 5d compounds in this regard originates in the larger values of U for 3d transition metals [9], as well as the larger spatial extent of the 5d orbitals. For 4d elements, the situation is as-of-yet unclear, although there are reports on successful observation of 4d cluster-Mott systems based on Molybdenum [10, 11] and Niobium [11].

This chapter presents Raman spectroscopic measurements of electronic transitions in two ruthenium-based dimer systems: $Ba_3CeRu_2O_9$ and $Ba_3EuRu_2O_9$. Single crystals were grown by H. Schilling and P. Becker at the University of Cologne. They crystallise in the hexagonal space group $P6_3/mmc$ [12–14]. A schematic picture of the crystal structure, as well as pictures of the two samples used for the measurements in this chapter, can be seen in fig. 6.1. The RuO_6 octahedra form face-sharing dimers along the c axis with the Ba and Ce ions providing the trigonal structure that hosts them. The Ru-Ru distance of ≈ 2.5 Å [12,14] is smaller than e.g. in bulk ruthenium (2.7 Å) [15]. This has been suggested [5] to facilitate the formation of quasi-molecular orbitals. The ions occupy the Wyckoff positions 2a (Ce), 2b (Ba1), 4f (Ba2 & Ru), 6h (O1) and 12k (O2). The samples also macroscopically grow in a near-hexagonal shape, with diameters of around 350 μm ($Ba_3CeRu_2O_9$) and 250 μm ($Ba_3EuRu_2O_9$). The surfaces are flat, with small crystallites growing

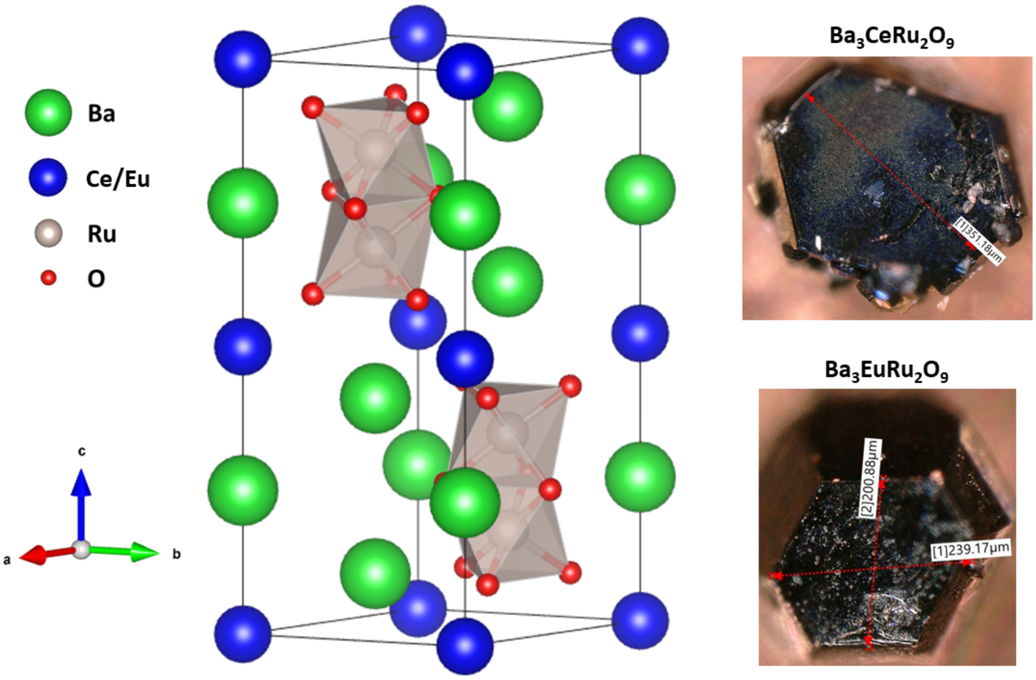

Figure 6.1: Left: Crystal Structure of $Ba_3CeRu_2O_9$ and $Ba_3EuRu_2O_9$. Green, blue, grey and red spheres represent barium, cerium/europium, ruthenium and oxygen ions, respectively. Right: Pictures of the measured (001) surfaces of $Ba_3CeRu_2O_9$ (top) and $Ba_3EuRu_2O_9$ (bottom). Arrows and labels indicate measured distances on the sample surface.

in some places and large, homogeneous areas in between.

6.2 Phonon spectra

The irreducible representation of Raman active phonons is Γ_{Raman} = 5 A_{1g} + 8 E_{2g} + 6 E_{1g} [16]. The corresponding Raman tensors are

$$A_{1g} = \begin{pmatrix} a & 0 & 0 \\ 0 & a & 0 \\ 0 & 0 & b \end{pmatrix} \tag{6.1}$$

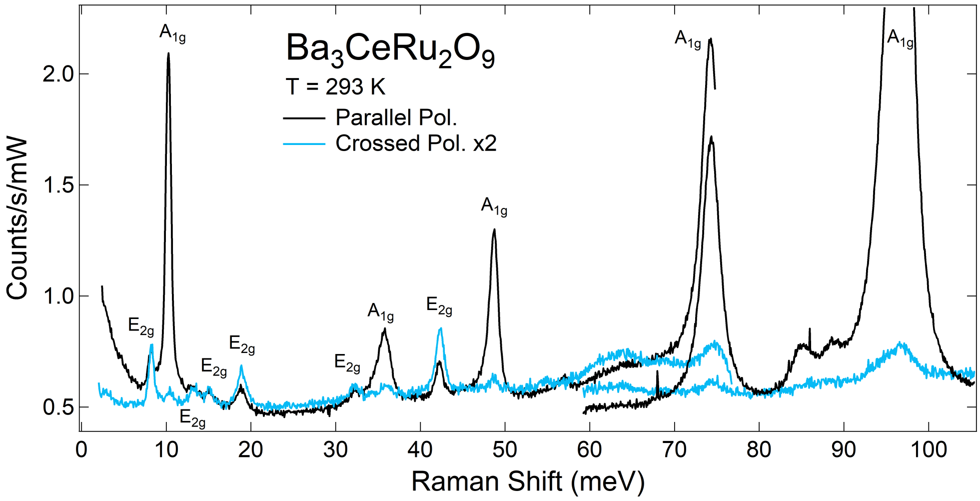

Figure 6.2: Raman spectra of $Ba_3CeRu_2O_9$ at T = 5 K in parallel (black) and crossed (blue) polarisation, measured in two separate energy windows. Labels indicate the phonon representation. The spectrum in crossed polarisation is multiplied with a factor 2 for better comparability.

$$E_{1g} = \begin{pmatrix} 0 & 0 & 0 \\ 0 & 0 & c \\ 0 & c & 0 \end{pmatrix}, \begin{pmatrix} 0 & 0 & -c \\ 0 & 0 & 0 \\ -c & 0 & 0 \end{pmatrix} \tag{6.2}$$

$$E_{2g} = \begin{pmatrix} d & 0 & 0 \\ 0 & -d & 0 \\ 0 & 0 & 0 \end{pmatrix}, \begin{pmatrix} 0 & -d & 0 \\ -d & 0 & 0 \\ 0 & 0 & 0 \end{pmatrix} \tag{6.3}$$

Raman measurements were done in $c(aa)\bar{c}$ (*"parallel"*) and $c(ab)\bar{c}$ (*"crossed"*) polarisation geometries on a (001) surface. From the tensors, the A_{1g} phonons should be active in parallel polarisation only, the E_{2g} phonons should be active in both geometries with equal magnitude, and the E_{1g} phonons should be completely inactive.

Fig. 6.2 shows the Raman spectra of $Ba_3CeRu_2O_9$ at room temperature, measured with the Jobin Yvon spectrometer. The five A_{1g} phonons yield the most intense peaks in the parallel polarisation spectrum at 10, 36, 49, 74 and 96 meV. As expected, they are not visible in the crossed polarisation spectrum. The energies of the four lowest ones correspond very well to those

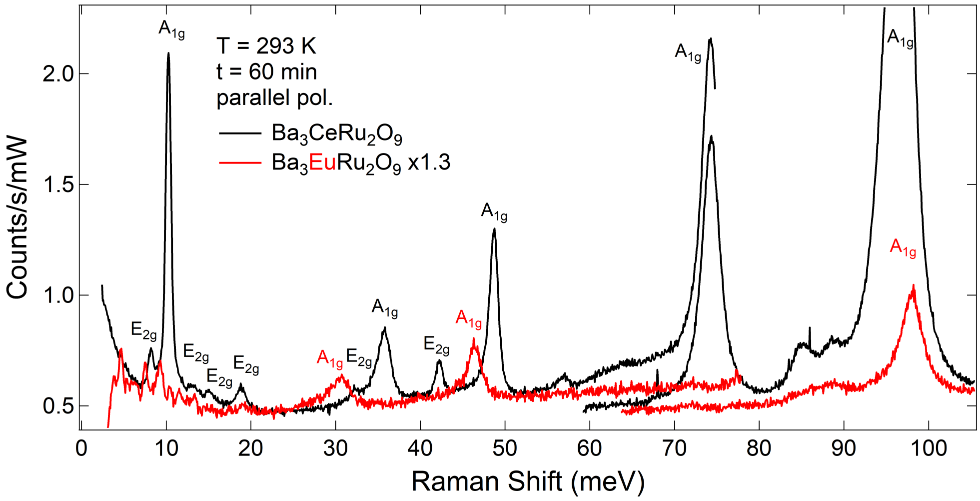

Figure 6.3: Raman spectra of $Ba_3CeRu_2O_9$ (black) and $Ba_3EuRu_2O_9$ (red) at T = 293 K in parallel polarisation, measured in two separate energy windows. The BERO spectrum has been multiplied by 1.3 for better comparison. Black/red labels indicate phonon types for the $Ba_3CeRu_2O_9$ and $Ba_3EuRu_2O_9$ spectrum, respectively.

of A_{1g} modes reported in the parent compound Ca_2RuO_4 [17–21], and all 5 A_{1g} modes are similar to those reported for isostructural $Ba_3ZnSb_2O_9$ [22]. The E_{2g} phonon peaks are generally a bit weaker, but six of them can be tentatively identified at 8, 14, 15, 19, 32 and 42 meV. The magnon- and two-magnon peaks that have been seen in Ca_2RuO_4 at low temperatures [17–19, 21] don't show up here, because of the absence of magnetic order. Additional peaks in the spectrum at 85 and 89 meV can be attributed to two-phonon scattering processes. The feature around 65 meV will be addressed together with the higher energy excitations in chapter 6.4.3.

The Raman spectrum of $Ba_3EuRu_2O_9$ is plotted in fig. 6.3. Since the crystals are very small, this sample had to be measured in a slightly different setup, using a microscope to focus the light. This results in a visible signature of the Raman spectrum of air in the energy region below 12 meV. The spectrum features only three recognisable phonons, all of A_{1g} symmetry, at energies 31, 46 and 98 meV, all of them slightly shifted with respect to their counterparts in $Ba_3CeRu_2O_9$, and with ≈ 5 times lower intensity.

Interestingly enough, the 10 meV and 75 meV peaks that are reported in most RuO_6-based compounds [17–23] are completely absent here. There are also no detectable signatures of any of the E_{2g} modes. This is confirmed by a cross-polarised measurement on $Ba_3EuRu_2O_9$, in which, according to the selection rules, only the E_{2g} modes are allowed. The corresponding spectrum does not show any recognisable features within 60 minutes of integration time, apart from the previously mentioned peaks below 12 meV originating from air.

6.3 Electronic structure

When searching for eletronic transitions, the starting point has to be the electronic configuration of the magnetic ions. In both $Ba_3CeRu_2O_9$ and $Ba_3EuRu_2O_9$, the oxidation states of the barium and oxygen ions are 2+ and 2-, respectively. Cerium has an electronic configuration of $[Xe]6s^25d^14f^1$, where the 6s, 5d and 4f orbitals are very close in energy, and one electron occupies the d shell because of the strong electron-electron repulsion within the 4f orbital [24]. Like all lanthanides, cerium ions can take the 3+ oxidation state resulting in a $[Xe]4f^1$ configuration. It is unique among this group in that it can also exist in a 4+ oxidation state [24], resulting in a noble gas configuration. This is the case e.g. in the popular polishing agent CeO_2 [25]. For $Ba_3CeRu_2O_9$, this means that the valence of ruthenium must be 4+ as well, resulting in a $4d^4$ configuration.
In the case of europium, things are more complicated. The configuration of elemental europium is $[Xe]4f^76s^2$. Besides taking the typical 3+ state with configuration $[Xe]4f^6$, it can also form divalent compounds like EuO, Eu_2SiO_4 or $EuTiO_3$ [26], where the oxidation state of Eu is 2+. This is because the resulting $4f^7$ configuration with an exactly half-filled 4f shell provides additional stability [24]. In $Ba_3EuRu_2O_9$, the 3+ state is favoured, which results in a mixed 4+/5+ valence for ruthenium, and accordingly a mixed electronic configuration $5d^3$ / $5d^4$.
As illustrated in chapter 2.5, the 4d orbitals can be described by the cubic harmonics. Their degeneracy is lifted by the octahedral crystal field, which

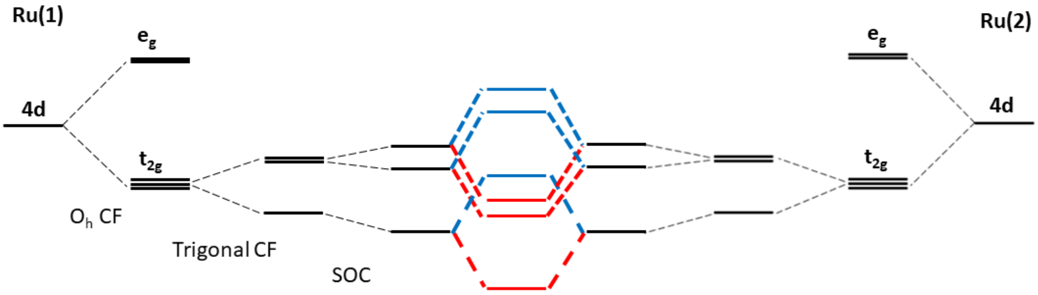

Figure 6.4: Electronic Structure of ruthenium dimers. Left and right side show the 4d states of the free Ru ion, which are split by the presence of octahedral (O_h) and trigonal crystal field, and spin-orbit coupling. The center shows the formation of quasimolecular bonding (red) and anti-bonding (blue) states.

splits them into a lower energy t_{2g} triplet and a higher energy e_g doublet. These states are further influenced by the trigonal crystal field that is provided by the barium and cerium ions, and by spin-orbit coupling, which cause the t_{2g} orbital to split into three non-degenerate states. This is illustrated in the left- and right side part of fig. 6.4. If the intra-cluster hopping is large enough and the d-electrons are completely delocalised over a dimer, the single-site orbitals of the two ruthenium ions can combine and form *quasi-molecular* cluster orbitals [4, 14, 27]. This process, thought to be similar to the formation of molecular orbitals in e.g. H_2, leads to the creating of bonding- and anti-bonding states. This is depicted in the central part of fig. 6.4. RIXS measurements on dimer [4] and trimer [7] systems show a number of peaks that can be interpreted as crystal field transitions. Exciting these at different points in reciprocal space reveals a periodic intensity modulation reminiscent of Young's double slit experiment that has been established as a signature of quasi-molecular states. As a counter-example, the same measurement on Ba_2CeIrO_6, which is a Mott insulator without clusters, shows the single-ion electronic states, and no periodic modulation [28]. In the two compounds discussed in this chapter, the short Ru-Ru distance and preliminary RIXS results [29] suggest that the formation of dimers is indeed a relevant process in the system. Magnetic susceptibility measurements [14] also concluded that the magnetic ground state can't be properly described in a single-ion picture, and that the assumption of a dimer ground state in a molecular orbital picture is required.

Properly taking into account all interactions in the system that can change the electronic states, including especially the influence of intra-cluster hopping, leads to a significant increase in the number of excited states expected. Since the energy differences between these states are typically very small, Raman spectroscopy should be a good way to resolve them.

6.4 High energy Raman measurements

Raman spectroscopic measurements on the $Ba_3CeRu_2O_9$ and $Ba_3EuRu_2O_9$ samples shown above were done with the Princeton HRS-300 spectrometer at $T = 5$ K and 293 K in *parallel* and *crossed* polarisation geometries. Since the focus is on excitations in the energy range between 150 and 800 meV, a green laser with a wavelength of 532 nm was used to ensure optimised detection efficiency. The power density was ≈ 250 W/cm^2 for the measurements on $Ba_3CeRu_2O_9$ and 100 W/cm^2 for the measurements on $Ba_3EuRu_2O_9$, with a spot size of ≈ 10 μm.

The spectrum of $Ba_3EuRu_2O_9$ recorded at $T = 5$ K is displayed in fig. 6.5 for parallel (black curve) and crossed (blue curve) polarisations. The two strongest phonons at 45 meV and 96 meV known from the measurements with the Jobin Yvon spectrometer shown in fig. 6.3 can be seen in the energy region below 100 meV that is marked in grey. Their strong polarisation dependence confirms that these are the high-intensity A_{1g} phonons. The lowest energy excitation that was not seen in the phonon spectrum is a single peak at 181 meV. Since this is approximately twice the energy of the strongest phonon, it is tempting to identify it as a two-phonon excitation. However, such an excitation would typically be expected to be much weaker in comparison to the one-phonon peak. A similar peak has been reported in Raman measurements of the parent compound Ca_2RuO_4 [20,21] at a slightly lower energy of 168 meV. Contrary to the phonons, this peak also doesn't disappear in a crossed polarisation measurement. All peaks above 100 meV can be tentatively identified as crystal field excitations. They can be sepa-

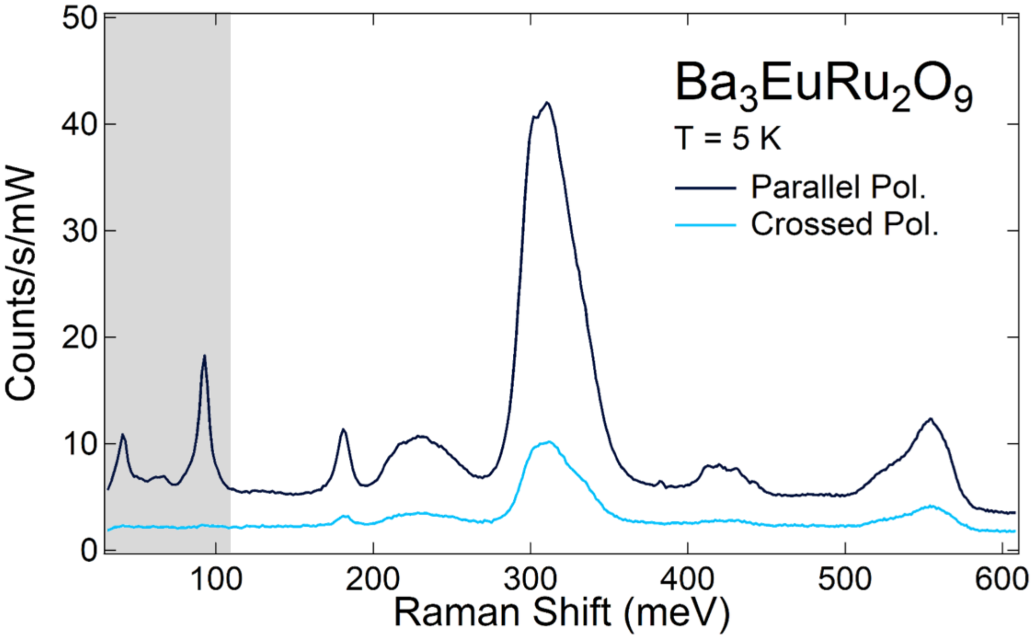

Figure 6.5: High energy Raman spectra of $Ba_3EuRu_2O_9$ measured at T = 5 K in parallel (black) and crossed (blue) polarisation. The grey area marks the phononic energy range that was covered with the Jobin Yvon spectrometer.

rated into four "groups" around 220 meV, 310 meV, 420 meV and 550 meV that each consist of multiple excitations. A multi-peak fit of the spectrum in parallel polarisation can be found in the appendix. It shows that the highest intensity peak groups at 310 meV can be fitted with three peaks, while the other three peak groups only require two. It should be noted that the width of the fitted peaks is typically between 10 and 20 meV, which is significantly higher than the calculated spectral resolution of 2-3 meV. This can also be seen when comparing the crystal field excitations with the phonon peak at 90 meV, which is narrower ($\approx$ 7 meV, with a calculated spectral resolution of 4 meV at that energy). The spectrum measured in crossed polarisation shows the same features, with the intensity reduced by a factor 3 - 4. This applies to all crystal field excitations, and also to the feature at 181 meV, further discouraging an explanation based on two-phonon scattering. The reduced intensity can at least partially be traced back to the transmission of the beam splitter, which is $\approx$ 1.6 times higher for the scattered light com-

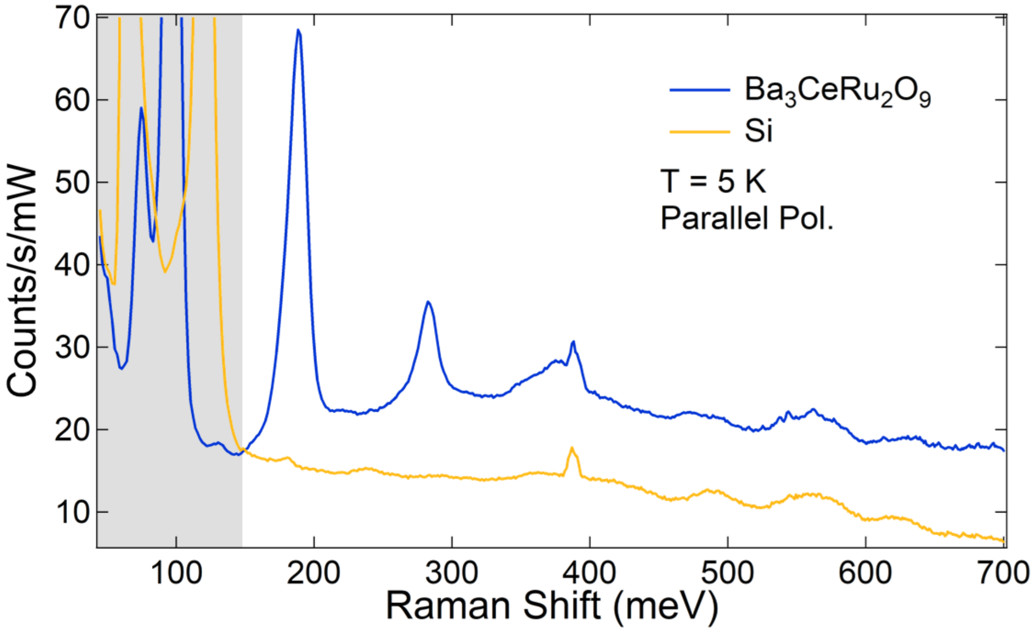

Figure 6.6: Raman spectrum of $Ba_3CeRu_2O_9$ measured with the Princeton setup at T = 5 K (blue curve), and of Silicon (001) (yellow curve). The grey area shows the phononic energy range.

ponent parallel to the incident light. Above 600 meV, the spectra show no discernible features.

The low temperature Raman spectrum of $Ba_3CeRu_2O_9$ can be seen in fig. 6.6 (blue curve). Again, the spectral region below 100 meV shows the strongest phonon peaks known from the previous sub-chapter, in this case at 74 and 96 meV. The phonons in $Ba_3CeRu_2O_9$ have an almost 10 times higher count rate than those in $Ba_3EuRu_2O_9$, which is also reminiscent of the previous measurement. Like $Ba_3EuRu_2O_9$, this sample shows a peak at $\approx$ 180 meV. This is no surprise if indeed it is the same peak that was observed in the parent compound Ca_2RuO_4. At higher energies, a multitude of further peaks are recognisable. However, not all of them seem to be excitations of $Ba_3CeRu_2O_9$. The yellow curve in fig. 6.6 shows a Raman spectrum of Silicon, measured under the same conditions as $Ba_3CeRu_2O_9$. Since Silicon has no excitations in the covered energy range except for one phonon at 65 meV and its multi-phonon equivalents, the spectrum should be completely flat above 150 meV in an ideal measurement. However, some of the features seen in the spectrum of $Ba_3CeRu_2O_9$ can also be seen here, indicating that these are likely artefacts from other sources, like the spectrometer, laser or external light. Comparing these, only the four peaks at 282 meV, 360 meV, 379 meV and 471 meV can be safely identified as crystal field excitations of $Ba_3CeRu_2O_9$. The crossed polarisation spectrum can be found in the appendix and is very comparable to that of $Ba_3EuRu_2O_9$. Most of the excitations seen in fig. 6.6 are active here as well, albeit with much lower intensity, and no new peaks arise. The signatures that were attributed to external sources do not show polarisation dependence.

6.4.1 Temperature dependence

Fig. 6.7 shows the temperature dependence for the high energy Raman spectrum of both compounds. There are no crystallographic phase transitions and no magnetic ordering expected for this material class [12,13]. Indeed, the spectra show the same peaks for both T = 5 K and room temperature. For $Ba_3CeRu_2O_9$, there are no discernible energy shifts or intensity differences over the entire spectral range. The only exceptions are the weak feature at 120 meV, which disappears at room temperature, and the sharp feature at 390 meV, which can be attributed to instrumental response (see previous section). The phonon at 92 meV is cut off for T = 293 K due to saturation of the CCD camera.

For $Ba_3EuRu_2O_9$, the crystal field excitations also don't show any changes with temperature. Notably, the phonons are ≈ 5 times stronger than at low temperature. The 181 meV peak was, as mentioned before, seen in Ca_2RuO_4 [20, 21], where it was reported to disappear for $T > 200$ K. Since this corresponds to the temperature of orbital ordering in that compound, the excitation was interpreted as an *orbiton*, similar to the one observed in $LaMnO_4$ [30], but this interpretation is still under debate today. Since there is no orbital ordering expected in $Ba_3EuRu_2O_9$, and the peak is not influenced by temperature changes at all, such an interpretation for this measurement

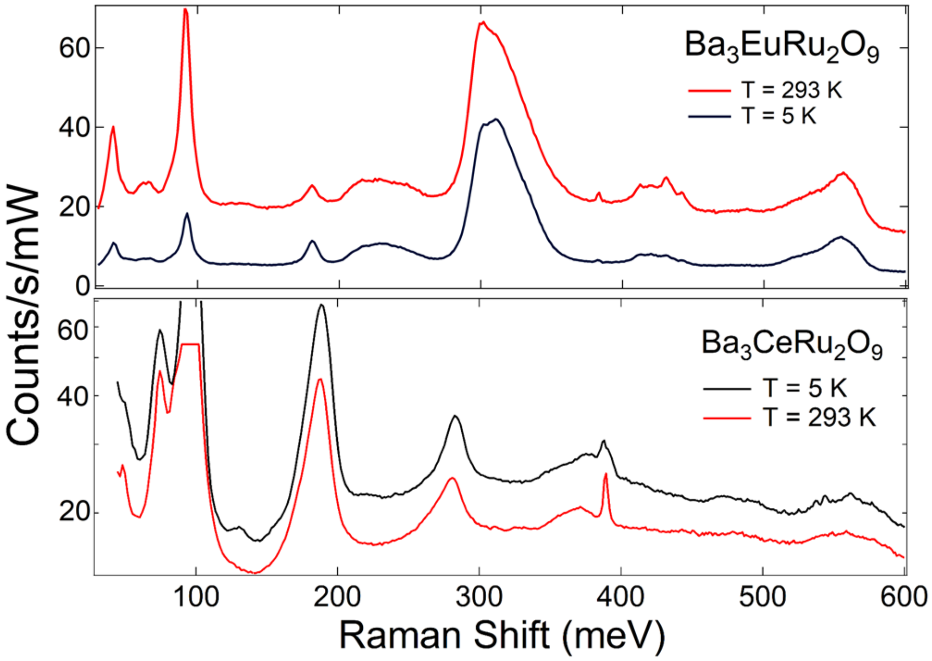

Figure 6.7: Temperature dependence of the high energy Raman spectrum for $Ba_3EuRu_2O_9$ (top panel) and $Ba_3CeRu_2O_9$ (bottom panel, logarithmic scale) in parallel polarisation.

is unlikely.

6.4.2 Influence of f-levels

As discussed in section 6.3, the lanthanides cerium and europium have partially filled f orbitals. For both of them, the electronic configuration, and thus the transitions, depend strongly on the valence. If, as assumed, the oxidation state of cerium is 4+, this would leave it with the closed shell configuration of Xenon, and no transitions would be possible. If, on the other hand, the oxidation state is 3+, and accordingly the electronic configuration is [Xe]4f^1, the ground state splits into a lower energy $^2F_{5/2}$ and a higher energy $^2F_{7/2}$ state. The transition between these is forbidden for free Ce^{3+} according to the Laporte selection rule, but can become symmetry-allowed in a crystal environment [32]. Its energy gap has been reported as 273 meV [32] or 281 meV [33], depending on the lattice symmetry. This is well in line with the strong peak in the Raman spectrum at $\approx$ 280 meV. Although the 4+ valence of cerium for this sample has been confirmed experimentally, the presence of oxygen vacancies, which are thought to be the most common defect in this structure, could indeed locally alter the valence of the cerium ions to Ce^{3+}. Eu^{3+} with configuration [Xe]$4\mathrm{f}^6$ has a $^7F_0$ ground state, and 6 low-lying excited states ^7F_J, J = 1,...,6 in the energy range up to 650 meV [32, 34, 35]. In a crystal field, these may further split into a multitude of possible excited states, although it should be noted that the influence of crystal fields on f orbitals is much less significant than for d orbitals [24]. The lowest of these states have energies of only around 45 - 50 meV [32, 34], which puts them in the phononic energy range. However, the spectrum in fig. 6.3 shows no peaks at this energy that can't be identified as phonons, making it unlikely that there are indeed crystal field transitions in this range. Comparing the calculated values for Eu^{3+} f transitions to the peaks in the Raman spectrum in fig. 6.5 (see Appendix) yields no obvious agreement. Only the $^7F_0 \rightarrow {}^7F_3$ transitions around 250 meV and the group of Raman peaks around 200-280 meV roughly coincide. Another interesting transition to look at is that from the lowest lying excited state $^7F_1$ to the $^5D_1$ state. This transition has an energy of 2.339 eV, which is remarkably close to the excitation energy of the laser used for the measurements presented here (2.331 eV). The low energy of the $^7F_1$ state (45 meV) should allow it to be weakly thermally populated at room temperature, which could potentially lead to resonance effects. If this was the case, there should be a large difference between the room temperature spectrum and that at low temperature, where the $^7F_1$ state is depopulated. As discussed above, at room temperature, the scattering intensity of the phonons is $\approx$ 5 times stronger than at 5 K, while the crystal field transitions do not change. However, without a more detailed temperature dependence or measurements with different incident wavelengths, it is difficult to conclusively argue that resonance plays a big role in the material. So in total, it is likely that there is little to no influence of the Eu^{3+} crystal field transitions on the spectra presented in this chapter.

6.4.3 Identification of ruthenium d → d transitions

The remaining peaks in the spectrum can thus be identified as transition between the electronic states of the ruthenium ion, split by spin-orbit coupling and intra-cluster hopping. The multitude of interactions in the dimers leads to an enormously high number of electronic states that can be scattered from [29]. This be shown in the following through comparison of the Raman data to RIXS measurements and calculations.

Fig. 6.11 shows a comparison of the Raman data with measurement data from resonant inelastic x-ray scattering (RIXS) experiments [29]. The RIXS spectrum can be divided into three energy regions: Below 0.4 eV; between 0.4 and 1.4 eV; and above 1.4 eV. The Raman data only covers the first region and a small part of the second. The phonons and the lowest crystal field excitations from the Raman spectrum lie within in the first section of the RIXS spectrum, indicating that these signatures have a similar origin. In

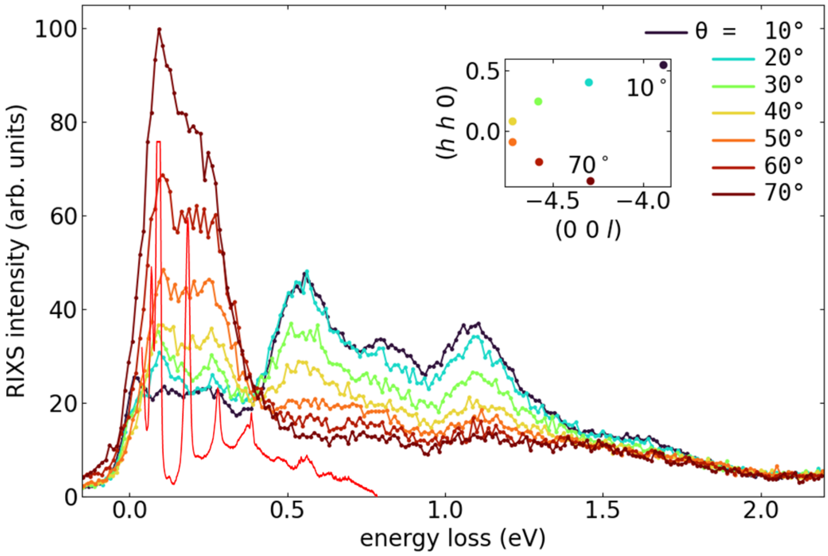

Figure 6.8: RIXS spectra of $Ba_3CeRu_2O_9$ measured for different scattering angles at T = 20 K. The lower, red line is the parallel polarisation Raman spectrum at T = 5 K. The intensity of the Raman spectrum is arbitrarily scaled for best comparison. Inset: The scattering angles Θ can be translated into points in k-space.

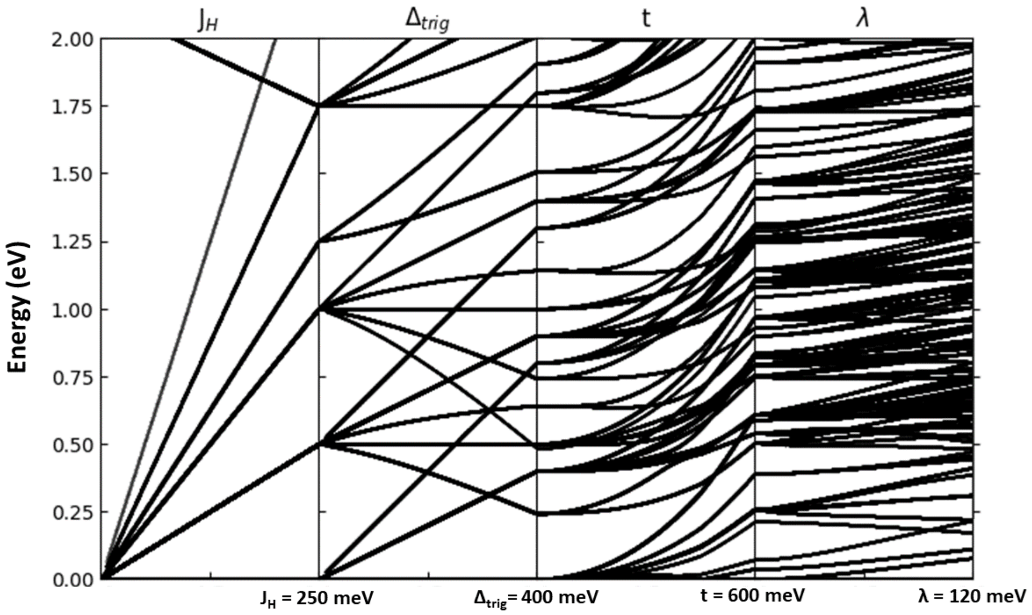

Figure 6.9: Calculation of energy states for a four-hole dimer, considering Hund's coupling J_H, trigonal crystal field Δ_{trig}, intra-cluster hopping t, and spin-orbit coupling λ.

the energy region above 400 meV, RIXS shows another group of excitations, while in the Raman spectrum, only very weak signatures are recognisable. An interesting observation is that the highest energy Raman active excitations lie exactly in the intensity minimum of the RIXS graph between the first and second group of excitations. The same thing can also be observed when comparing the $Ba_3EuRu_2O_9$ spectra (see fig. 6.11 in the appendix): Even though the energy scale of excitations in that material is different, the highest energy Raman peaks are again in the minimum of the RIXS curve. This could be an indicator that these peaks belong to excitations that the RIXS incident energy is not resonant with.

Fig. 6.9 shows a calculation of t_{2g} energy states for two-site system with four holes, i.e., a cluster consisting of two Ru^{4+} ions with eight electrons occupying the t_{2g} orbitals. This corresponds to the electronic configuration of $Ba_3CeRu_2O_9$. The model considers on-site Coulomb repulsion, Hund's coupling, trigonal crystal field, spin-orbit coupling and intra-cluster hopping, parametrised by the corresponding parameters U, J_H, Δ_{trig}, λ and t. Starting values were taken from comparable cluster systems, and the parameters were optimised for best agreement with the measured RIXS spectra. The best set of parameter values was found to be

$$\begin{aligned} U &= 2.5\ \text{eV} \\ J_H &= 250\ \text{meV} \\ \Delta &= 400\ \text{meV} \\ \lambda &= 120\ \text{meV} \\ t &= 600\ \text{meV} \end{aligned}$$

In each section of the plot, the parameter mentioned on top is increased from 0 to this optimised value, with the final set of states emerging on the very right side. It should be noted that transitions to these states are not necessarily Raman active. For example, all excitations to the second branch emerging from finite Hund's coupling change the spin multiplicity, and are thus Raman-forbidden.

The simulation coincides quite well with the measured spectrum for BCRO. The lowest branch at around 80 meV could potentially be responsible for the unidentified peak in the phonon region around 65 meV (fig. 6.2). The isolated Raman peak at 180 meV fits nicely to the isolated branch in the calculation, and the double peak at 360 and 380 meV corresponds well to the two calculated states at exactly that energy. For higher energies, the extremely high density of energy levels makes an exact identification impossible. An overview of the detected peaks and their tentative interpretation can be found in table 6.1 for $Ba_3CeRu_2O_9$. For $Ba_3EuRu_2O_9$, no calculations of electronic states exist yet. The peaks found in its Raman spectrum are listed in table 6.2.

An additional benefit of Raman spectroscopy that can yield information about the relative strengths of interactions in the system is the possibility to filter different polarisations of the scattered light. For a purely cubic crystal field with no additional interactions, a strong polarisation dependence with

	Energy (meV)	**Interpretation**
1	181	Suggested: Orbiton, 2-Phonon, CF, corresponds to branch in calculations
2	282	Potentially Ce^{3+}: $J_{eff} = 1/2 \rightarrow 3/2$, but also coincides with calculated energy level
3	360	CF doublet, not present in RIXS, coincides well with calculated energy levels
4	379	
5	471	CF

Table 6.1: Energies (T = 5 K) of crystal field excitations and their interpretation in the Raman spectrum of $Ba_3CeRu_2O_9$.

peaks mostly appearing either in parallel or crossed polarisation measurements would be expected. As discussed in chapter 2.5, a trigonal crystal field will a leakage of the formerly cross polarised excitations to the parallel polarisation geometry. The additional presence of SOC causes further weakening of the selection rules, but will also, if dominant, create additional transitions of predominantly T_{2g} character. RIXS results and simulations, as shown above, suggest that both interactions are present, but that $\frac{\Delta_{trig}}{\lambda} \approx 4$. The completely lack of polarisation contrast and the high number of observable states for both $Ba_3EuRu_2O_9$ and $Ba_3CeRu_2O_9$ can thus be seen as further indication that a single-site picture is not sufficient to describe the excitation spectrum. The inclusion of intra-cluster hopping leads to an enormous increase in the number of energy states that can be scattered from. In fact, the emerging states are so density packed in most energy regions that a proper separation likely becomes impossible even with high resolution techniques like Raman scattering. If the spectral signatures observed are indeed mixtures of many different states with different polarisation dependence, it is conceivable that for their combined spectral signature, the polarisation dependence is on average the same in the entire covered energy range.

	Energy (meV)	Interpretation
1	181	Suggested: Orbiton, 2-Phonon, CF same energy as peak 1 in BCRO
2	216	CF doublet
3	236	
4	300	CF triplet, strongest peaks in the spectrum, energies corresponds roughly to intensity maximum in RIXS spectra
5	313	
6	318	
7	414	CF doublet
8	429	
9	533	CF doublet, not present in RIXS, similar to peak 5 & 6 in BCRO
10	557	

Table 6.2: Energies (T = 5 K) of high energy excitations in $Ba_3EuRu_2O_9$ and their suggested interpretation.

6.5 Conclusion

The successful construction of a new Raman setup centred around a single grating with low groove density now enables measurements in the energy range up to ≈ 1 eV. Ruthenium dimer systems provide an optimal opportunity for a first study, as they are interesting, yet mostly unexplored, and the strengths of the setup can play out nicely.

The dimer materials $Ba_3CeRu_2O_9$ and $Ba_3EuRu_2O_9$ were characterised by low energy Raman scattering and their phonon spectra were measured for the first time. For $Ba_3CeRu_2O_9$, the number of observed modes and their polarisation dependence is in agreement with the claimed $P6_3/mmc$ space group. For $Ba_3EuRu_2O_9$, only one type of phonons was observable, and the scattering intensities were significantly weaker, indicating a lower sample quality.

High energy Raman spectra of $Ba_3EuRu_2O_9$ show a multitude of peaks in the energy range between 100 and 600 meV that can be associated with crystal field transitions. They lie mostly with the energy range for spin-conserving excitations predicted by calculations and RIXS measurements, but due to lack of computational results, an exact comparison is not possible. However, the Raman measurement constitute a significant improvement towards the resolution of individual excitations. The highest energy group of Raman peaks does not seem to correspond to any feature that were previously measured. The high number of peaks in combination with the results of a polarisation dependent measurement suggest that intra-cluster hopping is a strongly contributing interaction in the system.

For $Ba_3CeRu_2O_9$, a slightly lower number of crystal field peaks can be recognised. The detection of an isolated peak at 281 meV may suggests at least a local presence of Ce^{3+} ions and accordingly a mixed d^4 / d^5 valence for ruthenium. This could be caused by local oxygen deficiency in the material. Comparison to a plot of simulated energy states for a four-hole dimer shows good agreement between calculated energy states and Raman peaks. This suggests that the set of parameters used for this is accurate. As expected, neither $Ba_3EuRu_2O_9$ nor $Ba_3CeRu_2O_9$ show a temperature dependence in their spectra.

6.6 Potential future research topics in high energy Raman spectroscopy

The successful construction and functionality of the new high energy Raman setup demonstrated in this chapter now opens a wide field of potential research topics that could make good use of it. If the required additional equipment can be obtained, the accessible energy range could potentially even be extended up to $\approx$ 1.6 eV through the use of shorter-wavelength lasers.

Of course, the most obvious path would be to extend the research on cluster-Mott systems with quasi-molecular orbitals. Besides the two dimer materials presented in this thesis, it would be interesting to get comparative Raman spectra of the purely Mott insulating Ba_2CeIrO_6, and the trimer compound $Ba_3CeRu_3O_{12}$.

The comparatively high resolution of this setup can be utilised to resolve energy splittings of excitations such as crystal field transitions or spin-orbit excitons that have been suggested, but not successfully resolved by other experimental techniques like RIXS, e.g. the sidebands of the 600 meV spin-orbit exciton in Ba_2PrIrO_6.

In systems that are proposed to host Kitaev spin-liquids, one of the decisive questions is often how well they realise the effective $j_{eff} = \frac{1}{2}$ moments. Their existence relies on spin-orbit coupling splitting the t_{2g} orbitals in transition metals. If such a state indeed exists, there should be excitations from the ground state to the $J_{eff} = \frac{3}{2}$ and the $J_{eff} = \frac{5}{2}$ state. Typical values for the spin-orbit coupling constant in Kitaev candidate systems are between 160 meV for $RuCl_3$ [36] and 700 meV for Na_2IrO_3 [37]. In materials where the $j_{eff} = \frac{1}{2}$ character is not clearly established, like $BaCo_2(PO_4)_2$ [38] and $BaCo_2(AsO_4)_2$ [39, 40], high energy Raman spectroscopy should be able to provide further insight.

Detection of crystal field transitions by Raman spectroscopy could also be a good way to directly visualise Jahn-Teller effects [41], particularly when they are involved in a phase transition. One of the conclusions of the Raman measurements on K_2ReCl_6 presented in chapter 5 was that the octahedral tilting prevents the appearance of Jahn-Teller distortions in the material. However, the tilting angles are predicted to significantly reduce when potassium is replaced by larger ions, like rubidium or caesium [42]. Accordingly, in Rb_2ReCl_6 and Cs_2ReCl_6, a splitting could potentially be observed for the electronic transitions to the ${}^2E_g(\Gamma_8)$ and ${}^2T_{2g}(\Gamma_8)$ states around 9000 cm^{-1} [43].

Contributions

Samples for this study were grown by Henrik Schilling and Petra Becker (Universität zu Köln, Institut für Geologie und Mineralogie). Construction of the Raman setup, sample characterisation, Raman measurements and analysis were done by me. The RIXS data shown was measured by Lara Pätzold, Enrico Bergamasco and Markus Grüninger at DESY in Hamburg, Germany. The calculation of energy states for $Ba_3CeRu_2O_9$ was done by Lara Pätzold.

The chapter was written by me and represents my understanding of the topic.

Bibliography

[1] J. Hubbard, *Electron correlations in narrow energy bands*, Proc. R. Soc. A **276**, 237 (1963)

[2] M.C. Gutzwiller, *Effect of Correlation on the Ferromagnetism of Transition Metals*, Phys. Rev. Lett. **10**, 159 (1963)

[3] J. Kanamori, *Electron Correlation and Ferromagnetism of Transition Metals*, Prog. Theor. Phys. **30**, 275 (1963)

[4] A. Revelli, M. Moretti Sala, G. Monaco, P. Becker, L. Bohatý, M. Herrmanns, T.C. Koethe, T. Fröhlich, P. Warzanowski, T. Lorenz, S.V. Streltsov, P.H.M. van Loosdrecht, D.I. Khomskii, J. van den Brink, and M. Grüninger, *Resonant inelastic x-ray incarnation of Young's double-slit experiment*, Sci. Adv. **5**:eaav4020 (2019)

[5] A. Revelli, M. Moretti Sala, G. Monaco, M. Magnaterra, J. Attig, L. Peterlini, T. Dey, A. Tsirlin, P. Gegenwart, T. Fröhlich, M. Braden, C. Grams, J. Hemberger, P. Becker, P.H.M. van Loosdrecht, D.I. Khomskii, J. van den Brink, M. Herrmanns, and M. Grüninger, *Quasimolecular electronic structure of the spin-liquid candidate $Ba_3InIr_2O_9$*, Phys. Rev. B **106**, 155108 (2022)

[6] M. Magnaterra, M. Moretti Sala, G. Monaco, P. Becker, M. Herrmanns, P. Warzanowski, T. Lorenz, D.I. Khomskii, P.H.M. van Loosdrecht, J. van den Brink, and M. Grüninger, *RIXS interferometry and the role of disorder in the quantum magnet $Ba_3Ti_{3-x}Ir_xO_9$*, Phys. Rev. Research **5**, 013167 (2023)

[7] M. Magnaterra, A. Sandberg, H. Schilling, P. Warzanowski, L. Pätzold, E. Bergamasco, Ch.J. Sahle, B. Detlefs, K. Ruotsalainen, M. Moretti Sala, G. Monaco, P. Becker, Q. Faure, G.S. Thakur, M. Songvilay, C. Felser, P.H.M. van Loosdrecht, J. van den Brink, M. Herrmanns, and M. Grüninger, *Quasimolecular electronic structure of the trimer iridate $Ba_4InIr_3O_{12}$*, Phys. Rev. B **111**, 085122 (2025)

[8] M. Magnaterra, J. Attig, L. Peterlini, M. Herrmanns, M.H. Upton, J. Kim, L. Prodan, V. Tsurkan, I. Kézsmárki, P.H.M. van Loosdrecht, and M. Grüninger, *Quasimolecular J_{tet} = 3/2 Moments in the Cluster Mott Insulator $GaTa_4Se_8$*, Phys. Rev. Lett. **133**, 046501 (2024)

[9] J.W. Bennett, B.G. Hudson, I.K. Metz, D. Liang, S. Spurgeon, Q. Cui, and S.E. Mason, *A systematic determination of hubbard U using the GBRV ultrasoft pseudopotential set*, Comput. Mater. Sci. **170**, 109137 (2019)

[10] F.A. Cotton, *Metal Atom Clusters in Oxide Systems*, Inorg. Chem. **3**, 1217 (1964)

[11] H. Lee, M.Y. Jeong, J.-H. Sim, H. Yoon, S. Ryee, and M.J. Han, *Charge density functional plus U calculation of lacunar spinel GaM_4Se_8 (M = Nb, Mo, Ta, and W)*, EPL **125**, 47005 (2019)

[12] Y. Doi, M. Wakeshima, Y. Hinatsu, A. Tobo, K. Ohoyama, and Y. Yamaguchi, *Crystal structures and magnetic properties of the 6H-perovskites $Ba_3LnRu_2O_9$ (Ln = Ce, Pr and Tb)*, J. Mater. Chem. **11**, 3135 (2001)

[13] Y. Doi, K. Matsuhira, and Y. Hinatsu, *Crystal structures and Magnetic Properties of 6H-Perovskites $Ba_3MRu_2O_9$ (M = Y, In, La, Sm, Eu, and Lu)*, J. Solid State Chem. **165**, 317 (2002)

[14] Q. Chen, S. Fan, K.M. Taddei, M.B. Stone, A.I. Kolesnikov, J. Cheng, J.L. Musfeldt, H. Zhou, and A.A. Aczel, *Large Positive Zero-Field Splitting in the Cluster Magnet $Ba_3CeRu_2O_9$*, J. Am. Chem. Soc. **141**, 9928 (2019)

[15] J.W. Arblaster, *Crystallographic Properties of Ruthenium*, Platin. Met. Rev. **57**, 127 (2013)

[16] E. Kroumova, M.I. Aroyo, J.M. Perez-Mato, A. Kirov, C. Capillas, S. Ivantchev, and H. Wondratschek, *Bilbao Crystallographic Server: Useful Databases and Tools for Phase-Transition Studies*, Phase Transitions **76**, 155 (2003)

[17] H. Rho, S.L. Cooper, S. Nakatsuji, H. Fukazawa, and Y. Maeno, *Lattice dynamics and the electron-phonon interaction in* Ca_2RuO_4, Phys. Rev. B **71**, 245121 (2005)

[18] H. Rho, S.L. Cooper, S. Nakatsuji, H. Fukazawa, and Y. Maeno, *Raman scattering studies of* $Ca_{2-x}RuO_4$, Physica B **359-361**, 1270 (2005)

[19] S.-M. Souliou, J. Chaloupka, G. Khaliullin, G. Ryu, A. Jain, B.J. Kim, M. Le Tacon, and B. Keimer, *Raman Scattering from Higgs Mode Oscillations in the Two-Dimensional Antiferromagnet* Ca_2RuO_4, Phys. Rev. Lett. **119**, 067201 (2017)

[20] J.H. Jung, *Raman scattering and optical absorption studies of an orbital ordered* Ca_2RuO_4, Solid State Commun. **133**, 103 (2005)

[21] R. German, *Raman Spectroscopy on Selected Cooperative Systems*, PhD Thesis, Universität zu Köln (2022)

[22] A. Glamazda, P. Lemmens, S.-H. Do, and K.-Y. Choi, *Comparative Raman study of* $Ba_3MSb_2O_9$, Low Temp. Phys. **43**, 543 (2017)

[23] J. Quilty, H.J. Trodahl, and A. Edgar, *Raman Spectroscopy of* $BaRuO_3$, Solid State Commun. **86**, 369 (1993)

[24] S. Cotton, *Lanthanide and Actinide Chemistry*, John Wiley & Sons Ltd., Chichester, 2006

[25] D.D. Koelling, A.M. Boring, and J.H. Wood, *The electronic structure of* CeO_2 *and* PrO_2, Solid State Commun. **47**, 227 (1983)

[26] M.W. Shafer, *Preparation and Crystal Chemistry of Divalent Europium Compounds*, J. Appl. Phys. **36**, 1145 (1965)

[27] F. Gel'mukhanov and Hans Ågren, *Resonant inelastic x-ray scattering with symmetry-selective excitation*, Phys. Rev. A **49**, 4378 (1994)

[28] A. Revelli, C.C. Loo, D. Kiese, P. Becker, T. Fröhlich, T. Lorenz, M. Moretti Sala, G. Monaco, F.L. Buessen, J. Attig, M. Herrmanns, S.V. Streltsov, D.I. Khomskii, J. van den Brink, M. Braden, P.H.M. van Loosdrecht, S. Trebst, A. Paramekanti, and M. Grüninger, *Spin-orbit entangled $j=\frac{1}{2}$ moments in Ba_2CeIrO_6: A frustrated fcc quantum magnet*, Phys. Rev. B **100**, 085139 (2019)

[29] L. Pätzold, A. Sandberg, E. Bergamasco, M. Magnaterra, H. Schilling, P. Becker, M. Herrmanns, P.H.M. van Loosdrecht, and M. Grüninger, unpublished (2025)

[30] E. Saitoh, S. Okamoto, K.T. Takahashi, K. Tobe, K. Yamamoto, T. Kimura, S. Ishihara, S. Maekawa, and Y. Tokura, *Observation of orbital waves as elementary excitations in a solid*, Nature **410**, 180 (2001)

[31] P. Packiyaraj and P. Thangadurai, *Structural and photoluminescence studies of Eu^{3+} doped cubic Y_2O_3 nanophosphors*, J. Lumin. **145**, 997 (2014)

[32] C.M. Dodson and R. Zia, *Magnetic dipole and electric quadrupole transitions in the trivalent lanthanide series: Calculated emission rates and oscillator strengths*, Phys. Rev. B **86**, 125102 (2012)

[33] S. Afrin and P. Bollini, *On the Utility of Ce^{3+} Spin-Orbit Transitions in the Interpretation of Rate Data in Ceria Catalysis: Theory, Validation, and Application*, J. Phys. Chem. C **127**, 234 (2023)

[34] P. Serna-Gallén, H. Beltrán-Mir and E. Cordoncillo, *Practical guidance for easily interpreting the emission and physiochemical parameters of Eu^{3+} in solid-state hosts*, Ceram. Int. **49**, 41078 (2023)

[35] X. Zhang, L. Zhou, Q. Pang, J. Shi, and M. Gong, *Tunable Luminescence and* $Ce^{3+} \rightarrow Tb^{3+} \rightarrow Eu^{3+}$ *Energy Transfer of Broadband-Excited and Narrow Line Red Emitting* $Y_2SiO_5 : Ce^{3+}, Tb^{3+}, Eu^{3+}$ *Phosphor*, J. Phys. Chem. C **118**, 7591 (2014)

[36] P. Warzanowski, N. Borgwardt, K. Hopfer, J. Attig, T.C. Koethe, P. Becker, V. Tsurkan, A. Loidl, M. Herrmanns, P.H.M. van Loosdrecht, and M. Grüninger, *Multiple spin-orbit excitons and the electronic structure of* α-$RuCl_3$, Phys. Rev. Research **2**, 042007(R) (2020)

[37] K. Foyevtsova, H.O. Jeschke, I.I. Mazin, D.I. Khomskii, and R. Valentí, *Ab initio analysis of the tight-binding parameters and magnetic interactions In* Na_2IrO_3, Phys. Rev. B **88**, 035107 (2013)

[38] S. Das, S. Voleti, T. Saha-Dasgupta, and A. Paramekanti, *XY magnetism, Kitaev exchange, and long-range frustration in the* $J_{eff} = \frac{1}{2}$ *honeycomb cobaltates*, Phys. Rev. B **104**, 134425 (2021)

[39] R. Zhong, T. Gao, N.P. Ong, and R.J. Cava, *Weak-field induced nonmagnetic state in a Co-based honeycomb*, Sci. Adv. **6**:eaay6953 (2020)

[40] P.K. Mukharjee, B. Shen, S. Erdmann, A. Jesche, J. Kaiser, P.R. Baral, O. Zaharko, P. Gegenwart, and A.A. Tsirlin, *Intermediate field-induced phase of the honeycomb magnet* $BaCo_2(AsO_4)_2$, Phys. Rev. B **110**, L140407 (2024)

[41] S.V. Streltsov and D.I. Khomskii, *Jahn-Teller Effect and Spin-Orbit Coupling: Friends or Foes?*, Phys. Rev. X **10**, 031043 (2020)

[42] H.D. Grundy, I.D. Brown, *A Refinement of the Crystal Structures of* K_2ReCl_6, K_2ReBr_6 *and* K_2PtBr_6, Can. J. Chem. **48**, 1151 (1970)

[43] P.B. Dorain and R.G. Wheeler, *Optical Spectrum of* Re^{4+} *in Single Crystals of* K_2PtCl_6 *and* Cs_2ZrCl_6 *at 4.2°K*, J. Chem. Phys. **45**, 1172 (1966)

6.7 Appendix / Supplemental Information

Multi-peak fit of high energy $Ba_3EuRu_2O_9$ Raman spectrum

The easiest way to determine the minimum amount of excitations that are present in the high energy Raman spectrum of $Ba_3EuRu_2O_9$ is attempting to fit the spectrum with the lowest number of peaks possible. This fit, together with the measured data, is shown in fig. 6.10. It turns out that the spectrum can be desribed sufficiently well with ten Gaussian peaks at energies 181, 216, 236, 300, 313, 318, 413, 430, 533 and 557 meV.

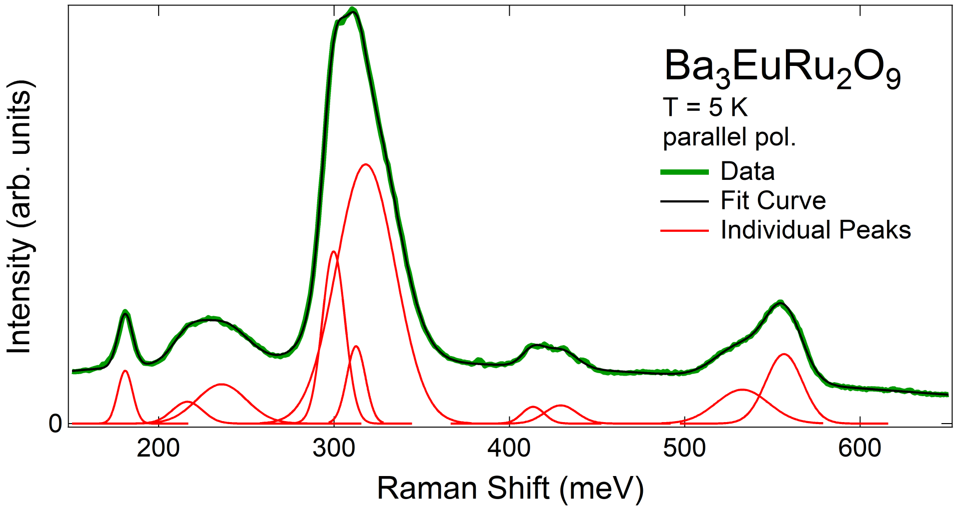

Figure 6.10: Multi-Peak fit of the $Ba_3EuRu_2O_9$ large-shift Raman spectrum at T = 5 K in parallel polarisation.

Comparison between RIXS and Raman spectra of BERO

Fig. 6.11 shows a comparison of the low temperature Raman spectrum of $Ba_3EuRu_2O_9$ (red line) with RIXS spectra taken at different points in reciprocal space (blue lines). Similar to $Ba_3CeRu_2O_9$, the RIXS spectra show three groups of excitations in different energy regions (0 – 0.55 eV, 0.55 – 1.1 eV and 1.1 – 1.7 eV), but the energy scale is slightly different. The peak in the Raman spectrum around 280 meV coincides well with the RIXS intensity maximum. Similar to $Ba_3CeRu_2O_9$, the highest energy Raman excitations lie in the region where the RIXS intensity is minimised. The group of excitations above 550 meV can be interpreted as spin-flip excitations and are not expected to be Raman active.

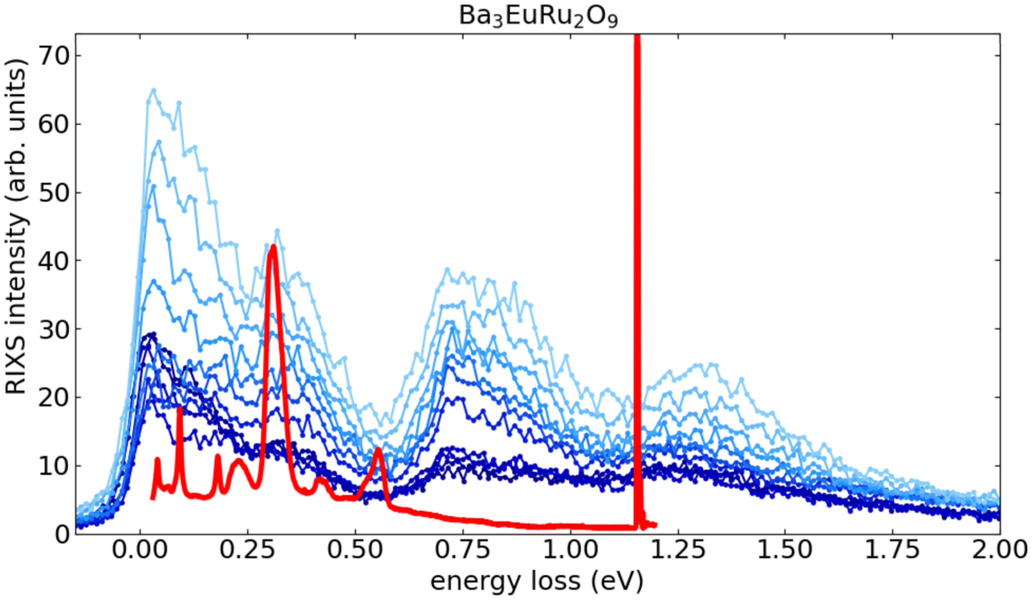

Figure 6.11: RIXS spectra of $Ba_3EuRu_2O_9$ measured at different points in reciprocal space at T = 5 K (blue lines). The red line an extended version of the parallel polarisation Raman spectrum at T = 5 K that was shown in fig. 6.5.

Polarisation dependence of $Ba_3CeRu_2O_9$ high energy spectra

Fig. 6.12 shows the high energy Raman spectra of $Ba_3CeRu_2O_9$ and silicon in parallel and crossed polarisation geometry. The measurement artefacts from the spectrometer don't show significant polarisation dependence and are present in all four spectra, although they are difficult to recognise in the cross polarised silicon spectrum due to generally reduced scattering intensity. The crystal field excitations of $Ba_3CeRu_2O_9$ below 500 meV are significantly weakened in crossed polarisation, and the scattering background is also weaker by a factor of ≈ 1.6, which is consistent with the relative transmission intensities of the beam splitter for horizontally and vertically polarised light.

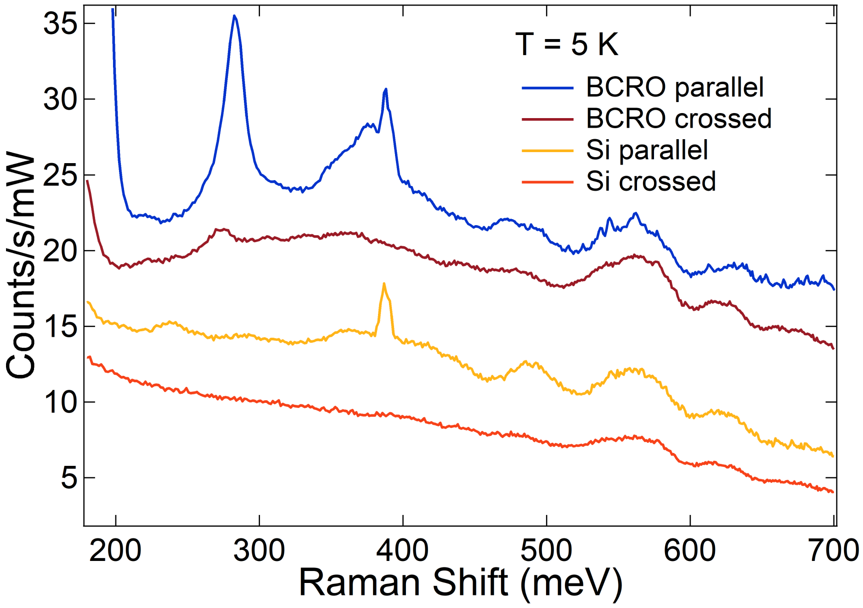

Figure 6.12: Raman spectra of $Ba_3CeRu_2O_9$ and Si at T = 5 K in parallel and crossed polarisation.

Comparison of the Raman spectrum of $Ba_3EuRu_2O_9$ with calculated f-f transition energies for the Eu^{3+} ion

Fig. 6.13 shows the Raman spectra of $Ba_3EuRu_2O_9$ at low temperature in parallel and crossed polarisation (top), and a calculated line spectrum of electronic f-level transitions for the Eu^{3+} ion. The only energy region with at least tentative agreement between the spectral peaks and the calculated lines is that between ≈ 1800 – 2100 meV ($^7F_0 \rightarrow {}^7F_3$ transitions).

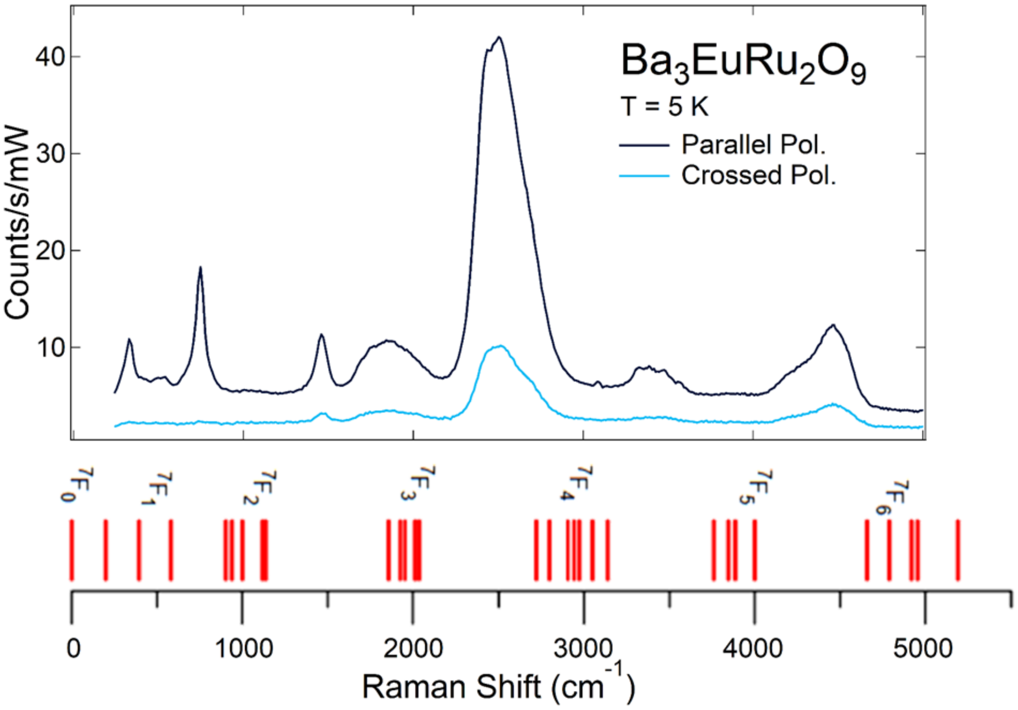

Figure 6.13: Comparison of the $Ba_3EuRu_2O_9$ large-shift Raman spectrum at T = 5 K with calculated transition spectrum for Eu^{3+}. Lower part of the figure adapted from [C. Cascales, J. Fernández, and R. Balda, Opt. Express 13, 2141 (2005)]

CHAPTER 7

Summary

This thesis aims to demonstrate different application possibilities for Raman spectroscopy in solid state physics and develop and showcase some rarely used extensions of the method.

Measurements on **Ni_3TeO_6** show that the scattering intensity of some phonons is different for left- and right circularly polarised light. This is quantified by calculating the Raman optical activity (ROA), which for most phonons yields values between 0.01 and 0.2. These values are giant compared to commonly reported values of 10^{-3} - 10^{-4} for chiral molecules. More generally, these results are among the very few cases where the method was successfully applied to crystals. A comparison with calculated ROA spectra shows good agreement in general, but deviations in some aspects, e.g. the exact energies and the sign of ROA. Calculations show that the strong chiral scattering contributions in this material originates from dynamic modification of the Berry curvature of the electronic band structure through phonon excitation. The phonon band structure and the associated phonon chiralities show that chiral phonons exist in this material, but their existence is not intrinsically connected to ROA. This study should thus establish ROA as a viable spectroscopic method for chiral solids, and Ni_3TeO_6 as one of the most promising chiral materials.

In K_2ReCl_6, polarisation selective Raman spectroscopy is performed in the temperature range between 5 K and room temperature. Besides showing the effect of the crystallographic phase transitions on the Raman active phonons, results also establish that the global cubic $Fm\bar{3}m$ symmetry is locally broken by disordered tilting of the $ReCl_6$ octahedra. Although differentiation between static and dynamic tilting is not possible, a dynamic process is deemed more likely. Contrary to expectations, there was no detectable Jahn-Teller distortion of the ReO_6 octahedra.

High energy Raman spectroscopy on Ruthenium dimer systems is successfully demonstrated, following construction of a new Raman setup. In $Ba_3EuRu_2O_9$ and $Ba_3CeRu_2O_9$, a number of crystal field excitations are observed in the energy range between 100 and 600 meV. The competition between crystal fields, spin-orbit coupling and intra-cluster hopping leads to a large number of states that can be scattered from, which impedes exact identification of the observed peaks. Nevertheless, comparison with a calculated energy level diagram shows some agreement for $Ba_3CeRu_2O_9$. Polarisation dependent measurements suggest that neither trigonal crystal field nor spin-orbit coupling are dominating, and that intra-cluster hopping plays a large role. The results show the advantages of the superior energy resolution of Raman spectroscopy, even in the energy regime up to 1 eV. To reduce the spectral artefacts, better filtering of the incident light is required. For the scattered light, the dielectric notch filters show used so far show a huge drop in transmission for higher wavelengths. This makes a measurement of excitations above 1 eV very difficult. Installation of holographic notch filters could make the setup much more effective for this energy range. Additionally, the significant difference in transmission of horizontally and vertically polarised light through the beam splitter causes a huge corresponding intensity difference in the measured spectra for different analysed polarisations. This could be prevented by using a polarisation independent beam splitter, or by circularly polarising the light before transmission. Finally, the spectral coverage could be significantly enhanced by using an incident laser with lower wavelength, e.g. 405 nm. Since the measurable energy range is mainly limited by the cut-off in detection efficiency of the CCD camera around 1000 nm (cf. chapter 3.3), this would increase the spectral coverage from $\approx$ 470 nm to $\approx$ 600 nm.

List of Publications

- **P. Stein**, T.C. Koethe, L. Bohatý, P. Becker, M. Grüninger, and P.H.M. van Loosdrecht, *Local Symmetry Breaking and Low Energy Continuum in* K_2ReCl_6, Phys. Rev. B **107**, 214301 (2023)
- P. Warzanowski, M. Magnaterra, **P. Stein**, G. Schlicht, Q. Faure, Ch.J. Sahle, T. Lorenz, P. Becker, L. Bohatý, M. Moretti Sala, G. Monaco, P.H.M. van Loosdrecht, and M. Grüninger, *Electronic excitations in* $5d^4$ $J = 0$ Os^{4+} *halides studied by resonant inelastic x-ray scattering and optical spectroscopy*, Phys. Rev. B **108**, 125120 (2023)
- A. Sahasradbudhe, M.A. Prosnikov, T.C. Koethe, **P. Stein**, V. Tsurkan, A. Loidl, M. Grüninger, H. Hedayat, and P.H.M. van Loosdrecht, *Chiral excitations and the intermediate-field regime in the Kitaev magnet* α-$RuCl_3$, Phys. Rev. Research **6**, L022005 (2024)
- L. Rieland, J. Wagner, R. Bernhardt, T. Wang, O. Abdul-Aziz, **P. Stein**, E.A.A. Pogna, S. Dal Conte, G. Cerullo, H. Hedayat, and P.H.M. van Loosdrecht, *Ultrafast Optical Control of Exciton Diffusion in* WSe_2*/Graphene Heterostructures Revealed by Heterodyne Transient Grating Spectroscopy*, Nano Lett. **24**, 9824 (2024)
- C. Reinhoffer, I. Razdolski, C. Kadlec, **P. Stein**, F. Kadlec, S. Germanskiy, A. Stupakiewicz, P.H.M. van Loosdrecht, and E.A. Mashkovich, *Terahertz Excitation of Exchange Mode in a Cavity Formed by Crystal Interfaces*, Phys. Rev. B **111**, 184412 (2025)
- **P. Stein**, R. Kaushik, E.V. Komleva, T.C. Koethe, V. Tsurkan, I. Kezsmarki, S.V. Streltsov, S. Artyukhin, M. Grüninger, and P.H.M. van Loosdrecht, *Giant Raman Optical Activity in chiral and polar* Ni_3TeO_6, unpublished (2025)

Data Availability

The dataset for this thesis is publish with Zenodo and is available at

- Stein, P. (2026). Dataset for the thesis 'Raman Spectroscopic View on Quantum Materials: Local Symmetry Breaking in K2ReCl6; Raman Optical Activity in Ni3TeO6; and Electronic Excitations in Ruthenates' [Data set]. Zenodo. https://doi.org/10.5281/zenodo.18163702